Dissertation
submitted to the
Combined Faculties for the Natural Sciences and for Mathematics
of the Ruperto-Carola University of Heidelberg, Germany
for the degree of
Doctor of Natural Sciences

put forward by

Diplom-Physiker:	Robert Gerald Klein
Born in:	Berlin-Mitte, Germany

Oral examination: 13th of January, 2010

Swift Heavy Ion Irradiated Boron Nitride With and Without the Application of High Pressure

Referees: Prof. Dr. R. Neumann

Prof. Dr. R. Miletich-Pawliczek

für Christian

Zusammenfassung

In seiner kubischen Form ist Bornitrid (BN) nach Diamant das zweithärteste bekannte Material. Die Struktur des hexagonalen BNs ist der des Graphits sehr ähnlich. Doch im Gegensatz zu dessen Kohlenstoff-Allotropen muss BN künstlich erzeugt werden, da natürliche Vorkommen nicht existieren. Erste Hinweise auf die Erzeugung von Diamant in mit Schwerionen bestrahltem Graphit gaben Anlass zu Experimenten an hexagonalem (hBN), mit dem Ziel, kubisches BN zu erzeugen. Zusätzlich angewandter Druck sollte diesen Prozess katalytisch begünstigen. Jedoch konnte eine solche Umwandlung nicht nachgewiesen werden. Dennoch verursacht die von Schwerionen an das Kristallgitter abgegebene Energie sichtbare Änderungen, wie eine stark orientierungsabhängige Verfärbung im hBN, die mit unterschiedlich ausgeprägten Gitterführungseffekten erklärt werden kann. Sowohl orientierungs- als auch druckabhängig entwickeln sich Intensitäten charakteristischer Ramanbanden mit zunehmender Fluenz. Des Weiteren konnte mittels Raman-Spektroskopie und Synchrotron-Röntgenbeugung *in situ* gezeigt werden, dass Ionenbeschuss den Phasenübergang von hBN zum wurtzitischen BN (wBN) in dem Sinne erleichtert, dass dieser im Gegensatz zu unbestrahltem hBN bei Druckerhöhung vollständiger abläuft.

Abstract

Cubic boron nitride (cBN) is the second hardest material after diamond. The hexagonal form (hBN) resembles graphite. However, due to speculations, derived from the generation of diamond in trajectories of energetic ions in graphite, irradiation experiments were initialized, aiming a hBN $\rightarrow$ cBN transition. Simultaneous pressurization were suggested to trigger such transitions. Nevertheless, this goal could not be reached, but several other, irradiation and pressure-induced effects have emerged. A strongly orientation dependent colourization is explained by ion channeling, which is believed to be also responsible for alterations in the Raman spectra of hBN crystals, irradiated under different orientations under simultaneous high pressure conditions. Furthermore, the pressure phase transition from hBN to wurtzitic BN is effected by ion irradiation, observed *in-situ* by XRD as well as Raman spectroscopy.

Acknowledgement

First of all, I would like to express my sincere thank to my supervisor and first referee Prof. R. Neumann, who gave me the opportunity to realise this thesis in his working group. He also enabled me to attend conferences and workshops, where I could always gain and exchange important experience.

Furthermore, I am indebted to Prof. R. Miletich-Pawliczek, who contributed valuable assistance throughout the time of research. His point of view of the results and experiments, as well as the realization of the measurements at the ESRF in Grenoble were of great value.

Prof. Takashi Taniguchi, who generously fabricated and accorded me the BN single crystals, was also a priceless benefit, and the AIRAPT conference he has organized, however, was a great experience.

Moreover, I appreciate the proper expertise of the high-pressure group within the Bayerisches Geoinstitut Bayreuth, especially the assistance of Dr. L. Dubrovinsky, who taught me the art of reaching highest pressures.

Dr. C. Trautmann gave me the thankworthy opportunity to a stay at the Australian National University and initialized first SAXS-beamtimes at the Australian Synchrotron, which was not only an unvorgettable experience, but also the promising start of a fruitful cooperation with Dr. P. Kluth, the SAXS expert, who kindly tested our BN single crytals for track formation.

Nevertheless, this work could have never been finished without the support, assistance and encouragement of all the members of the GSI Materials Research

Department. Therefore, I would like to thank espacially:

Ms. Dipl.-Phys. B. Schuster for the XRD measurement series at the APS synchrotron, and for all her helpful advices.

Dr. K.-O. Voss for the assembling of the numerous ionoluminescence devices, and his always patient assistance.

Mr. E. Schubert for his very active support.

Mr. Dipl.-Chem. T. Seidl for the ATR measurements.

Mr. Dipl.-Chem. M. Rauber and Dipl.-Phys. O. Picht for the SEM (EDX) introductions.

Dr. A. Sankarakumar for always having time and motivation for scientific chatting.

Dr. D. Severin for the realisation of the luminescence measurement at the novel M-branch irradiation site.

And all others, who contributed and offered support.

Many thanks be expressed also to the members of the Mineral Physics Group of the Heidelberg University as:

Mr. Dipl.-Min. C. Weikusat, who was always open for a helpful discussion, and a nightshift during beamtime. Thank you for the argon filling.

Ms. I. Glass for the XRD introduction and measurements.

Mr. Dipl.-Min. P. Schouwink for the support during ESRF beamtime.

Last but not least I would like to express sincere thanks to Ina Stützer, who always gave more than moral support, and to my friends and to my family.

All that was not possible without your always self-forgetting help, dear Christian, though it never returned worthily. Not even when you needed it most.

Contents

List of Figures vi
List of Tables vii

1 Introduction **1**

2 Theory **5**
2.1 Boron Nitride 5
2.1.1 Introduction 5
2.1.2 Cohesive properties 7
2.1.3 The hBN - wBN phase transition 13
2.1.4 The hBN - cBN phase transition 14
2.2 Stopping of Charged Particles in Matter 15
2.3 High Pressure 20
2.4 Raman Spectroscopy 22
2.4.1 The polarizability tensor 24
2.4.2 Lattice modes in single crystals 27
2.5 X-ray Diffraction 30
2.5.1 Analysing methods 30
2.5.2 The phase problem 31

3 Experimental **35**
3.1 Specimen Fabrication 35
3.1.1 Single crystals 35
3.1.2 Powder samples 36
3.2 Generation of High Pressure 36
3.3 Swift Heavy Ion Irradiation 41
3.3.1 Unilac 41
3.3.2 SIS18 41

3.4 Examination Methods 42
3.4.1 Raman spectroscopy 42
3.4.2 X-ray diffractometry 44

4 Results **47**
4.1 Structural Changes under Ambient Pressure Conditions 47
4.2 hBN Single Crystals Irradiated Under Different Pressures and Orientations 50
4.3 Pressurization of BN, Irradiated Under Ambient Conditions . . . 59
4.3.1 Cubic BN 59
4.3.2 Hexagonal BN 59

5 Discussion **69**
5.1 Radiation Stability examined by XRD 70
5.2 Ion-induced Colour Change 73
5.3 Irradiations under Different Pressures and Orientations 75
5.4 The hBN → wBN Phase Transformation 76
5.4.1 X-ray diffraction 79
5.4.2 Raman spectroscopy 80
5.5 Nature of the Defects 83

6 Outlook **85**

List of Figures

2.1 Boron nitride structures 10
2.2 Boron nitride phase diagram 13
2.3 Energy per unit cell for different BN phases 14
2.4 Energy loss behaviour 18
2.5 S_{total} as a function of density and Z_1 21
2.6 Energetic behaviour at pressure 22
2.7 The stress tensor 22
2.8 Rayleigh and Raman scattering principle 25
2.9 Character of Raman and infrared active vibrations 26
2.10 Vibrational modes in BN 29
2.11 Bragg's law 32
2.12 Laue and Debye-Scherrer methods 32

3.1 SEM micrographs of BN powder samples 37
3.2 Boron nitride structures 38
3.3 Diamond Anvil Cells 39
3.4 Unilac and X0 42
3.5 SIS and cave A 43
3.6 Inside cave A and Paris Edinburgh press 44
3.7 Raman bands in cBN and hBN 45
3.8 ESRF beamlines 46

4.1 Raman spectra of hBN and cBN (diff. ϕ; P = 1 bar) 48
4.2 XRD on irradiated hBN powder at 1 bar 49
4.3 XRD on irradiated cBN powder at 1 bar 50
4.4 XRD on irradiated wBN powder at 1 bar 51
4.5 Orientation dependent irradiation of hBN single crystals at 1 bar 52

4.6 Fluence series on orientation dependent irradiated hBN 53
4.7 hBN Raman intensity$_{max}$/background development after irradiation 53
4.8 Irradiated cBN single crystal 54
4.9 Raman spectra of pristine and irradiated cBN single crystals . . . 54
4.10 Two hBN crystals with different orientations in a gasket bore . . 55
4.11 E_{2g} Raman band of hBN at diff. P and ϕ ($\parallel a$) 56
4.12 E_{2g} Raman band of hBN at diff. P and ϕ ($\perp a$) 57
4.13 Raman band maximum / Raman background 58
4.14 Raman spectra of three cBN single crystals at different pressures 60
4.15 TO and LO Raman bands of cBN as a function of pressure . . . 61
4.16 Four hBN single crystals, irr. with diff. ϕ within a DAC 63
4.17 Disappearing E_{2g} Raman band in hBN 64
4.18 E_{2g} Raman band position for several irradiated hBN crystals as a function of pressure 65
4.19 Synchrotron X-ray diffractograms 66
4.20 hBN $\rightarrow$ wBN phase transition: norm. intensities for three diff. reflections 67

5.1 XRD on BN 70
5.2 Collapse line in hBN 72
5.3 Channeling in hBN 74
5.4 Raman background and E_{2g} intensity vs. ϕ for different pressures and orientations 77
5.5 Synchrotron XRD: proportions of the hBN and wBN phase . . . 78
5.6 Buckling in hBN-wBN phase transition 81
5.7 4 hBN crystals, diff. ϕ, norm. E_{2g} intensity vs. P 82
5.8 Inhomogeneous pressure application resulting in remaining hBN . 83
5.9 One- and three-boron centers in BN 84

6.1 First SAXS patterns of hBN 86

List of Tables

2.1 hBN stacking symmetries 9
2.2 BN lattice parameters 9
2.3 Properties of BN and C modification 11
2.4 Structural and cohesive properties of BN phases 12
2.5 Raman active modes for wBN 29

3.1 Density filters in the Raman spectrometer 45

4.1 Parameters of the orientation and pressure dependent hBN irradiation 55
4.2 Pressure dependent Raman band shift for cBN after irradiation . 62
4.3 Parameters of the hBN phase stability Raman experiment 62
4.4 Parameters of the samples for synchrotron XRD 65

1 Introduction

Investigation of materials, irradiated with relativistic heavy ions under high pressure conditions is a novel and promising field. Recently, it has been shown in several experiments that certain physical properties can alter in specific ways when a material is exposed simultaneously to both extreme conditions. E.g., the quenching of high-pressure phases in solids [66], which recover entirely after pressure release without ion bombardment. Furthermore, the temperature phase transition from monoclinic to tetragonal zirconia (ZrO_2), which has been triggered by sole exposure to high-energetic charged particles [6, 8, 9], occurs at fluences one order of magnitude lower when additionally pressurized [106]. Furthermore, the irradiation of zircon ($ZrSiO_4$) at 14 GPa with 2×10^9 uranium ions per cm^2 quenched its high-pressure polymorph reidite, which is not possible without heavy ion irradiation.

The initial idea of such experiments originated, however, from geosciences. More precisely, from geochronology where fission tracks in track forming minerals are used to estimate the age of the inclusion and hence the age of the surrounding rock. Since during the Earth's genesis isotopes of the most prevalent elements accumulated within the mantle of our planet [55], the track-causing fission process takes place in different possible depths and therefore at different pressures. Thus, it was under debate, if fission fragments behave in the same manner when the surrounding material is highly compressed. Due to its capability of delivering accelerated heavy ions, that bevave like fission fragments, energetic enough to interpenetrate the first gem of a diamond anvil cell, irradiation experiments were conducted at GSI, using the heavy ion synchrotron SIS18.

Due to the request for the beam exposure of larger sample chambers, a new class of pressure generating devices has been introduced to swift heavy ion

irradiation experiments. These so-called Paris Edinburgh presses are suited to contain specimens in the order of several mm^3 which, on the other hand turns out to be a drawback with respect to the anvil material. Since diamond of the necessary size is not available, new substances have to be established, suitable for extreme conditions as high pressure, high temperature as well as large doses of heavy ion irradiation. Cubic boron nitride is the second-hardest material after diamond, and therefore withstands very high pressures and shear forces. Furthermore, it is insoluble in iron, nickel, and related alloys at high temperatures, whereas diamond is soluble in these metals to create carbides. These properties in combination with a moderate price for the acquisition make cubic boron nitride the ideal anvil material for higher dimensioned pressure applications. Though it does not exist in nature, one has to produce it in a high temperature - high pressure procedure using multi anvil presses and catalysts. In 1957, Wentorf [135] succeeded with the first fabrication of cBN[1] and named his discovery "Borazon". A long and fruitful time of research began and brought forward the high-pressure community. In the near future, cBN may replace ruby as pressure calibrant since it possesses a higher temperature resistance and via Anti-Stokes scattering it is possible to establish a straightforward temperature probe for measurements within the pressure chamber. Unlike ruby, cBN delivers 'true' Raman bands instead of luminescence lines.

However, irradiation experiments on the hBN counterpart graphite by Wang et al. [133], that resulted in nano-diamond generation, encouraged us to repeat such investigations on pressurized hBN, in order to obtain cBN. Unfortunately, even with the application of additional pressure, which was suggested to lower the transformation threshold, this goal could not be reached so far. Nevertheless, the focus on the pressure phase transition hBN → wBN lead us to in-situ investigations using Raman spectroscopy on single crystals as well as synchrotron X-ray diffraction on powder samples. It could have been shown that irradiation with energetic Au^+ ions prior pressurization results in an entirely proceeded phase transition at a considerably lower pressure than for non-irradiated hBN samples, though the initial pressure for the transformation is not affected by heavy ion bombardment. An explanation is given by a lattice collapse and

[1] The first synthesis of hexagonal BN has been managed by Balmain in 1842 [4].

buckling of the hexagonal planes in hBN.

Furthermore, irradiation experiments utilising the non-isotropic character of the hBN lattice, revealed pressure dependences by means of luminescence background increase and decreasing Raman band intensities. It turned out, that hBN single crystals resist ion bombardment the better the higher the applied pressure, but only when irradiated along the direction of the crystallographic c-axis. Interestingly, hBN also changes its color from grayish-white into a deep red tone, when ions traverse the crystal parallel to c. The well known ion-channeling effect can therefore be used in order to explain such processes, originating from lattice defects, which can be F-centers.

Cubic BN possesses, up to fluences of $\approx 1.5 \times 10^{13}\ {}^{ions}/_{cm^2}$*, high irradiation hardness. Both hBN and cBN does not amorphize by ion bombardment on the above metioned fluences, proved via ex-situ Cu-*k_α *X-ray diffraction.*

The ion irradiation itself took place at the GSI's Unilac accelerator (X0) for those samples not being under pressure, and at the SIS (Cave A) for the samples exposed to high pressure.

2 Theory

2.1 Boron Nitride

2.1.1 Introduction

Boron nitride (BN) does not exist in nature and is therefore produced synthetically, which succeeded first Balmain in the year 1842 [4]. At first sight the position of boron (B) and nitrogen (N) in the periodic table of the elements is noticeable due to its vicinity to carbon, which is in terms of the atomic number the average of both B and N. Expectedly, BN emulates all carbon allotropes such as graphite and diamond. Even BN-nanotubes [18] as well as BN-fullerenes [37, 119] are known. In the following the hexagonal graphite-like BN is mentioned as hBN and the cubic BN counterpart of diamond as cBN. Furthermore, two different BN structures are well-known: The wurtzite type wBN and the rhombohedral phase rBN. The former is the high-pressure phase of hBN [15, 128], and cBN can be formed when rBN is exposed to high pressure. However, both wBN and rBN are metastable phases at ambient conditions, and the growth of single-crystalline bulk material is realisable only in hBN as well as cBN. Table 2.2 displays the lattice parameters of the most common BN phases.

Remarkably, it is a moot question whether hBN or cBN is the stable modification at standard conditions. Corrigan and Bundy [19] predicted hBN as the thermodynamically stable structure in analogy to the carbon phase diagram. In contrast, Solozhenko [113, 114] presented a phase diagram with cBN as the theromdynamically stable structure, while the equilibrium line between both phases intersects the temperature axis at 1600 K.

Regarding these differences, it seems inevitable to draw some conclusions from cohesive energy calculations (see Table 2.4). Equilibrium properties of a crystal

can be derived from thermodynamic potentials, e.g. the Helmholtz free energy $F(T,V) = F_0(V) + F_{vib}(T,V)$, where F_0 is the static lattice energy without vibrational contributions, F_{vib}.

The transition between both cubic and hexagonal phase of BN is always a phase transition of first order [126]. Therefore, the line between cBN and hBN in the p-T diagram indicates the equlibrium of the thermodynamic potentials of the coexisting phases, determined by the equilibrium condition

$$G_{\text{cubic}}\left(p,T\right) = G_{\text{hexagonal}}\left(p,T\right) \tag{2.1}$$

wheras $G\left(p,T\right)$ is the free enthalpy under given pressure and temperature conditions. G is the sum of the Helmholtz free energy and the product of pressure p and unit cell volume V.

$$G\left(p,T\right) = F_0 + F_{\text{vib}} + pV \tag{2.2}$$

The static part of the Helmholtz free energy $F_0\left(V\right)$ was calculated by Albe [1] and is plotted in Figure 2.3. In order to discuss the vibrational contributions of the zero point Helmholtz free energies, the empirical Debye-Grüneisen approximation was used [1].

$$F_{\text{vib}} = 2 \times 3Nk_BT \int 2\sinh\left(\frac{\hbar\omega}{2k_BT}\right) g\left(\omega\right) \mathrm{d}\omega \tag{2.3}$$

For cubic systems the phonon density of states $g\left(\omega\right)$ can be derived from the three-dimensional Debye model

$$g_D^{(3\text{D})} = \begin{cases} 3\,\frac{\omega^2}{\omega_D^3} & \omega \leqslant \omega_D \\ 0 & \omega > \omega_D \end{cases} \tag{2.4}$$

The cutoff frequency ω_D is linked to the Debye temperature Θ_D by

$$k_B\Theta_D = \hbar\omega_D \tag{2.5}$$

With the proposed cBN Debye temperature of 1700 K [36] we obtain a zero point vibrational energy

$$F_{\text{vib}} = 0.33\,{}^{\text{eV}}/_{\text{unitcell}} \tag{2.6}$$

For graphitelike structures as hBN a two-dimensional Debye-approximation is more suitable due to the weak interplanar binding. The phonon density of states is here

$$g_D^{(2\text{D})} = \begin{cases} 2\,\frac{\omega}{\omega_D^2} & \omega \leqslant \omega_D \\ 0 & \omega > \omega_D \end{cases} \tag{2.7}$$

The suggested Debye temperature for hBN of 1900 K [1] yields a zero point vibrational energy of

$$F_{\text{vib}} = 0.32\,{}^{\text{eV}}/_{\text{unitcell}} \tag{2.8}$$

Finally, free enthalpy calculations of Albe [1] deliver an equilibrium line which crosses the temperature axis at ca. 1450 K, indicating cBN as the stable form at standard conditions. This is in contrast to the calculations of Corrigan and Bundy [19], who pronounced hBN as the stable phase at room temperature and pressure.

2.1.2 Cohesive properties

Hexagonal hBN allocates carbon. It also consists of a layered planar comb-like structure (Figure 2.1), in which the B and N atoms are arranged alternately. However, in contrast to graphite, the hexagons in hBN are not staggered but lying right upon each other, that above and below of each N atom a B atom is placed (and vice versa). The physical properties of hBN and graphite are very similar (Table 2.3). Their densities are virtually identical and both exhibit a very high melting point which is beyond 3000 K. The hBN c axis length, which is determined by a mixture of ionic attraction between oppositely charged ions in adjacent planes, and weak van der Waals interaction such as in graphite, varies much more under hydrostatic pressure than the a-axis length, which is given by the extremely short and strong ionic-covalent sp^2 bondings. This is found both experimentally and theoretically [117]. Up to 12 GPa the relative

compression of the a axis is insignificant, while the c axis is compressed to about 85 %. This strong directional bonding between adjacent coplanar atoms shows charge localization closer to the N atom than the B atom, and depending on the radii assumed for these atoms, each B atom loses 1-2 electrons to its three neighbouring N atoms. Electrons in π orbitals are also localized closer to the N atoms than the B atoms [80]. Unlike graphite, hBN occurs due to its bi-atomic character in various stacking orders as specified in Table 2.1, whereas the energetically preferred way of stacking is not yet known nowadays [88]. The cohesive energy of the atoms within a hBN plane has been the subject of a variety of works and differs between 6.41 $^{\mathrm{eV}}/_{\mathrm{atom}}$ [1] and 1.794 $^{\mathrm{eV}}/_{\mathrm{atom}}$ [31]. However, the cohesive energy between the hBN layers is with 0.024 $^{\mathrm{eV}}/_{\mathrm{atom}}$, as expected, drastically lower and was calculated with the van der Waals density function (vdW-DF) [103].

Cubic The zinc blende modification of boron nitride, commonly referred to as cubic boron nitride (cBN), is the second-hardest known material after diamond. For this reason and due to other outstanding properties like chemical inertness, high-temperature stability, wide band gap and low dielectric constant, it has attracted a large interest in both fundamental as well as applied fields. Whether cBN is thermodynamically the most stable structure at 0 K among all BN phases is still up for debate. As in diamond the atoms in BN are connected via sp^3 bonds. But diamond forms a strong covalent bond through sharing of its electrons, whereas cBN appears to an appreciable extent on ionic interaction for its bonding energy.

Wurtzitic The lattice energy of the wurtzitic structure is slightly higher than for cBN [1] and is known as a metastable phase under ambient conditions. Experiments [115] and calculations [1] yield that the unit cell axes scale in the same fashion as those of cBN with increasing hydrostatic pressure. This is less surprising due to the sp^3-bonded structure of this modification. Although the wBN bonding is predominantly sp^3 in nature it differs from that of cBN [75]. The c-axis bond of wBN may possess more ionic characteristics than other bonds, whereas all bonds in cBN are identical.

Table 2.1: Symmetries of different hBN stackings [88]. E.g.: AA stacking is tantamount to indistinguishable layers, AB means every second layer is located in the same manner, and AJ stands for the tenth layer which lies exactly underneath the first one.

	Hermann-Mauguin		Schoenflies	
Stacking	Space group	Point group	Point symmetry	Point group
AA	$P\overline{6}m2$	$\overline{6}m2$	D_{3h}	X
AB	$P63/m2/m2/c$	$6/mmm$	D_{3d}	D_{6h}
AC	$P1$	1	C_{1h}	D_{2h}
AD	$P3m1$	$3m1$	C_{3v}	D_{3h}
AE	$P63/m2/m2/c$	$6/mmm$	D_{3d}	D_{6h}
AF	$P63/m2/m2/c$	$6/mmm$	D_{3d}	D_{6h}
AG	$P121/m1$	$2/m$	C_1	C_{2h}
AH	$C2/m2/c21/m$	Mmm	C_{1h}	C_{2v}
AI	$C2/m2/c21/m$	mmm	C_{1h}	D_{2h}
AJ	$P121/m1$	$2/m$	C_{2h}	D_{2h}

Rhombohedral Since rBN is akin to hBN, the cohesive energy of both structures are nearly the same. Calculations based on a density functional theory [1] revealed only a very small difference to hBN because of a higher bulk modulus for rBN in comparison to hBN.

Table 2.2: Lattice parameters for perfect crystalline samples of BN at 298 K [64].

phase	a ($\AA$)	c ($\AA$)
hBN	2.50428 (5)	6.6562 (10)
rBN	2.5042 (2)	9.99 (1)
cBN	3.6153 (1)	
wBN	2.5505 (3)	4.210 (1)

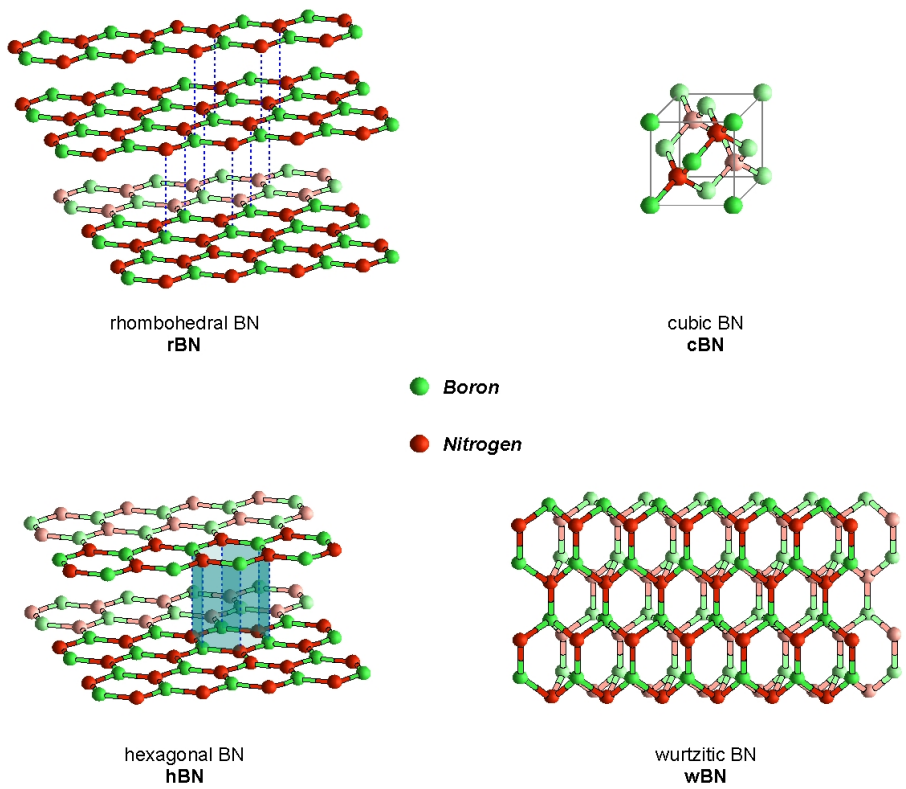

Figure 2.1: Structures of boron nitride. Both rhombohedral and hexagonal BN possess weak sp^2 bonds. Cubic as well as wurtzitic BN are bound via very strong sp^3 bonds.

Table 2.3: Some mechanical, electrical and thermodynamical properties of BN modifications in comparison with the common carbon phases. (aBN: amorphous BN) All data are measured at ambient conditions, or calculated for such conditions.

	aBN	hBN	wBN	rBN	cBN	graphite	diamond
density (g/cm^3)	2.28 [134]	2.1 [102]	3.39 [102]	2.28 [32]	3.45 [102]	2.1 [93]	3.52 [93]
Mohs hardness		1 - 2 [134]	10 [36]	n.a.	10 [36]	1 - 2 [93]	10 [93]
Knoop hardness (GPa)	10 [134]		34 [36]	n.a.	45 [36]		100 [93]
Thermal conductivity (W/cmK)	0.03 [41]	$\parallel$ 6 $\perp$ 0.3 [102]			7.4 [102]	$\parallel$ 2-20 $\perp$ 0.02-0.8 [93]	$\leq$ 12 [17]
Bandgap (eV)	5.05 [142]	5.2 [124]	5.0 [139]	n.a.	6.4 [29]	0	5.5 [93]
Refractive index	1.7 [41]	$\parallel$ 2.13 $\perp$ 1.65 [52]	2.05 [140]	n.a.	2.1 [36]	2.0 [93]	2.4 [93]
Static dielectric constant		$\parallel$ 5.09 $\perp$ 7.04 [33]	7.0 [3]		7.1 [36]	0	5.68 [11]
Magnetic susceptibility (μemu/g)		$\parallel$ -0.48 $\perp$ -17.3 [146]				$\parallel$ -(0.2-2.7) $\perp$ -(20-28) [42]	-1.6 [42]
Heat capacity ($J\ K^{-1}\ mol^{-1}$)		19.85 [32]	16.45 [32]	20.63 [32]	15.95 [32]	10.24 [96]	8.03 [96]

Table 2.4: Calculated structural and cohesive properties of several BN phases: Volume per atom V, lattice constant a, cohesive energy E_c (for hBN and rBN between the atoms within a layer), ratio of interlayer distance to lattice constant c/a, energy difference to the cohesive energy of cBN ΔE, bulk modulus B, and pressure derivative of the bulk modulus B'.

	Albe [1]	Furthmüller *et al.* [31]	Xu and Ching [139]	van Camp and van Doren [127]
cubic BN				
V (Å^3)	5.797	5.718	5.905	5.954
a (Å)	3.593	3.576	3.615	3.625
E_c (eV/atom)	-6.47	-8.152	-7.00	n.a.
B (GPa)	395	397	370	392
B'	3.65	3.59	3.8	3.31
ΔE (eV/atom)	0	0	0	0
wurtzitic BN				
V (Å^3)	5.813	5.731	5.845	6.73
a (Å)	2.532	2.521	2.536	2.6883
c/a	0.827	0.826	0.828	0.8
B (GPa)	394	401	390	107
B'	3.68	3.59	6.3	4.24
ΔE (eV/atom)	0.011	0.020	0.075	n.a.
hexagonal BN				
V (Å^3)	8.747	8.613	8.970	10.02
a (Å)	2.496	2.468	2.494	2.592
c/a	1.300	1.295	1.335	1.330
B (GPa)	30.1	26.1	335	77
B'	10.1	3.66	3.76	4.41
ΔE (eV/atom)	0.057	0.055	-0.35	
rhombohedral BN				
V (Å^3)	8.693	8.603	n.a.	n.a.
a (Å)	2.493	2.495	n.a.	n.a.
c/a	1.296	1.294	n.a.	n.a.
B (GPa)	32.3	26.2	n.a.	n.a.
B'	10.3	3.87	n.a.	n.a.
ΔE (eV/atom)	0.057	0.052	n.a.	n.a.

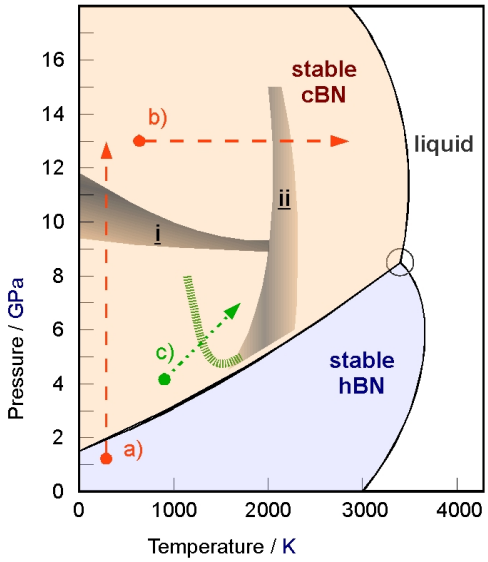

Figure 2.2: Boron nitride phase diagram according to Eremets [28]. Black solid lines mark the edges of both stable phases cBN and hBN. Furthermore, the metastable phase wBN can be produced using path **a)**. In order to obtain cBN an additional temperature increase is required **b)**. Here the blurry fields indicate the domains for phase transitions from hBN ⇒ wBN **i** as well as from wBN ⇒ cBN **ii** [19]. The green arrow **c)** is a possible cBN production path starting with rBN and crossing the necessary barrier (green dashed line) [125].

2.1.3 The hBN - wBN phase transition

As displayed in Figure 2.2, hBN undergoes a phase transition to the hexagonal close-packed polymorph wBN, starting at a pressure of ca. 9.5 GPa and room temperature. The wBN obtained in such a manner is quenchable after releasing the pressure, though only in powder samples. No single crystal bulk material of wBN has been produced until today. Within this work, the transformation hBN ⇒ wBN was the only phase change we have observed. In the literature, two possible mechanisms were proposed by which the hBN to wBN transformation could proceed: The chair deformation [54] that may only involve the direct bonding between the layers, and the boat deformation [94] that may require the relative rotation and displacement between the layers.

The chair deformation Near K-edge spectroscopy using inelastic X-ray scattering (IXS or X-ray Raman spectroscopy) provides information about the char-

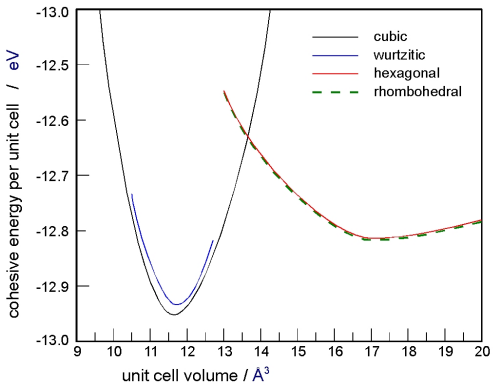

Figure 2.3: Cohesive energies of BN as a function of cell volume in the cubic, wurtzitic, hexagonal, and rhombohedral structure; calculated by Albe [1].

acteristics of the BN π and σ bonds, which has been investigated by Meng et al. [75]. It is described that the sole displacement of N atoms along the c direction will transform hBN into wBN. In hBN, B and N form strong covalent sp^2 bonding (σ state) within the plane; however, there is a weak interlayer p bonding (π state) with significant ionic characteristics. As the pressure increases, the van der Waals interaction between the layers becomes small compared to the dominant electrostatic repulsion. Wang et al. [130] managed to observe strong directional bonding between adjacent coplanar atoms in hBN resulting in charge accumulation closer to the N atoms, owing to the electron deficient nature of B atoms. With the displacement of N atoms along the transition path, each N atom gradually bonds to a B atom in the adjacent plane, and at the transition sp^2 hybridization in hBN evolves into sp^3 hybridization in wBN.

The boat deformation This mechanism involves lateral motion between the layers, that may be activated at high temperatures depending on the PT path and on the crystalline quality of the starting hBN phase [75].

2.1.4 The hBN - cBN phase transition

It is argued that during the synthesis of cBN by HTHP methods hBN first transforms by compression along the c-axis into wBN [67]. The subsequent wBN $\Rightarrow$ cBN transition occurs by a so-called dislocation mechanism [46, 50].

Under 7.7 GPa the formation of cBN starts at 1250 °C. Defects in the wBN lattice are accounted for the forming of nucleation centres. When pressure is sufficiently high, the wBN will convert into cBN around these nucleation centres by increasing the temperature. Thus, without using catalysts the transformation path from hBN to cBN must be directed over the generation of wBN.

2.2 Stopping of Charged Particles in Matter

Charged particles, when traversing matter, release their kinetic energy in a strong velocity-dependent manner (Figure 2.4 a). Two major decelerating processes are to be distinguished: The first process is called nuclear stopping, and occurs for ion velocities v sufficiently lower than the Bohr velocity v_0[1], which implies an energy transfer to recoiling nuclei. Or in other words - the incoming ion is slow enough to perceive the lattice atoms as neutral solid spheres. Since nuclear stopping affects only a very small part of the irradiated crystal and covers a comparatively diminutive range of ion energies, it is of minor importance in the situations considered in this thesis. A theoretical treatment of the nuclear stopping mechanism is given by Sigmund [109].

On the other hand, when $v \gg v_0$, the electronic stopping process becomes the dominating mechanism of energy exchange between the traversing ion and the target atoms. Commonly expressed, the projectile and the irradiated atom see each other more and more as an electromagnetic field between the positive-charged nucleus and the negative-charged electron cloud with increasing velocity, causing interpenetration followed by energy transfer to the electron shell. This process has been described by H. Bethe for non-relativistic projectiles in 1930 [10], and subsequently for relativistic particles (2.9) in 1932 (Sigmund 2004) [109].

[1] Bohr velocity v_0 is defined as the classical speed of the electron on the innermost shell of a hydrogen atom. $v_0 = 2.42 \times 10^8$ cm/sec.

$$-\frac{\mathrm{d}E}{\mathrm{d}x} = \frac{4\pi}{m_e c^2} \cdot \frac{nz^2}{\beta^2} \cdot \left(\frac{e^2}{4\pi\varepsilon_0}\right)^2 \cdot \left[\ln\left(\frac{2m_e c^2 \beta^2}{I \cdot (1-\beta^2)}\right) - \beta^2\right] \tag{2.9}$$

β	$= \frac{v}{c}$
v	particle velocity
E	particle energy
x	distance travelled by the particle
c	speed of light
z	particle charge
e	elementary charge (1.602×10^{-19} C)
m_e	rest mass of the electron (9.109×10^{-31} kg)
n	electron density of the target
I	mean excitation potential of the target

Here, the electron density of the material can be calculated by $n = \frac{N_A Z \rho}{A}$, where ϱ is the density of the material, Z the atomic number, and A the mass number of the target material, respectively. N_A is the Avogadro number. The mean excitation potential I describes the target material and was given by Bloch [12] in 1933 as $I = (10\,\mathrm{eV}) \cdot Z$. Hence, (2.9) is called the *Bethe-Bloch equation*. Nevertheless, due to the existence of more accurate tables of I as a function of Z [84], obtained by experimental and theoretical investigations, the use of such tables yields more reliable results. The mean excitation potential versus Z shows a more oscillating behaviour due to necessary corrections from (2.9). Detailed descriptions of these corrections are found elsewhere [109]. Since Bethe assumed that the projectile is a point charge without shell electrons, the real stopping power is somewhat reduced taking into account a decreased effective charge due to shielding shell electrons [109]. Furthermore, the Barkas-Andersen effect needs to be considered for energy loss calculations of heavy ions, which gives rise to a z^3 correlation in (2.9) instead of $\propto z^2$. For extreme relativistic velocities, the Fermi density effect has to be taken into account in the calculations, [51], which is no longer negligible beyond $10\,^{\mathrm{GeV}}/_{\mathrm{u}}$.

An important property of the energy loss function is its profoundly non-linear way to release the ion energy - as depicted in Figure 2.4 (a) and (b). Unlike

photons, which spend their energy in a negative exponential manner, ions reach their maximum of energy loss per unit length at a certain velocity within the crystal - if the initial velocity was high enough. Furthermore, the energy loss as a function of penetration depth depends on the density of the material as well as on the mass of the impinging ion. Both dependencies are displayed in Figure 2.5.

Energy transfer mechanisms In the electronic stopping regime, which is the dominating deceleration process in our experiments, the energy of the moving ion is transferred to the material. Two major mechanisms have been developed in order to describe the energy transfer from the moving ion to the lattice. Dessauer [22] proposed the fulminant heating of the material around the ion path, which was later called the *thermal spike* model [26, 132], at which the energy is being transmitted via electron-phonon coupling. The time scale of a thermal spike is very short since the energy is deposited by the heavy ion projectiles within 10^{-16} s, shared between the electrons within 10^{-15} s, and thermalization in the lattice occurs within 10^{-13} s [76]. The energy diffusion in the electronic and atomic subsystems at time t and at a distance r from the ion track assuming cylindrical geometry is described by two coupled differential equations,

$$C_e\left(T_e\right)\frac{\partial}{\partial t}T_e = \frac{1}{r}\frac{\partial}{\partial r}\left[rK_e\left(T_e\right)\frac{\partial}{\partial r}T_e\right] - g\cdot\left(T_e - T_l\right) + A\left(r,t\right) \quad (2.10)$$

$$C_l\left(T_l\right)\frac{\partial}{\partial t}T_l = \frac{1}{r}\frac{\partial}{\partial r}\left[rK_l\left(T_l\right)\frac{\partial}{\partial r}T_l\right] + g\cdot\left(T_e - T_l\right) \quad (2.11)$$

where $T_{e,l}$, $C_{e,l}$, and $K_{e,l}$ are the temperature, specific heat, and thermal conductivity for the electronic system and the lattice, respectively. The initial energy density $A\left(r,t\right)$ is taken from a spatial distribution function $F\left(r\right)$ [129]:

$$A\left(r,t\right) = b\cdot\left(\frac{\mathrm{d}E}{\mathrm{d}x}\right)_{\text{electr.}}\cdot\exp\left[-\left(t-t_0\right)^2/2t_0^2\right]\cdot F\left(r\right) \quad (2.12)$$

with $t_0 = 10^{-15}$ s as the time required for the electrons to reach thermal equilibrium. b is a normalization constant so that the total energy input is equal

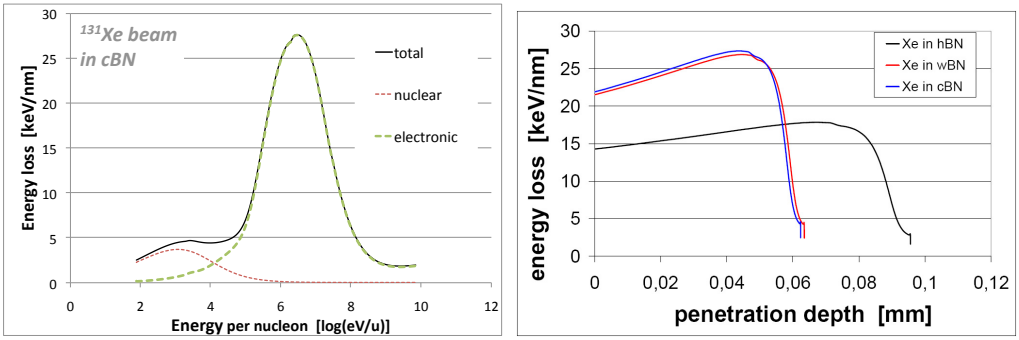

(a) Energy loss regimes of ^{131}Xe ions in cBN. $S_{\text{total}} = S_{\text{nuclear}} + S_{\text{electronic}}$

(b) Energy loss as a function of penetration depth in different BN modifications. $E_0 = 11.1$ MeV/u

Figure 2.4: Characteristics of the energy loss function in boron nitride.

to $(\mathrm{d}E/\mathrm{d}x)_{\text{electr.}}$. The electron-phonon coupling value g can be calculated using specific material parameters [132]:

$$g = \frac{\pi^4 \left(k_B z n_l v_s\right)^2}{18 K_e \left(T_e\right)} \tag{2.13}$$

where v_s is the sound velocity, n_l the atomic density and z the number of electrons participating in the thermal spike, which can be seen as $z = 1$ for most situations [14]. Due to a variety of experimental difficulties by means of temperature measurements in the wake of moving ions, numerical calculations are the method of choice. Dufour *et al.* [26] obtained temperatures in irradiated metals of up to 2,000 K for the lattice atoms and even up to 20,000 K for the electronic subsystem.

In contrast to the thermal spike model, which deals with temperature effects, another model has been developed in order to take into account the pressure effects, caused by a transversal shock wave, which is triggered by the traversing ion. Fleischer *et al.* introduced therefore the "Ion explosion spike mechanism" [30], which is nowadays known as the *Coulomb explosion* model. This is useful particularly with regard to the treatment of insulators since the inserted energy cannot be transferred via the electronic subsystem. The assumption is that the mutual repulsion of the positive (lattice) ions catapults them into the surrounding lattice. Hence, if the stress, induced by the electrostatic force of

the moving ion, is greater than the local bonding strength, the crystal matrix reacts by displacements of the constituents causing modified chemical bonds, melting, and vapourization, and may trigger phase transitions or latent track formation. When two ions in a material of dielectric constant ε and average atomic spacing a_0 have received an average ionization of z unit charges e, the force between them is $z^2e^3/\epsilon a_0^2$ or a local force per unit area (the electrostatic stress σ_e) of $z^2e^3/\epsilon a_0^4$. By noting that the theoretical mechanical tensile strength σ_m of material of Young's modulus E is approximately $\frac{1}{10}E$ [95], the electronic stress turns out to be larger than σ_m if $z^2e^2/\epsilon a_0^4 > \frac{1}{10}E$ or if

$$z^2 > R \equiv \frac{1}{10}\frac{\epsilon a_0^4}{e^2} \tag{2.14}$$

where R is defined as the stress ratio. Relation (2.14) thus indicates that tracks should be formed most easily in materials of low mechanical strength, low dielectric constant and close interatomic spacing.

Channeling The impact-parameter distribution between the ion projectile and the target atoms is orientation independent if the traversed specimen is homogeneous and isotropic. Unlike materials such as graphite or hBN, which are composed of highly non-isotropic distributed constituents. Here, the stopping process of the impinging ions is known to be significantly orientation dependent. This effect was predicted theoretically by J. Stark [118] in 1912, and approved experimentally by Piercy *et al.* [92] in 1963.

Positivelly-charged particles like ions are repulsed from the nuclei of the plane, and after entering the space between two adjacent planes, they will be repulsed from the second plane. The moving ions thus tend to follow the direction between two neighboring crystalline planes at the largest possible distance from each of them.

At low energies the channeling effects in crystals are not present, but particle diffraction is dominating, since small-angle scattering at low energies requires large impact parameters, which become bigger than typical interplanar distances. At high energies the quantum effects and diffraction are less effective and therefore the channeling effect is present.

Simulation codes Trajectory simulation codes are conventionally classified into molecular-dynamics, binary-collision and Monte Carlo codes [109]. Molecular-dynamics codes solve Newton's equation of motion. This technique requires considerable computing power and is therefore not much in use. Binary-collision codes operate on a given target structure. The domain of this type of code is the slowing down in a regular crystal lattice, in particular under channeling[2] conditions.

Monte Carlo simulations for particle penetration imply a medium with randomly distributed constituents to be traversed. The prime input is a table of differential cross sections for elastic nuclear scattering as well as a table of electronic stopping cross sections and, possibly, electronic straggling. The best known simulation program is the TRIM/SRIM[3] code, developed by Ziegler and Biersack [144].

2.3 High Pressure

Pressure induces a variety of alterations in materials. First, compression involves typically the tendency to higher unit cell symmetries as well as to closer packing of atoms or molecules in the solid state, but furthermore, a higher pressure is tantamount to changes in electron hybridization, represented in the basic Hamiltonian at the level of elementary nuclear and electronic charges [40]:

$$\hat{H} = \hat{H}_{nn} + \hat{H}_{en} + \hat{H}_{ee} \tag{2.15}$$

where $\hat{H}_{nn}$ and $\hat{H}_{ee}$ are the kinetic energy of the nuclei and the electrons, respectively. $\hat{H}_{en}$ denotes the mutual Coulomb attractions. Due to the confinement of the constituents described by (2.15) in the volume V, the stationary states of the fundamental Schrödinger equation

$$\hat{H}\psi(V) = E(V)\,\psi(V) \tag{2.16}$$

[2] Charged particles moving along planes of symmetry in a crystal behave in an unusual way: They interact with nuclear planes or chains instead of with separate atoms.

[3] abbreviation for TRansport of Ions in Matter, in more recent versions called Stopping and Range of Ions in Matter. SRIM download from http://www.srim.org

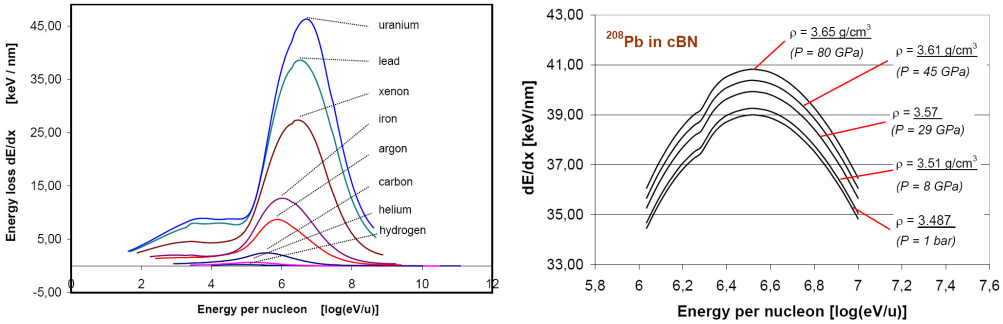

(a) SRIM code calculations for different ions in cBN

(b) SRIM code calculations for Pb irradiation in cBN at different pressures

Figure 2.5: Total energy loss as a function of the incident ion (a) and of the material density (b).

are functions of V and therefore alterable by pressure. Under this condition, electrons tend toward states of lower kinetic energy. This means, in general, a destabilization of intramolecular bonds [39] (Figure 2.6). Compression also alters both bandwidths and bandgaps, associated with major changes in electronic and magnetic states, including the formation of conductors [63] or even superconductors [70] from materials originally possessing substantial bandgaps. Wigner and Huntington suggested the phenomenon of pressure induced metallization already in 1935 [136]. Finally, pressure can affect the chemistry of substances by accelerating or kinetically inhibiting reactions, depending on the activation volume [137].

The stress and strain in a sample, caused by application of pressure, which is in general non-hydrostatic, is mathematically described by Cauchy's stress tensor σ_{ij} (2.17). Each individual tensor element represents the strain and the stress on a side of an infinitesimal cube, which itself is an infinitesimal constituent of the crystal as displayed in Figure 2.7. At perfect hydrostatic conditions only the tensor elements on the diagonal $\sigma_{i=j}$ are unequal to zero. A more extensive description is given elsewhere [77].

$$\sigma_{ij} = \begin{pmatrix} \sigma_{11} & \sigma_{12} & \sigma_{13} \\ \sigma_{21} & \sigma_{22} & \sigma_{23} \\ \sigma_{31} & \sigma_{32} & \sigma_{33} \end{pmatrix} \equiv \begin{pmatrix} \sigma_x & \tau_{xy} & \tau_{xz} \\ \tau_{yx} & \sigma_y & \tau_{yz} \\ \tau_{zx} & \tau_{zy} & \sigma_z \end{pmatrix} \tag{2.17}$$

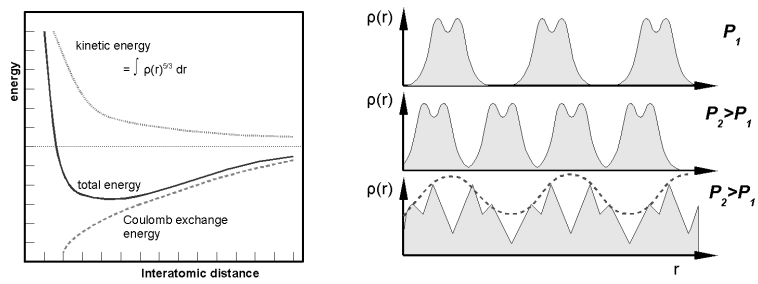

(a) (b)

Figure 2.6: Schematic of the effect of decreasing interatomic distance on the (repulsive) kinetic and (attractive) Coulomb exchange energies (a), and effect of compression on a chain of molecules showing the buildup of electron density between the molecules, and the possibility of symmetry breaking to form a charge transfer state (charge density wave) (b) (reference: [39]).

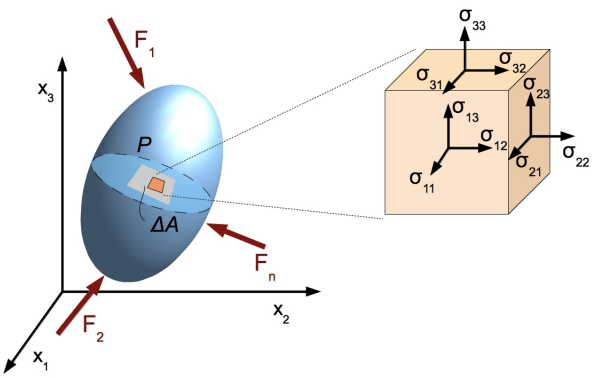

Figure 2.7: Stress and strain tensor component σ_{ij} represents the strain caused by a force acting along x_i on a face element normal to x_j.

2.4 Raman Spectroscopy

The phenomenon of inelastic scattering of light was first postulated by Smekal in 1923 [111] and first observed experimentally in 1928 by Raman and Krishnan [97].

Photons may be absorbed or scattered when interacting with matter. Otherwise, they will pass straight through, and the material appears transparent. Scattered photons can be observed by collecting light at an angle to the incident light beam. Provided there is no absorption from any electronic transitions, the efficiency increases with the fourth power of the incident light frequency. Un-

like infrared spectroscopy, which uses a wide range of frequencies of the beam applied to the sample in order to detect real vibration states of molecules by measuring the absorption frequencies, Raman spectroscopy works with a sole wavelength and therefore a laser beam of fixed wavelength is used in almost every application. In Raman scattering, the light interacts with the molecule and distorts (polarizes) the electron cloud around the nuclei to form a so-called *virtual state* which is not an eigenstate of the molecule. Further, the actual shape of the distorted electron arrangement will depend on how much energy is transferred to the molecule and hence is dependent on the applied laser frequency. The nuclei themselves possess too much inertial mass, making it impossible to follow the electron cloud movement. This results in a high-energy form of the molecule with a different electron geometry but almost always without any nuclear movement. Since no energy has been transferred after the electron cloud has relaxed and returned to its initial state, this is essentially an elastic process, which is called *Rayleigh scattering*.

The actual Raman scattering on the other hand is a much rarer event which involves only one out of $10^6 - 10^8$ of the photons scattered [112]. This occurs when the light and the electrons interact and the nuclei begin to move at the same time. Thus the relaxing electron cloud will end up at an appreciable higher (*Stokes*) or lower (*anti-Stokes*) vibrational state of the electronic ground state, which is illustrated in Figure 2.8. Most molecules at rest prior to interaction with the exiting light and at room temperature are likely to be in the vibrational ground state. Therefore the majority of Raman scattering will be Stokes Raman scattering. Nevertheless, since thermal energy is tantamount to vibrational energy, Raman spectroscopy can be seen as an outstanding tool for non-contacting temperature measurements even on microscopic specimens, only by comparing both Stokes- and anti-Stokes signals. The intensity ratio of the Stokes and anti-Stokes Raman scattering depends on the number of molecules in the ground and the excited vibrational levels and can be calculated with the Boltzmann equation,

$$\frac{N_n}{N_m} = \frac{g_n}{g_m} \exp\left[\frac{-(E_n - E_m)}{k_B T}\right] \tag{2.18}$$

N_n	is the number of molecules in the excited vibrational energy level (n)
N_m	is the number of molecules in the ground vibrational energy level (m)
g	is the degeneracy of the levels n and m
$(E_n - E_m)$	is the difference in energy between the vibrational energy levels
k_B	is the Boltzmann constant (1.3807×10^{-23} J/K)

Some vibrations can occur in more than one way but the energies of the different ways are the same, so that the individual components cannot be separately identified. The number of these components is called the degeneracy and is denoted by the symbol g in equation (2.18).

In Raman spectroscopy, a broad energy range of the scattered beam is being examined, beginning in the far anti-Stokes region and ending up with high energies of the Stokes region. The commonly used unit of the Raman shift (the difference to the Rayleigh scattered beam) is the wavenumber ν with the unit cm^{-1} (light waves per cm). Since anti-Stokes scattering is the less probable the colder the molecule or the crystal appears, it can be neglected even at room temperature. Furthermore, regarding the masses of the vibrating constituents it can be pointed out that heavier nuclei cause Raman modes emerging at higher wavenumbers due to a deeper quantum well with steeper walls, described by the Morse potential and accompanied by larger differences between each energy level.

Figure 2.9 illustrates the contrast to infrared spectroscopy. In order to yield a Raman signal, the dipole moment of the observed molecule must sustain, whereas the polarizability changes drastically when excited.

2.4.1 The polarizability tensor

When polarized light interacts with a molecule or with a bond in a crystal, the surrounding electron cloud will be distorted to a degree, that depends on the ability of the electrons to polarize - expressed by the *polarizability* α. Though

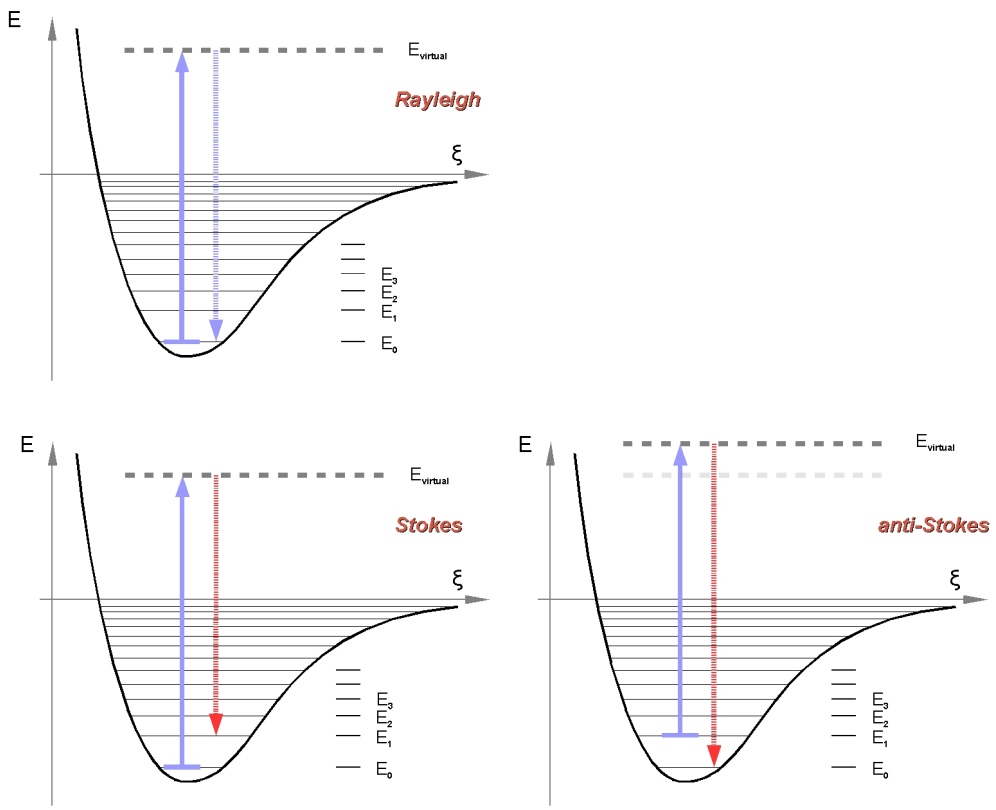

Figure 2.8: Principle of Rayleigh scattering (upper graph) and Raman scattering (lower graphs). In case the initial electronic state is below the state after excitation to the virtual state and subsequent relaxation, the process is called Stokes Raman scattering. When excitation and relaxation end up on a lower energy level as the initial state, the process is called anti-Stokes. ξ is the internuclear separation for the case of linear vibrations. The level of the virtual state depends only on the energy of the exciting photon.

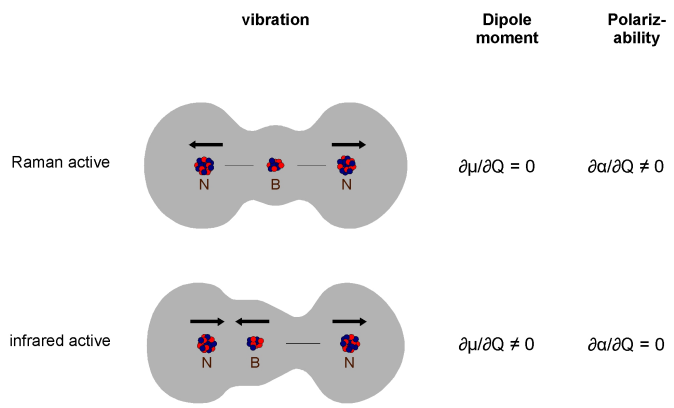

Figure 2.9: Electron cloud model of a boron nitride bond showing IR and Raman active vibrations. In order to obtain a Raman resonance, the dipole moment must not change when excited but the polarizability must change. Vice versa for obtaining an infrared signal.

the light causing the effect is polarized in one plane, the effect on the electron cloud is in all directions, and can be described as a dipole change in the molecule (or bonding) in each of the three Cartesian coordinates x, y and z. Therefore, three dipoles have to be considered in order to describe the effect on molecular polarizability. Simplified, a dipole μ occurs in the bond induced by the field from the incident photon E.

$$\mu = \alpha E \tag{2.19}$$

In order to connect the direction of the polarisability of the molecule and the polarization of the incident light, the polarizability of the molecule becomes a tensor,

$$\alpha_{ij} \tag{2.20}$$

at which the first subscript i refers to the direction of polarisability of the molecule and j stands for the polarization of the incident light. Hence, the expression for the induced dipole in x direction is $\mu_x = \alpha_{xx}E_x + \alpha_{xy}E_y + \alpha_{xz}E_z$. μ_y and μ_z can be derived by the same rule, which means conclusively

$$\begin{pmatrix} \mu_x \\ \mu_y \\ \mu_z \end{pmatrix} = \begin{pmatrix} \alpha_{xx} & \alpha_{xy} & \alpha xz \\ \alpha_{yx} & \alpha_{yy} & \alpha yz \\ \alpha_{zx} & \alpha_{zy} & \alpha zz \end{pmatrix} \begin{pmatrix} E_x \\ E_y \\ E_z \end{pmatrix} \tag{2.21}$$

2.4.2 Lattice modes in single crystals

In a single crystal all molecular axes are lined up within the unit cell. Thus, the polarization direction of the incident beam has a relationship to the molecular axes. Hence it is possible to analyse each component of the tensor (2.20). The induced vibration (or stopped vibration in the anti-Stokes case) corresponds to the hole lattice of the bulk, and can propagate in the same direction as the applied radiation, or perpendicular to it. The former results in a longitudinal or L Raman mode, and the latter in a transversal or T Raman mode.

Each mode consists of a very large number of vibrations of similar energy which occupy a band of energies in the material. The band width varies depending on the material, and each of these bands is called a lattice mode. If the electron cloud excitation takes place in such a manner that the ions vibrate against each other causing a charge separation, the modes are called optic modes and labelled $\mathrm{L_O}$ or $\mathrm{T_O}$, which occur in the Raman spectrum at higher energies. On the other hand, vibrations with ions oscillating in phase cause so-called acoustic modes at lower energies in the Raman spectrum. These acoustic modes are tagged as $\mathrm{L_A}$ or $\mathrm{T_A}$ (longitudinal acoustic and transversal acoustic, as for the optic modes, respectively).

Cubic boron nitride

cBN belongs to the zinc blende structure (Figure 2.1) and exhibits one Raman active optical phonon at Γ in the Brillouin zone, which is triply degenerated due to three possible spatial dimensions of vibration. Nevertheless, this mode splits into a transversal and a longitudinal phonon [98]. The $\mathrm{T_O}$ phonon is at $1055\,\mathrm{cm}^{-1}$ and the $\mathrm{L_O}$ phonon at $1304\,\mathrm{cm}^{-1}$ (Figure 3.7).

Hexagonal boron nitride

hBN, which consists of graphite-like planes, provides one major Raman resonance at $1364\,\mathrm{cm}^{-1}$. Since the hexagonal layers posses a two-dimensional geometry, the phonon eigenvector of this mode is a doubly degenerated in-plane optical mode and reveals E_{2g} symmetry. As displayed in Figure 2.10 a and Figure 3.7, the B and N atoms of each plane oscillate in opposite directions within the plane but parallel with the atoms of the adjacent layer. And exactly this parallel movement is responsible for the dipole cancellation observed perpendicular to the layers. Thus, the E_{2g} mode does not have an L_O-T_O splitting. In contrast, the anti-parallel optic vibrational E_{1u} mode (Figure 2.10 b) is infrared active and has a large L_O-T_O splitting.

A second Raman active vibration at very low wavenumbers ($55\,\mathrm{cm}^{-1}$) was detected by Nemanich [82]. This acoustic phonon, where the two BN planes slide against each other, as depicted in Figure 2.10 c, was not detectable within our investigations due to the cutoff of the notch filter at ca. $80\,\mathrm{cm}^{-1}$. Further *ab initio* calculations [98] predict another low-energy vibration caused by a rigid movement of the planes against each other in c axes direction (Figure 2.10) at $125\,\mathrm{cm}^{-1}$, which is neither Raman nor infrared active and therefore not detectable in our experiments. Finally, the acoustic mode E_{1u} at which the atoms move parallel and without any difference in phase is of course not measurable using Raman spectroscopy.

Wurtzitic boron nitride

Karch *et al.* [56] suggested four Raman active phonon modes in wBN, resulting from the splitting of both A_1 and E_1 modes into L_O and T_O components. Ohba *et al.* [87] came to the same conclusion with analog results for the corresponding Raman shifts. Both calculations confirm the first experimental data for the E_1 L_O as well as the A_1 T_O mode measured by Doll [23]. Another investigation by Sachdev [104] yields similar Raman shifts for each mode. These findings are summarized in Table 2.5. Since wBN does not decompose only when existent as nano size powder, it is very difficult to obtain Raman signals.

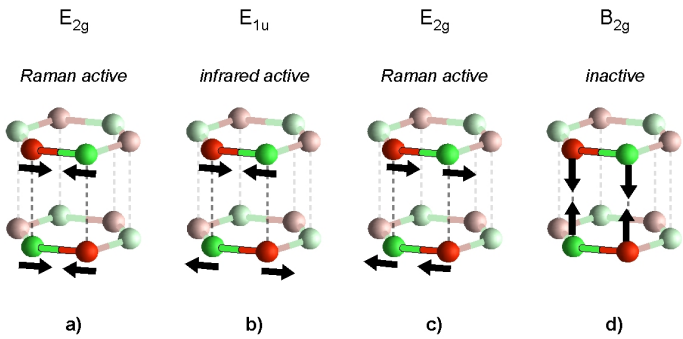

Figure 2.10: Vibrational modes in boron nitride. Only the E_{2g} phonon in a) is detectable using our Raman spectrometer. The E_{2g} phonon in *cl* is cut off by the notch filter, and the contributions of the B_{2g} phonons cancel each other.

Table 2.5: Calculated and measured Raman active modes for wBN (A_1, E_1).

	Raman shift / cm^{-1}			
modes	E_1 (L_O)	A_1 (L_O)	E_1 (T_O)	A_1 (T_O)
Karch [56] (calc.)	1281	1258	1053	1006
Ohba [87] (calc.)	1293	1280	1075	1043
Doll [23] (exp.)	1295	–	–	1015
Sachdev [104] (exp.)	1285	1246	1108	1016

2.5 X-ray Diffraction

Due to their wave character, X-rays obey Huygens' principle, and thus scatter on a diffraction grating when the lattice parameters are in the range of the wavelength of the incident beam. Since X-ray wavelengths are in the range of 1 pm up to 10 nm they can be used for resolving crystal structures. Unlike neutron diffraction, where the scattering takes place on the nuclei of the solid-state body, the X-rays scatter on the electron clouds of the material, and the scattered waves interfere with each other. This interference is constructive when the phase shift of two parallel reflected beams is a multiple of 2π. This condition is expressed by Bragg's law [13]:

$$n\lambda = 2d\sin\theta \tag{2.22}$$

where n is an integer determined by the order given, λ is the wavelength of the X-rays, d is the spacing between the planes in the atomic lattice, and θ is the angle between the incident ray and the scattering planes. The principle of Bragg's interference conditions is displayed in Figure 2.11. If a bundle of parallel lattice planes fulfills the Bragg equation, the contributions of each single plane superimpose in a manner that constructive interference gives rise to detectable signals under the so-called Bragg angles with a value of 2θ between the scattered and the non-scattered beam. Since the wavelength λ is known, one can easily obtain the lattice plane spacings d_{hkl}. (hkl) are the Miller indices, specifying the position of the parallel lattice planes in the reciprocal lattice. Therefore, if the crystal system is known, the lattice constants of the crytallographic unit cell can be derived from d_{hkl}. E.g., for the cubic crystal system via

$$\frac{1}{d_{hkl}^2} = \frac{h^2 + k^2 + l^2}{a^2} \tag{2.23}$$

with a denoting the lattice constant of the cubic unit cell.

2.5.1 Analysing methods

Depending on whether the system to investigate is a single crystal or a powder sample, mainly two analysing methods are of particular interest. On the

one hand, the *Laue method* is applied for single crystals using white, non-monochromatic X-ray radiation (bremsstrahlung) as depicted in Figure 2.12 (a). Thereby, constructive interference appears if and only if the change in the wave vector during the scattering process is equal to a reciprocal lattice vector. The result is a scattering image of point reflections.

On the other hand, when powder samples are to be investigated (which was the case in this study), the *Debye-Scherrer method* is of particular interest (Figure 2.12 (b)). Unlike single crystals, a powder sample possesses ideally every possible crystalline orientation randomly distributed and therefore the resulting diffraction image consists of smooth concentric rings around the beam axis. Powder diffraction data are usually presented as a diffractogram in which the diffracted intensity is shown as function either of the scattering angle 2θ or of the scattering value d fulfilling (2.22). The latter variable has the advantage that the diffractogram does no longer depend on the value of the wavelength λ and therefore is independent of the X-ray source. The major difference to the Laue method is the monochromatic beam.

2.5.2 The phase problem

The primary object of the crystal structure analysis is to find the positions of the centers of the atoms given by the maxima in the electron density function $\varrho(r)$[4] and to identify the atoms present from the relative weights of these maxima. Due to the lack of applicable optical devices to steer the X-rays, only the intensity of the scattered beam is detectable. All other information such as phase relations is not accessible, in spite of their importance in terms of determining the electron density $\varrho(r)$. This phenomenon is known as the *phase problem* [20]. However, the measured intensity I is proportional to the square of the structure factor F,

$$I_{hkl} \propto |F_{hkl}|^2 \tag{2.24}$$

and the structure factor F is the Fourier transform of the electron density $\varrho(r)$:

[4] Except the hydrogen atoms, where the maximum of the electron density is on the bonding to the neighbouring atom.

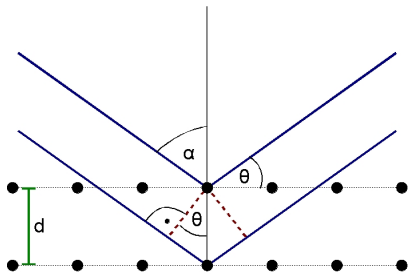

Figure 2.11: Principle of Bragg's scattering geometry. d is the lattice plane spacing and $theta$ the scattering angle. Positive interference occurs if the phase shift of the emitted beams is a multiple of 2π. The black spheres represent the atoms of the material.

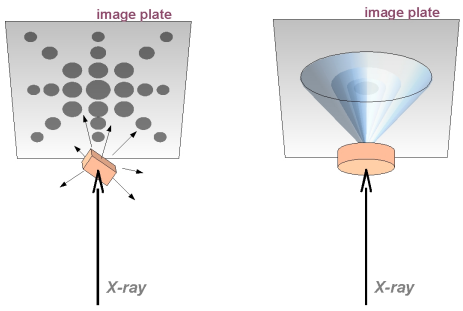

(a) Laue method (b) Debye-Scherrer method

Figure 2.12: X-ray diffraction methods using a "white" X-ray beam for single crystals (a) and monochromatic X-rays for powder samples (b).

$$F_{hkl} = \int_0^a \int_0^b \int_0^c \rho\left(x, y, z\right) \exp\left[2\pi i \left(\frac{hx}{a} + \frac{ky}{b} + \frac{lz}{c}\right)\right] \mathrm{d}x\mathrm{d}y\mathrm{d}z \tag{2.25}$$

Here, abc are the lattice constants, xyz the spatial coordinates in the unit cell, and hkl the Miller indices. Hence, the phase problem has to be solved in order to derive the structure factors from the measured intensities. Besides the *direct methods*, developed by Hauptmann and Karle [38] as well as the *Patterson method* [90, 91], which both solve the Fourier transform (2.25), methods using structure refinement have been prevailing. The refinement methods use the structure factor F as a sum of all atomic scattering factors f of a unit cell:

$$F_{hkl} = \sum_j^N f_j \exp\left[2\pi i \left(hx_j + ky_j + lz_j\right)\right] \tag{2.26}$$

Thus it is to sum over all N atoms j in the unit cell. xyz are the coordinates of the atom j, and f is the Fourier transform of the electron density of one atom. Structure refinement methods now change the coordinates until the difference between the experimentally obtained structure factor F_{hkl} and the structure factor F_{hkl} derived from (2.26) is minimized. A mathematical tool, which is used to solve this problem is the method of the least squares, applied in procedures as the Rietveld refinement method.

3 Experimental

3.1 Specimen Fabrication

3.1.1 Single crystals

The temperature gradient method was applied by Taniguchi et al. in order to grow high-purity hBN and cBN single crystals using a modified belt-type HP-HT apparatus with a 60 mm bore diameter [122, 123]. As a BN source, hot pressed hBN discs (Denka Co. Ltd., Japan, type N1) and powder hBN (Denka Co. Ltd., Japan, type JP) were heated at 2100 °C for 2 h in a nitrogen flow in order to remove residual oxygen. Remanent oxygen as well as carbon were of the order of 10^{19} and 10^{21} $^{\text{atoms}}/_{\text{cm}^3}$, respectively[1]. The carbon impurities originated from the graphite furnace used for this work. As solvent served a barium boron nitride ($Ba_3B_2N_4$)[2]. Both the samples and the solvent were embedded in a molybdenum sample chamber inside a nitrogen purged glove box in order to keep the oxygen and humidity level as low as possible. The specimen was then compressed between 4 and 5.5 GPa while heated between 1500 and 1650 °C for up to 80 h. The detailed experimental procedure has been described by Taniguchi in Ref. [123]. As displayed in Figure 3.2, exposure to pressures up to 4.6 GPa resulted in the growth of hBN crystals, regardless of the applied temperatures. On the other hand, when pressure exceeded 4.6 GPa, Taniguchi obtained cBN single crystal samples, whereas there is a small region in the P-T diagram

[1] SIMS standard specimen for meassuring the oxygen and carbon concentrations was prepared by HP reaction sintering from hBN at 7.7 GPa and 2100 °C without additives. Samples implanted with 60 keV ^{16}O or 55 keV ^{12}C ions were prepared to achieve concentrations of 10^{15} $^{\text{ions}}/_{\text{cm}^2}$ [121].

[2] ($Ba_3B_2N_4$) was synthesized by reacting barium nitride (Ba_3N_2) and BN at 1000 °C in a dry N atmosphere [121].

which delivers a mixture of both hBN and cBN crystals. After the HP-HT procedure, the molybdenum sample chamber was dissolved using hot aqua regia in order to obtain the crystals, which were subsequently characterized using SEM, cathodoluminescence spectroscopy, and Raman spectroscopy.

Near the phase equilibrium line between cBN and hBN at ca. 4.5 GPa and 1500 °C, both cBN and hBN crystals precipitated simultaneously in the growth chamber.

3.1.2 Powder samples

Both cBN and hBN powder samples (Figure 3.1 (a–e)) were obtained from Sigma-Aldrich®. The wBN powder samples (Figure 3.1 (f)) were made by a HPHT synthesis by Dubrovinskaia [25] starting with pyrolytic graphitelike boron nitride (pBN) precursor material, which was exposed to pressures from 7 up to 20 GPa for several hours using a multianvil press [24]. For the samples at 7 GPa no phase transformation into wBN was observed below a temperature of 1900 K, wheras the samples at the highest pressure of 20 GPa already initiated phase transition into wBN at a temperature of 1600 K.

3.2 Generation of High Pressure

Among various types of pressure generating devices, the diamond anvil cell (Figure 3.3) turned out to be most suitable for heavy ion irradiation experiments. On the one hand, the highest static pressures of up to 550 GPa [138] have been induced with a DAC[3]. Compared to other techniques, the usage as well as the transport of DACs is easy, and moderate pressures can be reached quickly. Another big advantage, the transparency of the diamond anvils, allows a direct view into the sample chamber, and several optical methods as laser heating or Raman spectroscopy can be realised *in-situ*. Not least these virtues give rise to the occurrence of many interesting discoveries [5].

[3] The highest pressure reached during working on this thesis was ≈100 GPa in a DAC with cullet sizes of 450 µm.

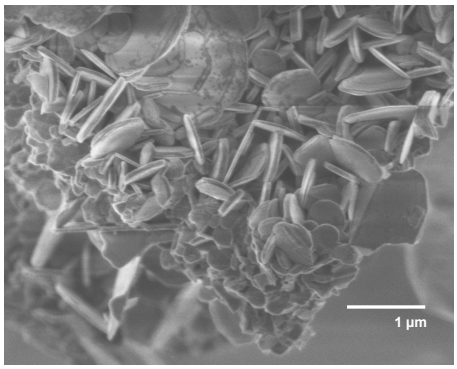

(a) hexagonal

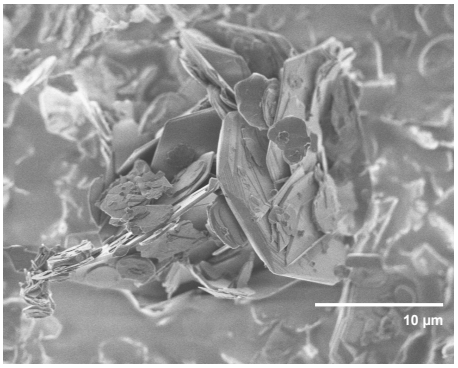

(b) hexagonal

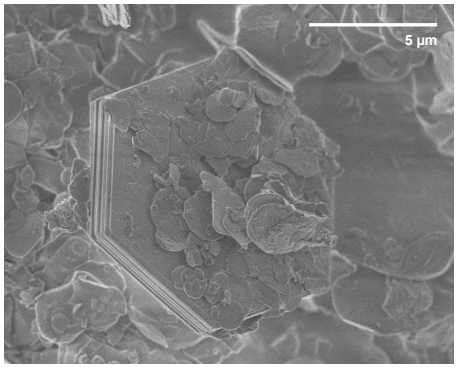

(c) hexagonal

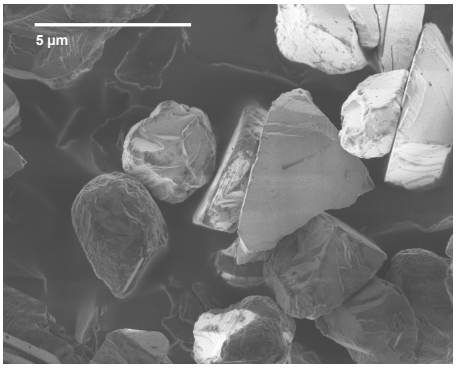

(d) cubic

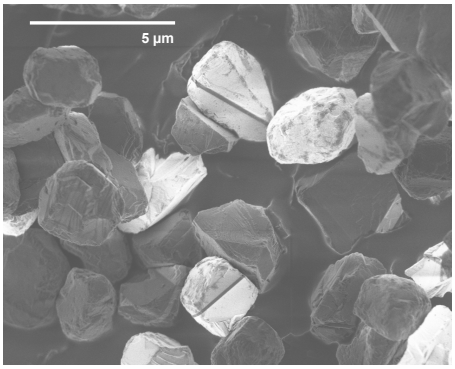

(e) cubic

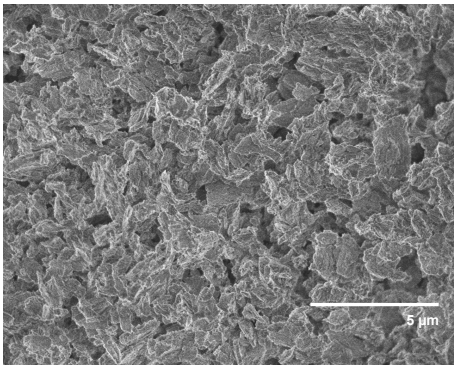

(f) wurtzitic

Figure 3.1: SEM micrographs of several BN powder samples. (a)–(c) hexagonal BN, (d) and (e) cubic BN, (f) wurtzitic BN.

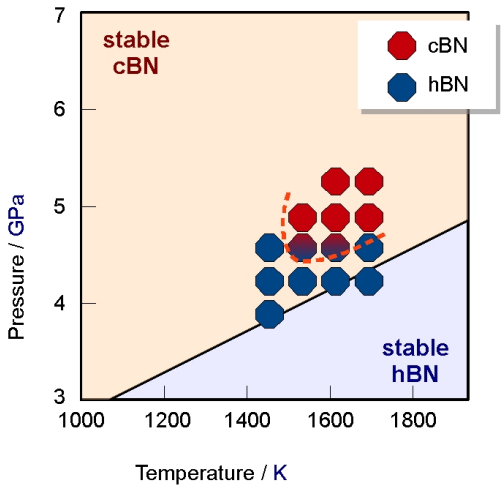

Figure 3.2: Reaction boundary in the *P*-*T* phase diagram for the single crystals obtained from Taniguchi [121]. The two-colored octagons correspond to co-existing of hBN and cBN in the recovered sample.

Alignment The main parts of a DAC are two opposing diamonds, each mounted on a backing plate, which itself is moveable and tiltable usually via screws in order to ensure parallel cullet areas as well as accurate alignment in which a diamond facet has to be right over a facet of the opposing diamond. Control of parallelism is managed using Newton's rings. In order to prevent damage of the diamond, and because the gems have to be very close to each other, it is recommended to place a thin, soft, and transparent plastic snippet between the diamonds during the procedure of alignment. An insufficient positioning of the anvils causes damage of the (below mentioned) gasket.

Gasket The gasket serves for many reasons: encapsulating the specimen, additional anvil stabilization, and delivering of force perpendicular to the diamonds. As gasket material was applied stainless steel for moderate pressures[4], or rhenium for highest pressures.

The first step of preparation is the preindentation of the gasket material down to a thickness of typically 60 - 110 µm using the anvil cell with the already aligned diamonds. It is important to pay attention to a uniform turning of the setscrews

[4] up to 20 GPa for powder samples without pressure transmitting medium and up to 10 GPa for samples with pressure transmitting medium

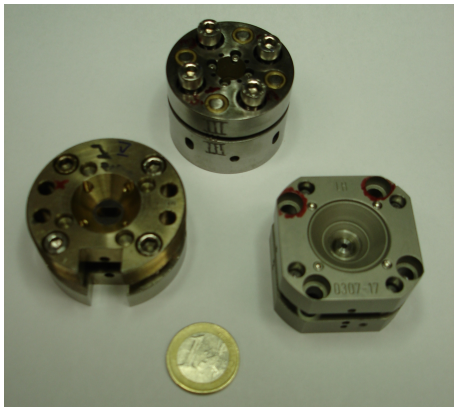

(a)

Figure 3.3: Different types of diamond anvil cells (a), and an opened DAC with its constituents (b).

in order to remain parallelism. Now a small hole has to be drilled through the indented gasket area. In order to do so, we used mechanical drills with diameters of 100 - 300 µm when using gaskets made of stainless steel. Rhenium gaskets were "drilled" using a spark erosion machine or a pulsed laser beam.

Sample insertion After a thorough gasket and diamond cleaning as well as the gasket re-positioning onto a diamond, the two anvils have to be put together again to ensure a perfect fit of the gasket on the diamond. Specimen(s) can now be given into the bore using a very thin needle. Ruby chips, serving as pressure calibrants are put beside the crystal or into the powder as well.

Pressure transmitting medium Since the crystal in the sample chamber needs to be surrounded by non-compressible matter, which ensures hydrostatic conditions around the sample and the pressure marker, a pressure transmitting medium has to be added. A mixture of methanol and ethanol at a ratio of 4 to 1 provides hydrostaticity up to ≈10 GPa, which can be improved to a certain degree by adding water up to a ratio of 16:3:1 for methanol:ethanol:water. In case the experiment requires hydrostaticity[5] of up to 30 GPa, argon is an appropriate

[5]sufficient hydrostatic conditions be given if P does not differ more than 0.5 GPa within a sample chamber of $\varnothing = 200\,\mu m$

pressure transmitting medium [108], which has to be loaded cryogenically. However, helium is unquestionably the best available pressure transmitting medium, even in its solid state above 12.1 GPa at 300 K. It provides hydrostaticity up to pressures of 50 GPa [120]. Helium has not been applied within this thesis. However, the most established pressure transmitting media were studied thoroughly by Klotz *et al.* [59].

Pressure adjustment The small ruby chips serve for the pressure setting using the R_1 luminescence line, which is easily collected with a spectrometer. This line is strongly pressure dependent and obeys (3.1) according to investigations of Mao *et al.* [72, 73].

$$P = \frac{19.04\,\mathrm{GPa}}{B}\left(\left[\frac{\lambda_0 + \Delta\lambda}{\lambda_0}\right]^B - 1\right) \tag{3.1}$$

After experiments in 1978 using a methanol-ethanol blend, the value B was set to 5. Measurements, carried out in 1986 with argon as pressure transmitting medium, which sustains hydrostaticity up to 77 GPa and delivers quasi-hydrostatic conditions at higher pressures, gave rise to a value of 7.665. P in (3.1) is in Mbar and λ is the wavelength in nm. $\lambda_0 = 694.2$ nm is the wavelength of the R_1 luminescence ruby line at a pressure of 1 bar. Current standard for pressure determination is a value of $B = 7.715$ [143]. Nevertheless, improvement of the ruby scale is a continuous request. Holzapfel *et al.* [43] proposed an extension of eq. (3.1) as:

$$P = \frac{A}{B+C}\left(\exp\left\{\frac{B+C}{C}\left[1 - \left(\frac{\lambda}{\lambda_0}\right)^{-C}\right]\right\} - 1\right) \tag{3.2}$$

With $A = 1820$ GPa, $B = 14$, and $C = 7.3$, at which the latter is pressure dependent. Eq. (3.2) has not been used because of uncertainties and high error values.

A different approach to measure the pressure has been undertaken to use the diamond Raman mode of the anvil itself [2, 27]. Though it is very tempting, the difficulties due to the emerging and by no means negligible pressure gradient

within the anvil, it is not recommended to use it for pressure measurements. Nevertheless, Baer *et al.* [2] suggested the formula

$$\nu\left(\mathrm{cm}^{-1}\right) = \nu_0 + aP + bP^2 \tag{3.3}$$

which describes the Raman band shift as a function of pressure, where a ranges between 2.301 for a 50 µm bevel on a 400 µm culet area, and 2.709 for a non-bevelled culet face with $\varnothing = 300\,\mu\mathrm{m}$ (b from -1.702×10^{-3} and -0.517×10^{-3}, respectively; ν_0 is a constant of $1332.4\,\mathrm{cm}^{-1}$).

3.3 Swift Heavy Ion Irradiation

3.3.1 Unilac

The Universal Linear Accelerator (abbr. Unilac) (Figure 3.4 a) of the GSI Helmholtz Centre for Heavy Ion Research[6] has been built in order to accelerate ionised atoms up to energies of 11.4 MeV/u without limits regarding the nucleus mass. This enables us to irradiate samples at ambient pressure conditions with virtuelly all stable elements of the periodic table. The main Unilac components comprise one high-charge injector, two high-current injectors, a gas stripper as well as foil strippers serving for ionisation of the projectiles. The actual speed-up is realised by an Alvarez accelerator[7] of 120 m length. Irradiations took place in the X0 site in the Unilac experimental hall. For more detailed information see [47].

3.3.2 SIS18

The heavy ion synchrotron of GSI (Figure 3.5 a) delivers ions within energy regimes of 50 up to 2 GeV/u for all elements up to uranium, and up to 4.5 GeV for protons [48], which is tantamount to 90 % of the speed of light. Energies of this magnitude are necessary in order to interpenetrate the first diamond of the DAC. Irradiation site is the cave A inside the SIS target hall.

[6] www.gsi.de
[7] a cavity resonance accelerator

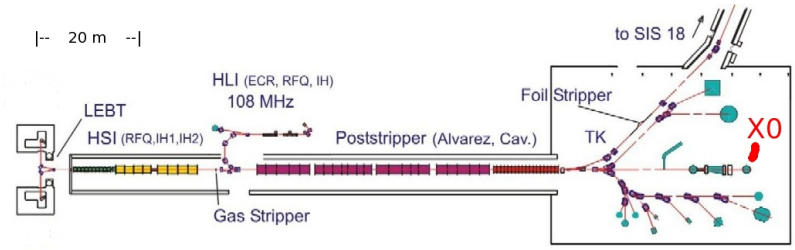

Figure 3.4: Scheme of the Unilac, taken from [47]. HSI - high current injector; LEBT - low energy beam transport; HLI - high charge injector; TK - beam transfer line.

3.4 Examination Methods

3.4.1 Raman spectroscopy

In order to obtain information about polarizability properties of the samples we used the Raman spectrometer HR800 from HORIBA Jobin Yvon™. It works with red light of a laser at the wavelength $\lambda = 632.817\,\mathrm{nm}$, polarized 500:1. Though the device itself is designed to use multiple lasers with different wavelengths, in our case only the above mentioned laser is available, which is a 17 mW He/Ne laser. An integrated holographic band-stop or notch filter is applied in order to cut off the Rayleigh scattered beam. Since a notch filter is specific for one wavelength, changing the exciting wavelength requires changing the notch filter. Six further neutral optical density filters (Table 3.1) are available for the reduction of the laser beam intensity, whereas the optical density D affects the intensity in the manner of $I = I_0 \times 10^{-D}$.

For microscopy needs, short working distance objectives with magnifications of ×5, ×10, ×50, and ×100 are available, as well as two objectives with long working distances and magnifications of ×25 and ×50. Long working distances are necessary in order to focus into the DACs. Sample illumination is realised in the transmission as well as in the reflection mode. Using these objectives, beam spots of 2 µm are realisable.

The spectrograph entrance confocal aperture is furthermore adjustable between 0 and 1,000 µm in a stepless mode in order to change spatial and spectral resolution as well as to manipulate the intensity of the re-emitted Raman signals. The spectograph is an asymmetric Czerny Turner optimized for flat field and

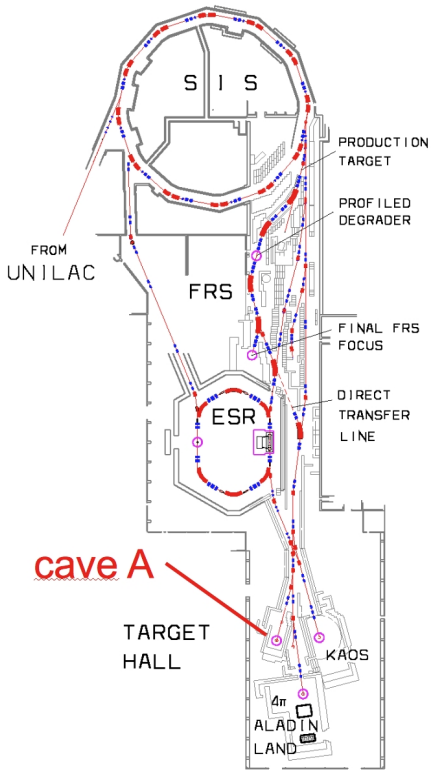

Figure 3.5: Scheme of the SIS18 with its adjacent beamlines and irradiation sites. SIS - Schwerionensynchrotron; FRS - Fragmentseparator; ESR - Elektronenspeicherring.

optical aberrations. Gratings are mounted one kinematic interchangeable holders. Standard grating is 1800 grooves/mm, while the second on is 600 grooves/mm. The former grating delivers exemplarily and in combination with a 100 µm hole a spectral resolution of 0.6 cm^{-1} and 3.9 cm^{-1} at the spectral positions of 810 nm and 400 nm, respectively.

Signal detection is carried out using a cooled CCD detector with a standard of 1024×256 pixels of 26 µm each. The collected data are displayed and the sample is being moved via the LabSpec software, allowing data mapping, spectrometer calibration[8], and data analysis. This program is a product of HORIBA Jobin Yvon™, too.

Detailed information about the device usage as well as the software applica-

[8] calibration via the 520.7 cm^{-1} Raman band of Si and the zero point, where Rayleigh scattered light is being collected.

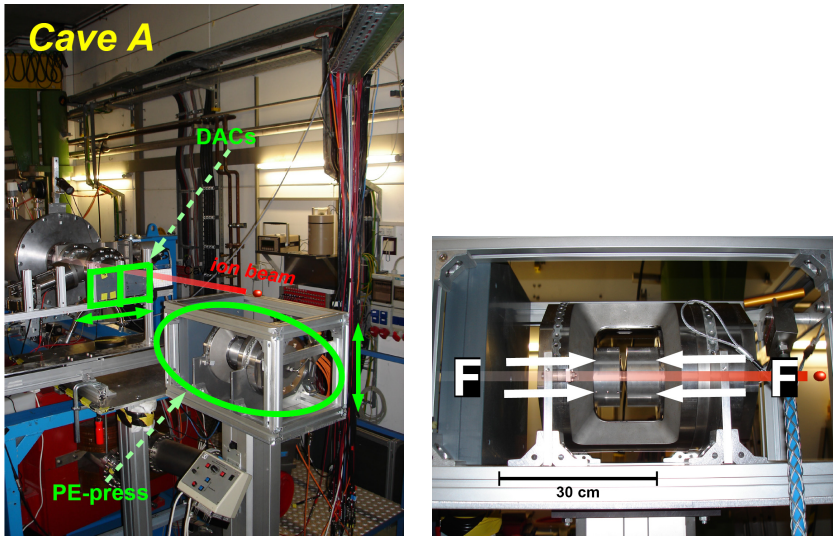

(a) (b)

Figure 3.6: High energy irradiation site "cave A" (a) and close-up of the Paris Edinburgh press (b), which contains anvils made of sintered cBN.

tions are displayed in the manuals [44, 45].

3.4.2 X-ray diffractometry

Ex-situ

Powder XRD was conducted on a Philips™PW 3710 diffractometer with a Cu anode using 40 kV generator voltage, 30 mA generator current and a secondary monochromator.

In-situ

Since both boron and nitrogen are weak X-ray scatterers and the diamond anvils absorb too much beam intensity, very intensive high-energy X-rays are necessary in order to obtain insight into pressurized BN samples. Only synchrotron sources deliver beams with these properties, and among them, the European Synchrotron Radiation Facility (ESRF) is one of the most powerful facilities. We used beamline ID27 (Figure 3.8), which is meant for high-pressure experiments. The wavelength of the X-rays was constant over the entire beamtime

Table 3.1: Available neutral density filters and the resulting intensity reduction.

optical density	–	D0.3	D0.6	D1	D2	D3	D4
attenuation/I_0	no	$\frac{1}{2}$	$\frac{1}{4}$	$\frac{1}{10}$	$\frac{1}{100}$	$\frac{1}{1{,}000}$	$\frac{1}{10{,}000}$

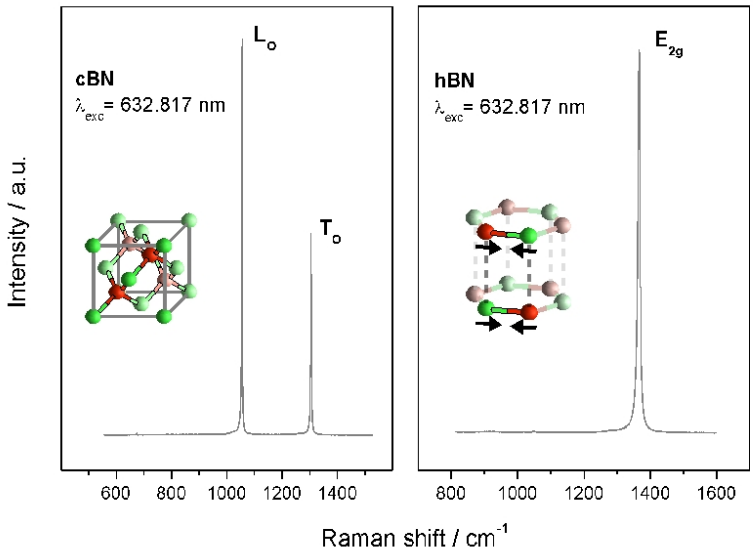

Figure 3.7: First-order Raman spectra of (left) cubic and (right) hexagonal boron nitride excited with $\lambda_{\text{exc}} = 0\,\text{nm}$. The insets show the crystal structures of the BN allotropes and the vibration mode.

with 0.3738 Å, and the beam spot diameter was 6 µm. The distance between specimen and detector was 352.583 mm; gauged with a Si standard.

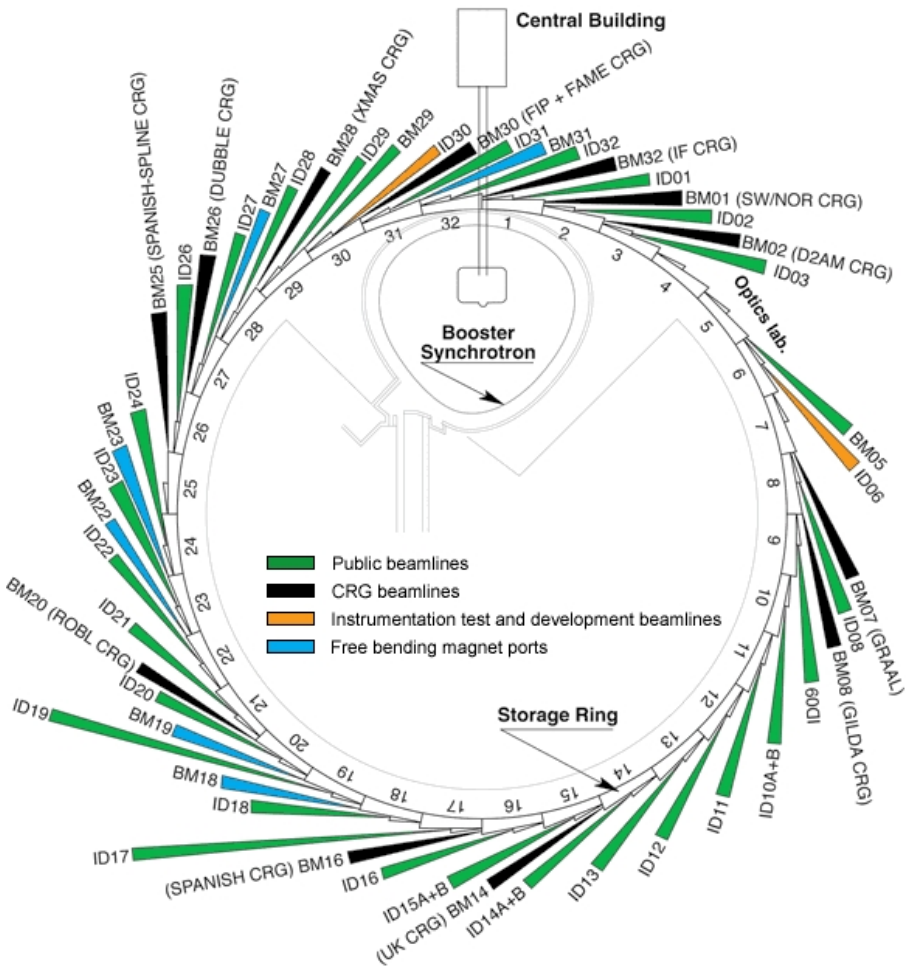

Figure 3.8: Plan of the ESRF experimental hall, taken from www.esrf.eu. Measurements took place at the high-pressure beamline ID27.

4 Results

4.1 Structural Changes under Ambient Pressure Conditions

Amorphization and irradiation hardness

All three available boron nitride allotropes have been exposed to several energies, ion masses and fluences in order to observe structure changes via Raman spectroscopy and X-ray diffraction. First experiments were carried out on powder samples, which adhere on stainless steel plates using isopropanol. After irradiation with 8.6 MeV/u Pb ions at the Unilac and a deactivation time of one month, Raman spectra have been recorded in the 20 s mode. Figure 4.1 displays spectra of samples before and after irradiation at fluences of up to 1.5×10^{13} ions per cm^2, all showing increased Raman background and decreased Raman bands. Wurtzitic BN powder does not show prominent Raman bands, and Pb ion irradiation did not reveal changes in the spectra (not shown here).

X-ray diffraction data are displayed in Figures 4.2, 4.3 and 4.4 for hBN, cBN and wBN powder samples, respectively. Due to instrumental standards, the powder samples had to be placed on glass plates, and therefore a significant longer deactivation time was necessary since glass is more easily to activate than steel. Unfortunately, effects originated from ionizing radiation of the activated glass can not be excluded entirely. Each diffractogram of the different BN forms shows slightly decreased reflections, although this effect is less pronounced than the band maximum decrease in the Raman spectra.

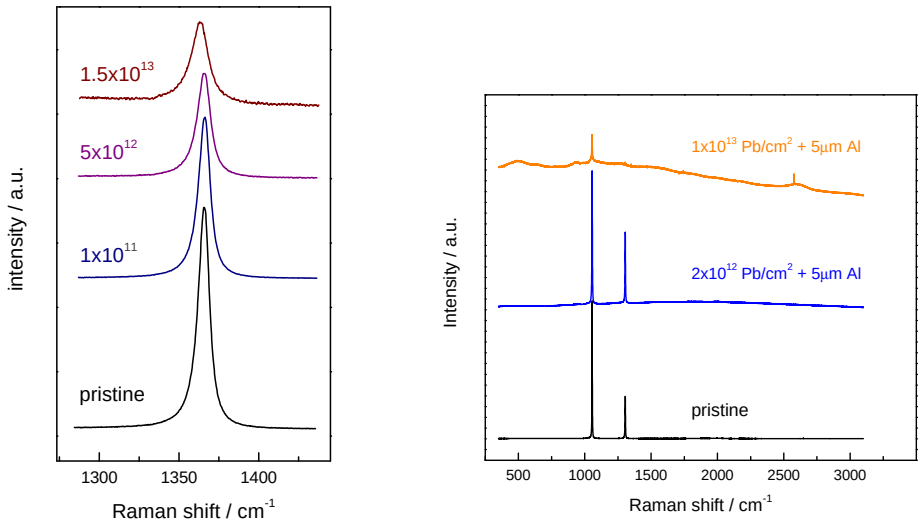

(a) (b)

Figure 4.1: Raman spectra of hBN (a) and cBN (b) irradiated with 8.6 MeV/u Pb ions at Unilac. Energy loss at the surface of the material was 21.0 ± 2.1 keV/nm for hBN and 32.5 ± 3.3 keV/nm for cBN, respectively.

Colourization

Single crystal cBN specimens have been glued on glass fiber (Figure 4.8) and irradiated at the irradiation site cave A with uranium ions of energies of 218 MeV/u. In addition to a color change from brownish-white to orange, Raman spectroscopy revealed a significantly increased LO band compared to the TO band as displayed in Figure 4.9. Furthermore, all measurements reveal new Raman bands at 1712 cm^{-1} and 2080 cm^{-1}. The hBN single crystals, on the other hand, have been irradiated in an orientation dependent manner, because physical properties are strongly anisotropic (see Table 2.4). After irradiation with 10^{13} Au ions per cm^2 at X0, the difference due to orientation is visible to the naked eye as depicted in Figure 4.5. Crystals exposed to the beam perpendicular to the a axis (parallel to the hexagonal, graphite-like layers) turned the color from white into a deep crimson tone. Astonishingly, crystals, that have been irradiated parallel to the a axis retained white.

In order to investigate such a phenomenon more systematically, a second

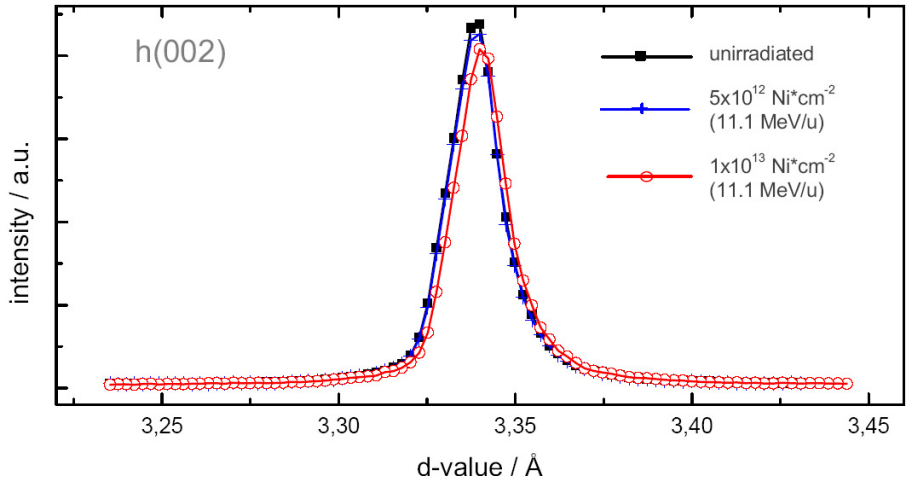

Figure 4.2: Powder XRD on hBN at atmospheric pressure. The (002) reflection as the major signal before ion bombardment and after two different fluences of nickel ions shows a decrease in height, but the diffraction background remains constant.

irradiation series has been conducted at X0 with fluences of up to 1×10^{13} Au ions per cm^2 and energies of 11.1 MeV/u. Figure 4.6 depicts the six crystals, of which three have been irradiated perpendicular to a and three parallel to a. Exemplarily one pristine crystal is also shown. As observed earlier, the color change took place again only for the hBN crystals with the hexagonal layers perpendicular to the ion beam. Nevertheless, the ratio between the E_{2g} Raman band and the Raman background converges to 1 in terms of fluence for both orientations with respect to the ion beam. The Raman scattered light has been also collected from both orientations, the ratio ζ behaving in the same manner for both cases (see Figure 4.7). Error bars for the ζ values are in all cases the root mean square deviations derived from at least five measurements on each sample and each orientation. Due to the obvious hexagonal shape of the hBN (Figures 4.5 and 4.6) no orientation check via e.g. XRD was necessary. Fluences, derived by a SETRAM and calibrated using a Faraday cup, are in the range of 10 % of the plotted value.

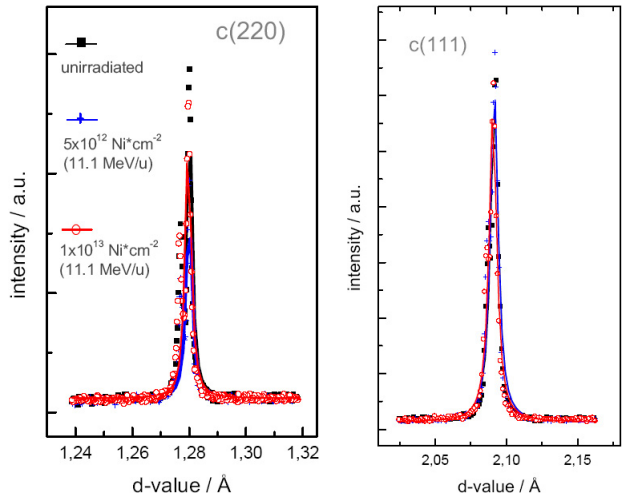

(a) (220) reflection (b) (111) reflection

Figure 4.3: Powder XRD on cBN at atmospheric pressure, representing the most intense cBN reflections.

4.2 hBN Single Crystals Irradiated Under Different Pressures and Orientations

Investigations of crystals, irradiated at different orientations, have been extended to the influence ot the parameter pressure. Two hBN crystals were inserted in a DAC - one with the hexagonal layers perpendicular and the other parallel to the ion beam. The former lays on the diamond surface, the latter clamps on the inner gasket wall. Figure 4.10 illustrates this arrangement. After filling the gasket aperture with a methanol-ethanol mixture, the samples have been pressurised, irradiated in cave A and, after a sufficient deactivation time, investigated by Raman spectroscopy. However, since the diamond Raman background differs too much from point to point of the anvil area, and interferes with the signal from the hBN E_{2g} vibration, no useable informations could be obtained under *in-situ* conditions. Therefore, the cells had to be opened, and the samples were being investigated under ambient pressure conditions. Comparisons of the E_{2g} Raman band before and after irradiations at three different pressures and for both orientations are depicted in Figures 4.11 and 4.12. All irradiations cause a trend to equalization of the Raman band maximum and the surounding Raman background, which is summarised in Figure 4.13. Here, the

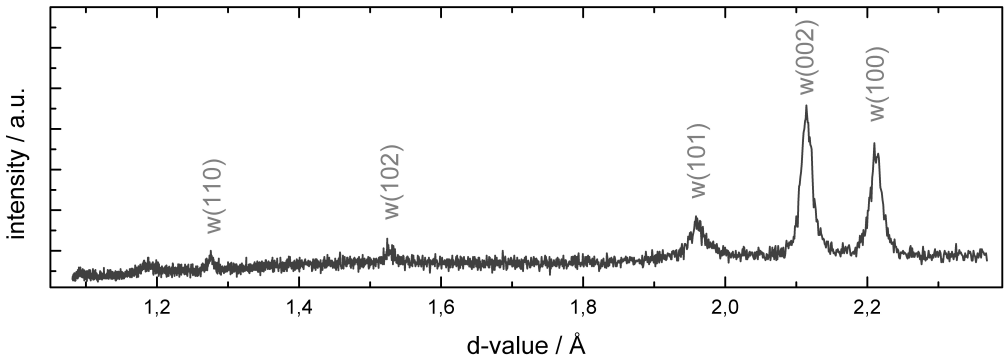

(a) entire diffractogram

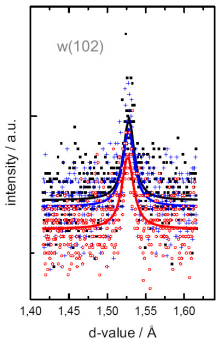

(b) (102) reflection

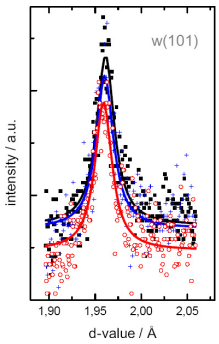

(c) (101) reflection

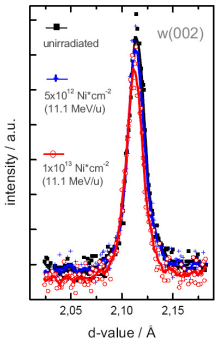

(d) (002) reflection

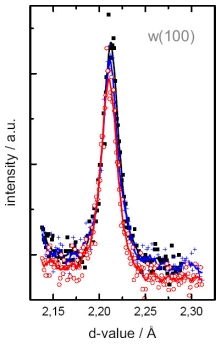

(e) (100) reflection

Figure 4.4: Powder XRD on wBN at atmospheric pressure before ion irradiation (a), and reflection close-ups showing comparisons to irradiated material (b–e). No significant evidence of ion-induced amorphization can be deduced by XRD.

crystals irradiated parallel to the a axis behave pressure independent, whereas the samples with the a axis perpendicular to the ion beam seem to resist the beam influence, the more likely the higher the pressure. A summary of the experimental parameters is given in Table 4.1, where the errors being about 2 % for E_{ion}, 10 µm for the diamond length, and 10 % for the fluences. The error for the energy loss can reach values of 20 % due to many steps in the calculations for the SIS irradiations.

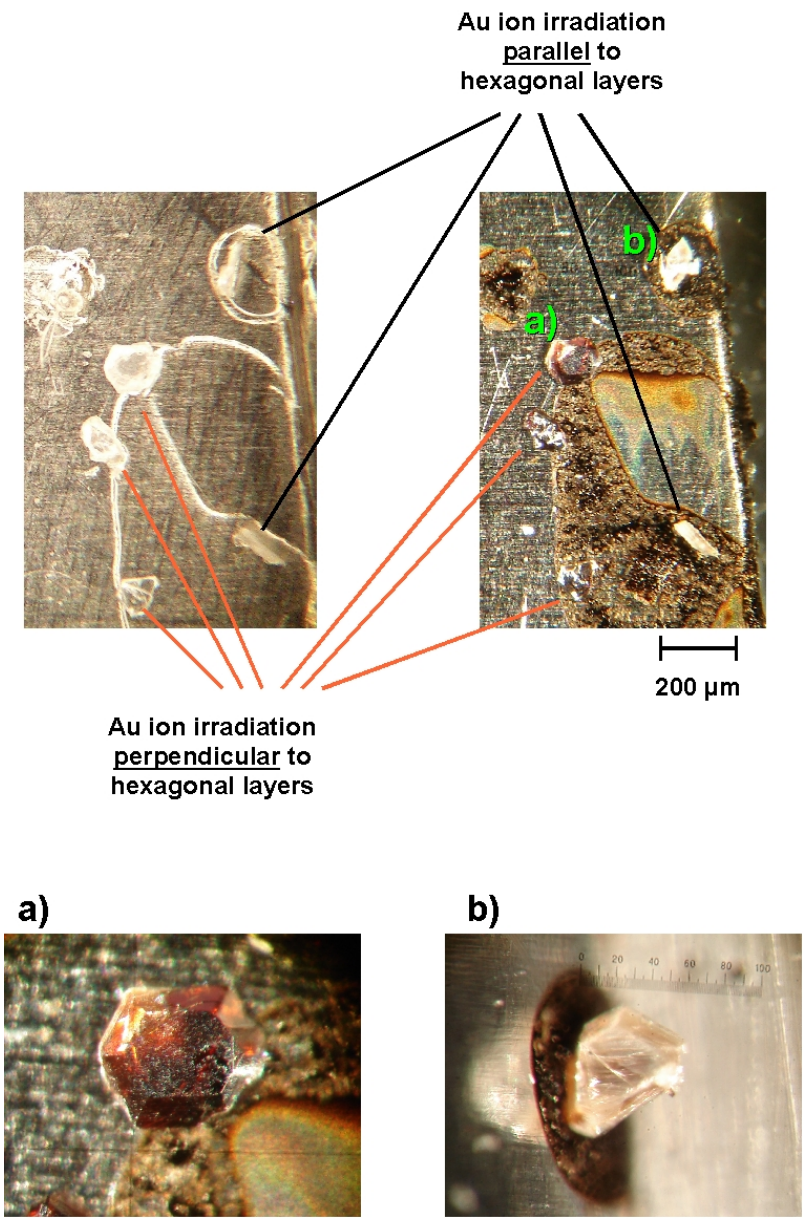

Figure 4.5: First orientation dependent irradiation with 11.1 MeV/u Au ions at 1 bar. Top left: Pristine hBN single crystals before irradiation. Top right: The same crystals, but irradiated with gold ions. Obvious coloring of the samples irradiated perpendicular to the hexagonal layers (a). Crystals with hexagonal layers oriented parallel to the ion beam (b) mostly withstand and retained grayish-white. Bottom: Close-up view of (a) and (b), in (b) the sample is being photograghed in a tilted position. All samples are glued to stainless steel with nail varnish.

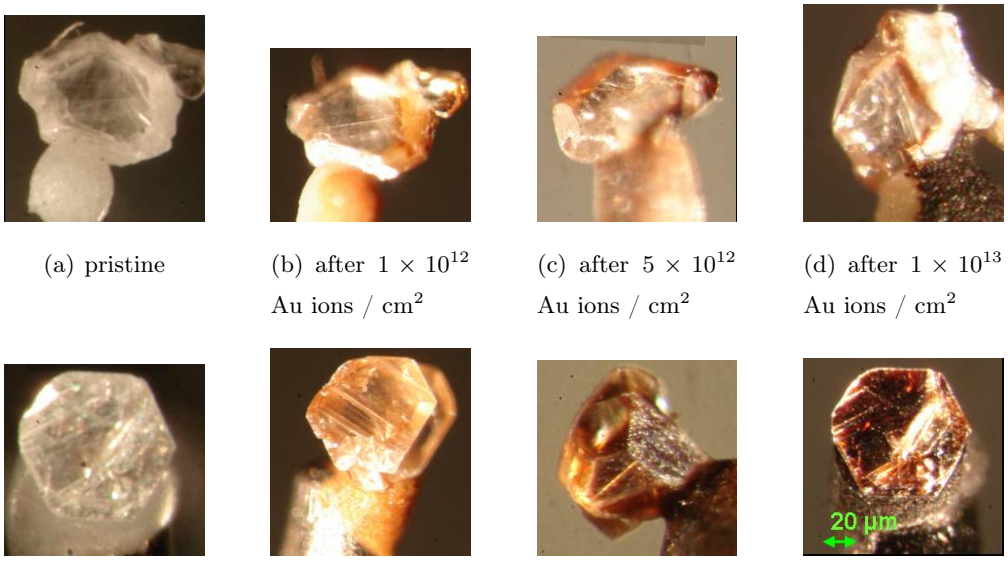

(a) pristine (b) after 1×10^{12} Au ions / cm^2 (c) after 5×10^{12} Au ions / cm^2 (d) after 1×10^{13} Au ions / cm^2

(e) pristine (f) after 1×10^{12} Au ions / cm^2 (g) after 5×10^{12} Au ions / cm^2 (h) after 1×10^{13} Au ions / cm^2

Figure 4.6: Fluence series of hBN single crystals irradiated parallel (a–d) to the hexagonal layers, and perpendicular (e–h) to the hexagonal layers.

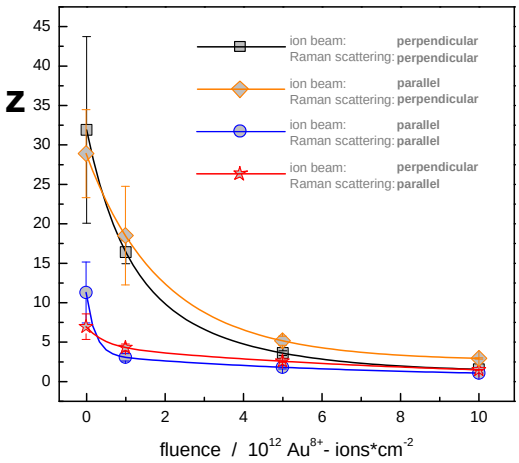

Figure 4.7: The ratio ($\zeta = E_{2g}$ Raman band maximum / Raman background) after several fluences of 11.1 MeV/u Au ion irradiations on hBN single crystals (Figure 4.6); taking two orientations into account (regarding irradiation and Raman scattering).

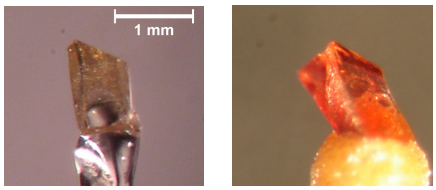

(a) (b)

Figure 4.8: cBN single crystal before (a) and after (b) irradiation with 5×10^{11} uranium ions per cm^2. $E_{ion} = 218\,^{MeV}/_{u}$.

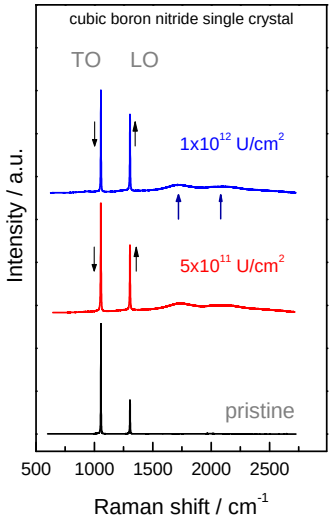

Figure 4.9: Raman spectra of cBN single crystal sample before irradiation (lower graph) and after a fluence of 5×10^{11}cm^{-2} (red) and 1×10^{12}cm^{-2} (blue). Ion bombardment equalizes the LO/TO intensity and induces two new Raman bands at 1712 cm^{-1} and 2080 cm^{-1}.

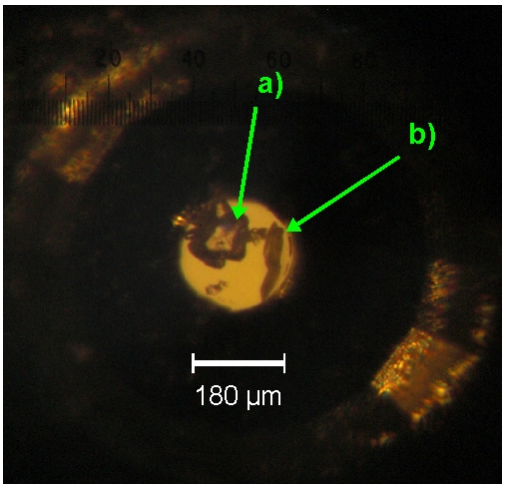

Figure 4.10: hBN crystals in a gasket hole - with the hexagonal layers oriented perpendicular (a), and parallel (b) with respect to the direction of ion beam propagation.

Table 4.1: Parameters of the orientation dependent irradiation experiment. Energy degrading at the Unilac irradiations habe been realised by aluminium foils.

P [GPa]		Ion	E_{ion} [MeV/u]	$l_{diamond}$ [mm]	$\frac{dE}{dx}$ [keV/nm]	fluence [ions/cm^2]
0	Unilac	Au	–	–	–	0
			11.1	–	15	1×10^{12}
			11.1	–	15	5×10^{12}
			11.1	–	15	1×10^{13}
4.3	SIS	Xe	–	–	–	0
			172	2.51	15	1×10^{11}
			185	2.64	15	3×10^{11}
			183	2.64	15	5×10^{11}
			141	1.71	15	1×10^{12}
8.7	SIS	Xe	–	–	–	0
			172	2.51	15	1×10^{11}
			185	2.64	15	2×10^{11}
			183	2.64	15	6×10^{11}
			173	2.51	15	1×10^{12}
			172	2.51	15	1.2×10^{12}

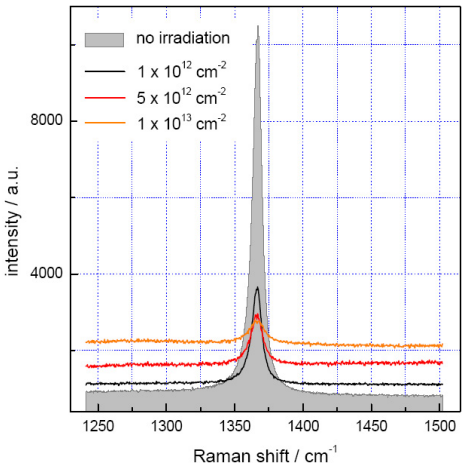

(a) 1 bar

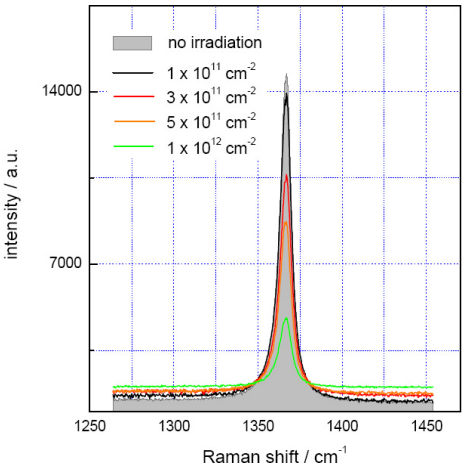

(b) 4.3 GPa

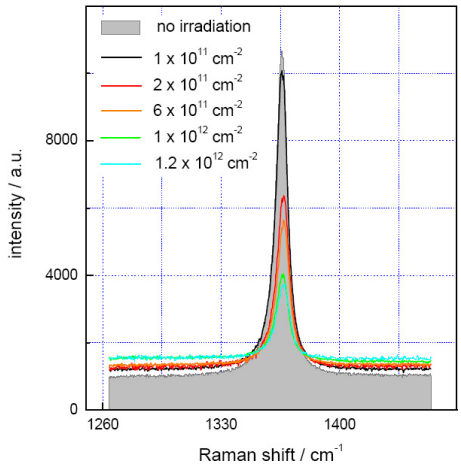

(c) 8.7 GPa

Figure 4.11: E_{2g}Raman band of hBN after different fluences and pressures. Irradiation as well as both incident and scattered Raman beam perpendicular to the hBN *c*-axis.

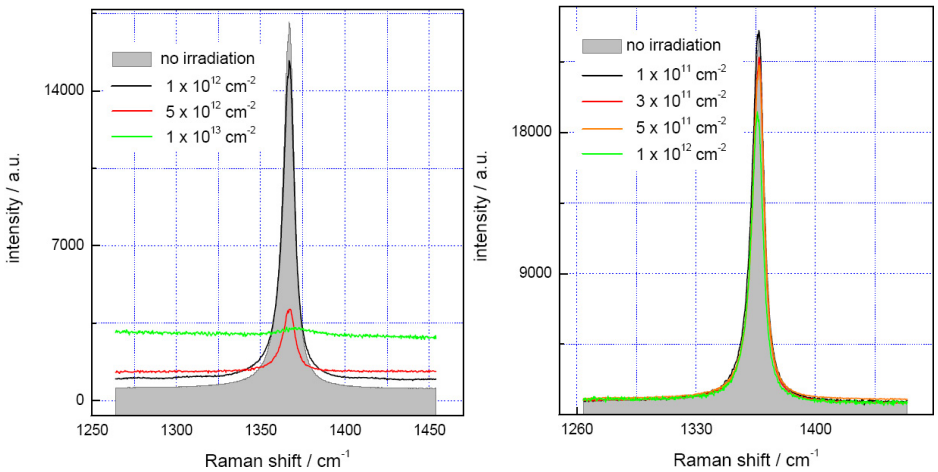

(a) 1 bar (b) 4.3 GPa

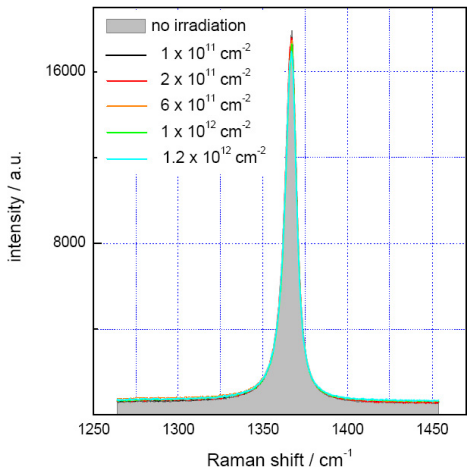

(c) 8.7 GPa

Figure 4.12: E_{2g}Raman band of hBN after different fluences and pressures. Irradiation as well as both incident and scattered Raman beam parallel to the hBN *c*-axis.

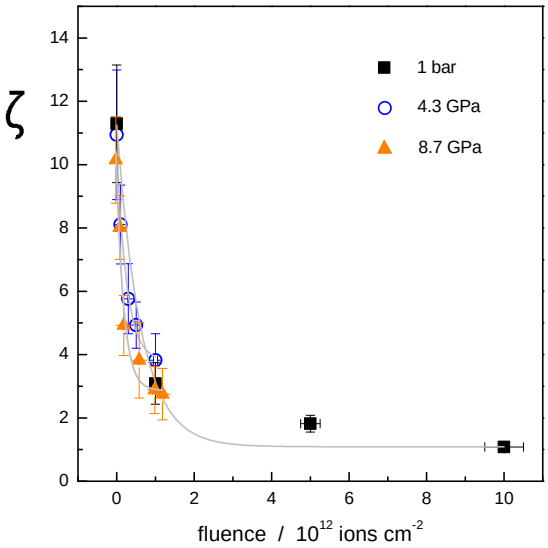

(a) Irradiation and Raman scattering ⊥ c

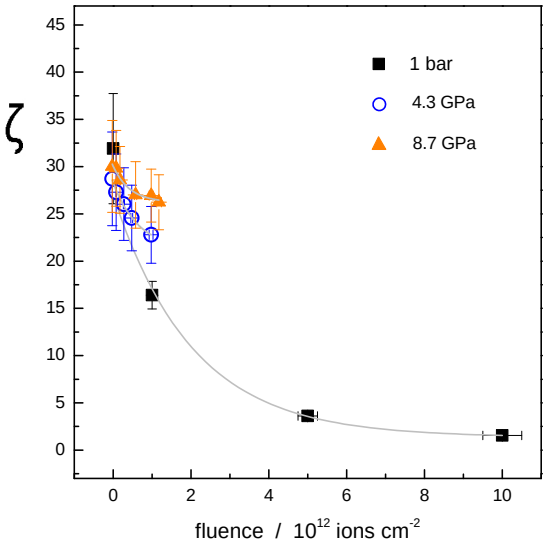

(b) Irradiation and Raman scattering ∥ c

Figure 4.13: ζ = Raman band maximum/Raman background after exposure to different fluences of gold (P = 1 bar) and xenon (P > 1 bar) ions. Irradiation and both Raman laser excitation and scattering was carried out perpendicular to c (a) as well as parallel to the c-axis (b) of the hexagonal BN layers. Unlike parallel irradiation and measurement, the perpendicular exposure shows a clear pressure dependency in terms of the behaviour of ζ.

4.3 Pressurization of BN, Irradiated Under Ambient Conditions

4.3.1 Cubic BN

As summarized in Table 4.2, three single crystal samples have been compared by means of irradiation conditions in order to obtain information about the Raman band shift, when pressurized. The first sample was not exposed to swift heavy ion irradiation, the second one was exposed to 1×10^{12} nickel ions per cm^2 at ambient conditions, and a third specimen was first pressurized to 16.49 GPa in a diamond anvil cell, then irradiated with 1.5×10^{12} uranium ions, and after some deactivation time released to 1 bar again. The pressure was somewhat less than before the irradiation. This might be due to a relaxation of the gasket. However, the Raman spectra of these three crystals are displayed in Figure 4.14, and the positions of the TO as well as the LO bands as a function of the pressure can be seen in Figure 4.15.

4.3.2 Hexagonal BN

Further subjects under study were the stability field of the hexagonal phase, and the question whether this field is constant when the crystal structure is affected by high energy deposition caused by swift heavy ions. Raman spectroscopy was applied for single crystal probing, and powder samples have been investigated using synchrotron X-ray radiation in order to observe the transformation from hexagonal to wurtzitic BN directly.

Raman spectroscopy

For Raman spectroscopic measurements, we irradiated several hBN single crystals in vacuum and room temperature at the Unilac of GSI, using different fluences of xenon ions as summarized in Table 4.3. All samples were arranged with the hexagonal layers perpendicular to the beam as has been proved to be the most effective orientation with respect to crystal alterations (Figures 4.5 and 4.6). After the samples as well as the sample holders had recovered

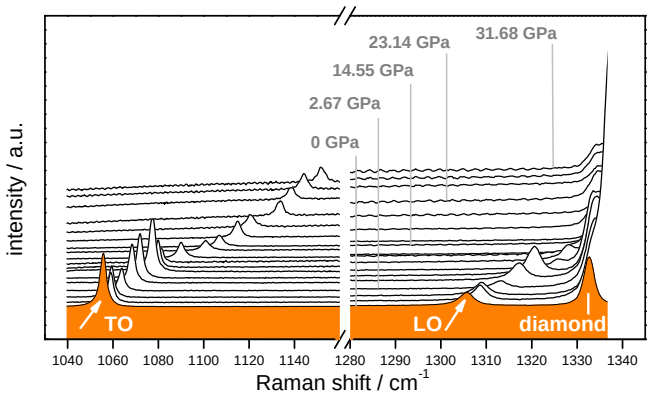

(a) Pristine sample - no irradiation.

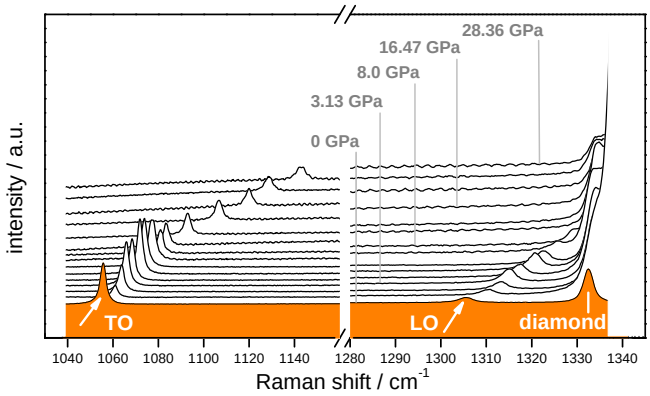

(b) *Ex-situ* irradiation with $1{\times}10^{12}$ Ni ions per cm^2

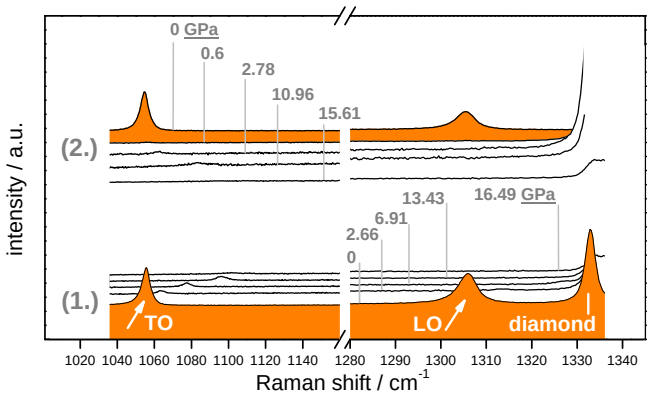

(c) (1.) pristine cBN at increasing pressure. (2.) The same sample after *in-situ* irradiation with $1.5{\times}10^{12}$ U ions per cm^2 at 16 GPa and decreasing pressure.

Figure 4.14: Raman spectra of cBN single crystal samples at different conditions.

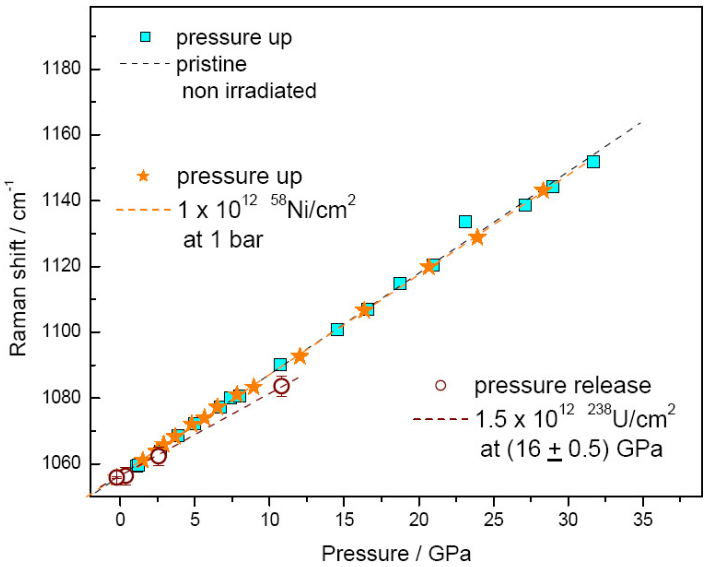

(a) TO Raman band position

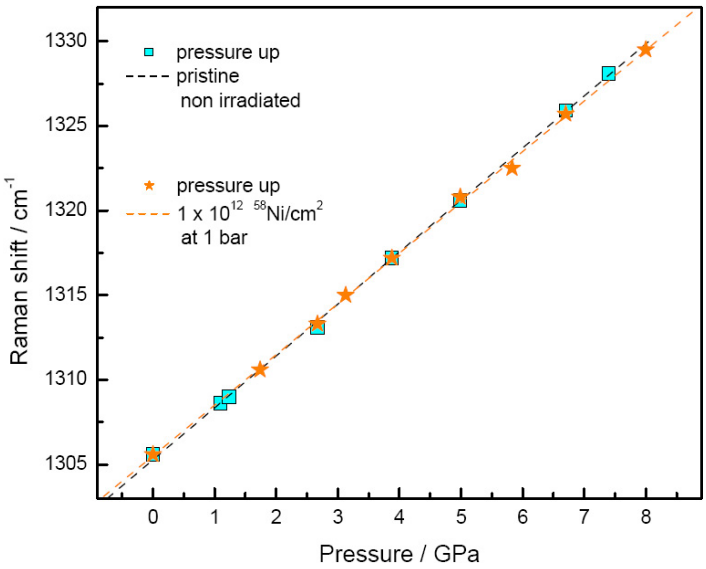

(b) LO Raman band position

Figure 4.15: cBN Raman bands as a function of pressure. Different irradiation conditions are indicated.

Table 4.2: Parameters of the cBN single crystal irradiation.

	fluence [cm^{-2}]	ion	$\frac{dE}{dx}$ [$\frac{keV}{nm}$]	$\frac{\Delta\omega}{\Delta P}$ [$\frac{1}{GPa \cdot cm}$]	
				TO	LO
no irradiation	–	–	–	3.08 ± 0.04	3.07 ± 0.03
ex-situ irradiated at 1 bar	1×10^{12}	nickel	18 ± 1.8	3.06 ± 0.02	3.00 ± 0.04
in-situ irradiated at 16 GPa	1.5×10^{12}	uranium	24 ± 2.4	2.52 ± 0.27	–

from the irradiation and were safe for transportion and handling, four crystals were put into a sample chamber of a stainless steel gasket, together with a methanol-ethanol-water pressure transmitting medium and a small ruby chip for pressure gauging. Starting off with 6.17 GPa, the E_{2g} Raman vibration has been monitored until its disappearance at higher pressures, which is displayed in Figure 4.17 and subsumed in Figure 4.18. Obviously, irradiation with heavy ions does not only result in an evidently decreased maximal pressure for hBN detection, but also in a sharper area of transformation as seen in Figure 4.17 (d). The time, necessary for accumulating the Raman scattered light, has been adjusted to a signal that is the weaker the more the sample was exposed to irradiation (Figure 4.1 (a)).

Table 4.3: Parameters of the irradiation experiment on hBN single crystals, aiming at information about the phase stability field. Irradiations took place at the Unilac of GSI. $P(max)_{hBN}$ is the highest pressure, at which traces of hBN were detected.

fluence (ions/cm^{-2})	ion	E_{ion} [MeV/u]	$\frac{dE}{dx}$ [keV/nm]	$P(max)_{hBN}$ [GPa]
–	–	–	–	11.89
5×10^{11}	Xe	11.1	14.3 ± 1.4	11.71
1×10^{12}	Xe	11.1	14.3 ± 1.4	11.53
1×10^{13}	Xe	11.1	14.3 ± 1.4	10.76

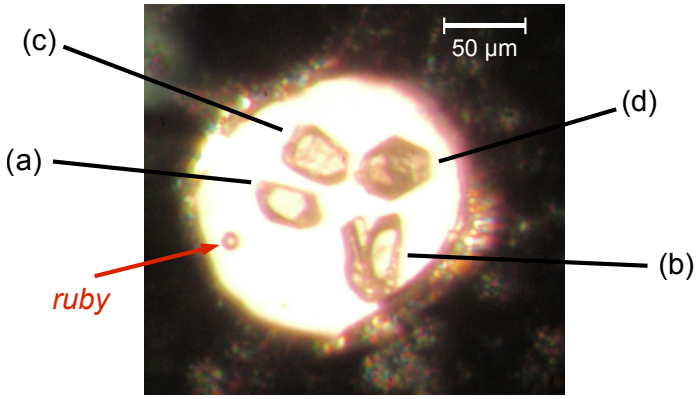

Figure 4.16: View into the sample chamber, containing four hBN single crystals and a ruby pressure marker. The crystals were exposed to different fluences of 11.1 MeV/u Xe^+ ions per cm^2: (a) no irradiation; (b) 5×10^{11}; (c) 1×10^{12}; (d) 1×10^{13}.

X-ray diffraction

Powder hBN samples were irradiated with gold ions at room temperature and without applied pressure. Gasket material was rhenium, pressure transmitting medium was a methanol-ethanol mixture (4:1), and a small ruby chip served for pressure measurements. After each pressure increase the material was kept under these conditions for at least one hour in order to stabilize the lattice structure. Each diffractogram was measured in a full 360° mode. The investigation of the non-irradiated sample and the material with exposure to 1×10^{12} ions per cm^2 was conducted at the European Synchrotron Radiation Facility (ESRF). The sample irradiated with 5×10^{11} ions per cm^2 was investigated at the Advanced Photon Source (APS) of Argonne National Laboratory. The integrated diffraction patterns are summarized in Figure 4.19.

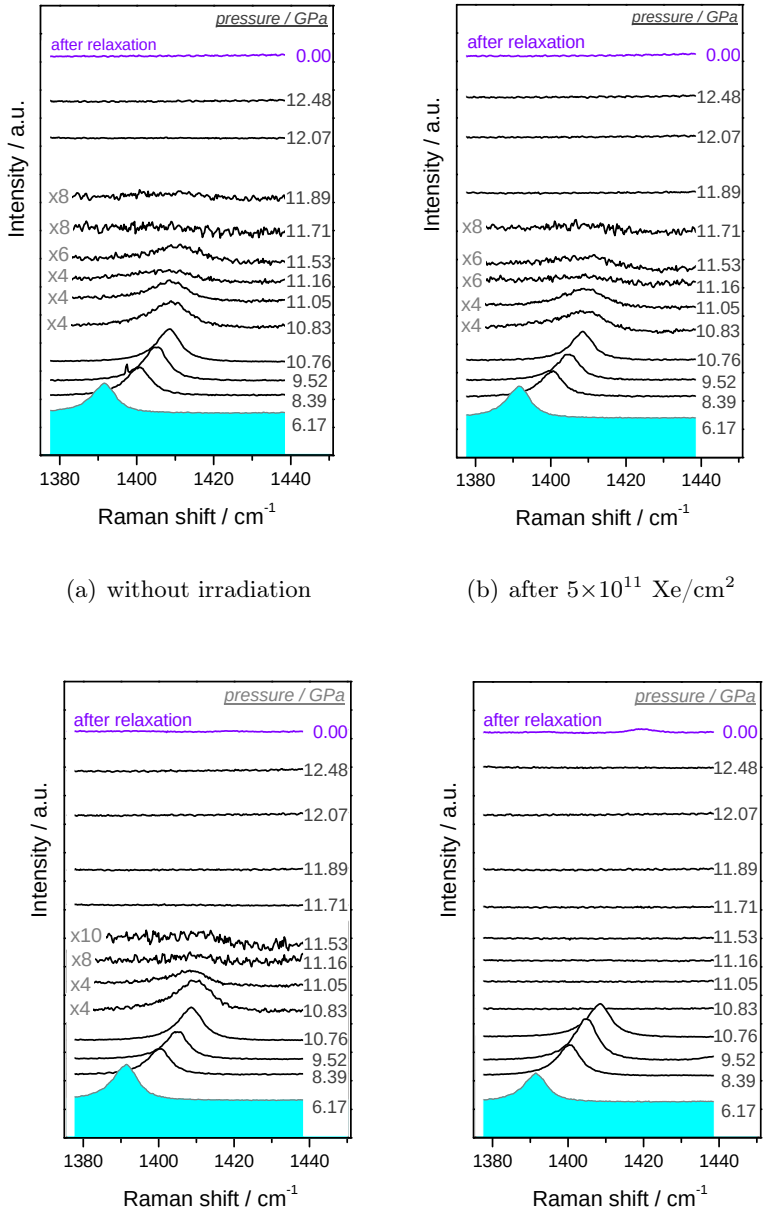

(a) without irradiation

(b) after 5×10^{11} Xe/cm^2

(c) after 1×10^{12} Xe/cm^2

(d) after 1×10^{13} Xe/cm^2

Figure 4.17: E_{2g} Raman band of hBN single crystal samples, seen in Figure 4.16 at different pressures. The disappearance of this vibrational mode occurs at lower pressures when irradiated with gold ions prior to compression. At highest fluences (d), the Raman band loss takes place significantly more abruptly.

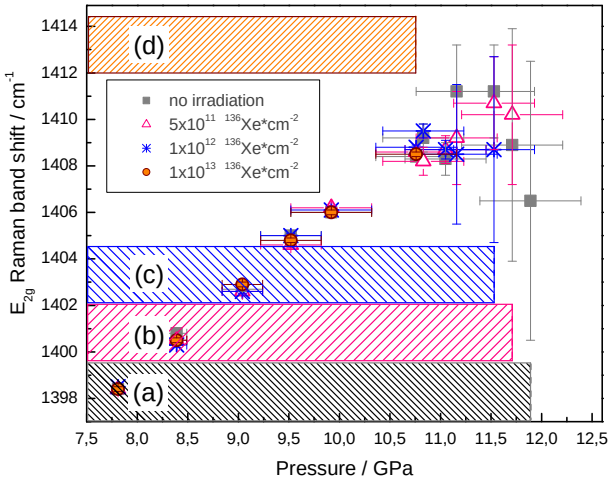

Figure 4.18: Positions of the E_{2g} Raman bands of hBN crystals, exposed to different fluences of gold ions. The hatched areas mark the pressure range with detectable hBN traces. At higher compressions no signs of the primary phase were measurable. Obviously, the highest pressure of hBN detection and the exposed irradiation dose are related with each other. (a) no irradiation, (b) 5×10^{11} Au/cm^2, (c) 1×10^{12} Au/cm^2, (d) 1×10^{13} Au/cm^2. This figure summarizes the findings of Figure 4.17.

Table 4.4: Samples for the *in-situ* XRD measurements. Each sample was embedded in rhenium gaskets. Pressure transmitting medium: methanol:ethanol (4:1).

material	fluence [Au^+/cm^2]	ion	irradiation-facility	XRD
hBN	–	–	–	ESRF
hBN	5×10^{11}	Au	Unilac	APS
hBN	1×10^{12}	Au	Unilac	ESRF

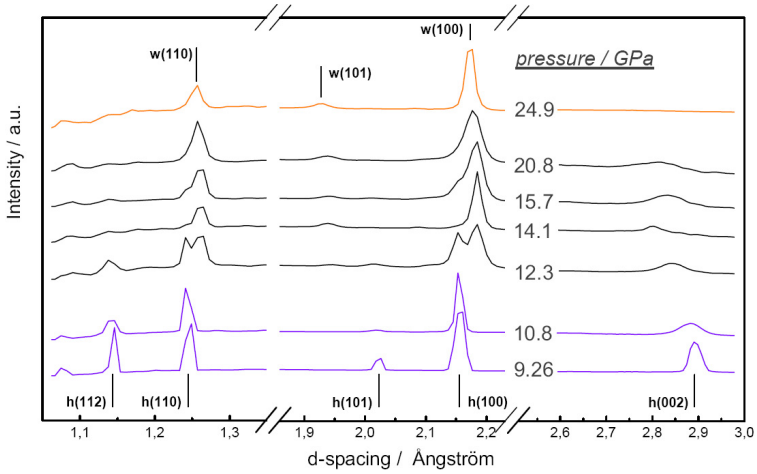

(a) no irradiation

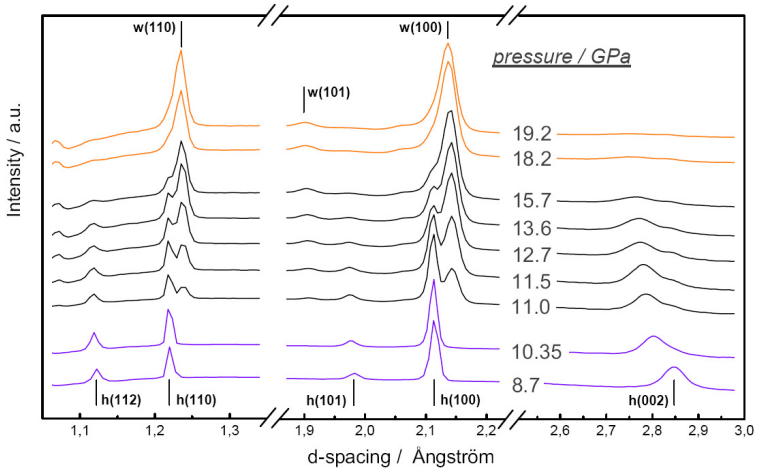

(b) *Ex-situ* irradiation with $5{\times}10^{11}$ Au ions per cm^2

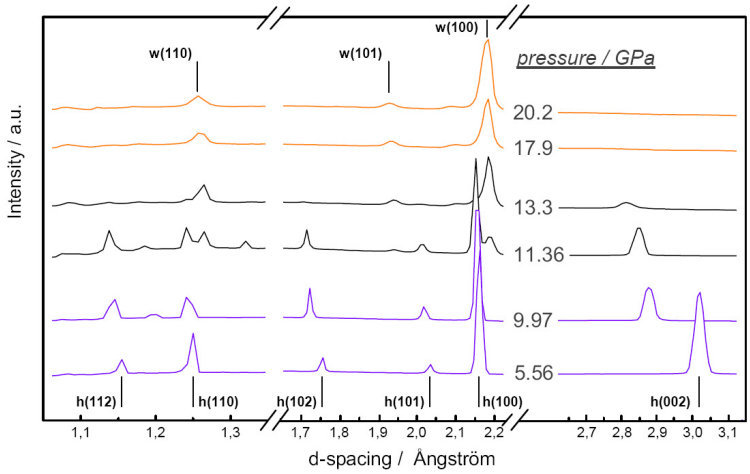

(c) *Ex-situ* irradiation with $1{\times}10^{12}$ Au ions per cm^2

Figure 4.19: Synchrotron X-ray diffraction: Pure hexagonal BN (purple curves), pure wurtzitic BN (orange curves), and BN samples with both hexagonal and wurtzitic traces (black curves). The samples (b) and (c) were irradiated *ex-situ* with different fluences.

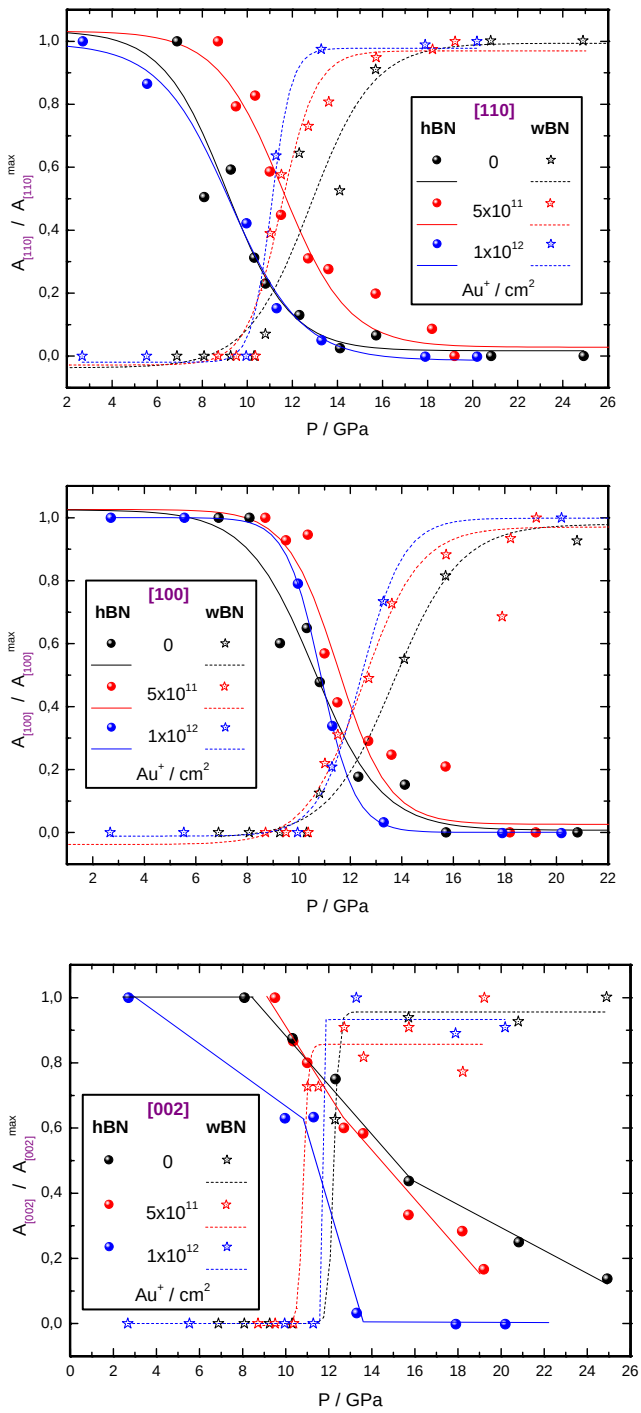

Figure 4.20: Intensities of the hBN and wBN reflections in comparison, integrated and normalized to the maximal value, as a function of pressure. Upper graph: [110], medium graph: [100], lower graph: [002]. This illustrates the pressure phase transition for three samples, pristine and irradiated with Au^+ ions of two different fluences.

5 Discussion

The very first idea to irradiate boron nitride was the query, whether traversing ions can trigger phase transitions if the pressure of a hBN sample is adjusted in such a way, that the material is near the transformation boundary to wBN (see Figure 2.2). Shock waves can propagate along the ion track according to the Coulomb explosion model [30], and therefore an additional pressure effect is supposed to occure. Due to the irreversibility of the hBN-wBN transformation, the wurtzitic structure thus should be detectable even when the pressure is released and the sample has returned into the stability field of its hexagonal phase. The temperature increase on the other hand, which is described by the thermal spike model [26, 132], may then bring the thermodynamic conditions of the sample towards higher thermal energies. Hence, simultaneous pressure and temperature effects of traversing charged particles give rise to aim for an ambigious goal: the fabrication of cubic boron nitride[1].

However, this aim could not be realised. Even wBN powder samples, irradiated at 21 GPa did not show any trace of cBN using *ex-situ* Raman spectroscopic measurements, which were carried out after a deactivation time of two months. Moreover, the wurtzitic phase could not have been desolved by *ex-situ* Raman spectroscopy either. Nevertheless, powder XRD clearly revealed the transformation from hBN into wBN and documented the quenching of the latter structure after sole pressurization. Figure 5.1 compares X-ray diffractograms of plain, non-irradiated hBN powder with those samples that were either only pressurized to 21.1 GPa or both irradiated with a high fluence of heavy ions (4.5×10^{11} Pb^{+}/cm^{2}) and pressurized to 21.0 GPa simultaneously. Obvious changes occured taking into account the single peak intensities, which entailed further

[1] A successful experiment would have raised hopes for the transformation of graphite into diamond induced by swift heavy ions on samples under pressure.

investigations concerning samples exposed to swift heavy ion irradiation and high pressure at the same time.

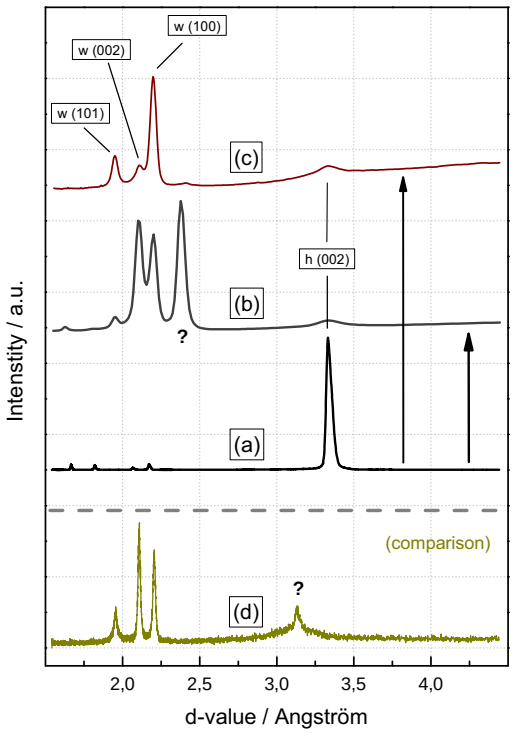

Figure 5.1: X-ray diffraction on pristine hBN powder (a), which as well serves as the starting material for a sole pressurization up to 21.1 GPa (b), and an irradiation with 4.5×10^{11} Pb ions at 21.0 GPa (c). For reasons of comparison: chemically generated wBN (Dubrovinskaia *et al.* [25]. The polymorph reflexion in (b) has disappeared almost entirely.

5.1 Radiation Stability examined by XRD

Besides ion-beam induced crystalline to crystalline phase transformations in insulators [6, 7, 9, 131] and metals [21], intense exposure to this kind of ionizing radiation can amorphize initially crystalline samples [68, 74]. In analogy to metallic phases, which are commonly believed to be nearly insensitive to electronic energy loss, compounds with strong ionic binding and directed orientation of the interatomic bonds also tend to withstand high S_e [81]. Very mobile charge

carriers thus prevent the absorbed energy to be transferred from the electron subsystem to the atomic lattice, and therefore no fulminant melting within the wake of the ion can occur. Moreover, temperature influence plays a crucial role by means of melting the material. Since our irradiations took place at room temperature, no elevated degree of amorphization could be expected and, as depicted in Figures 4.2, 4.3 and 4.4, no amorphization was detected via X-ray diffraction, since no significant broadening and no decreasing of the reflections in the diffraction patterns emerged.

On the other hand, due to the ionic and covalent character of the BN-bonds, ion beam-induced amorphization could not be excluded entirely. Hexagonal BN in particular, which possesses very weak interlayer attraction, has been proven to be prone to amorphization under the application of mechanical forces [49], resulting in deformation, shearing along the basal planes, and twinning in the crystal. Nevertheless, noticeable mechanical stress is not supposed to be introduced into the hBN lattice via ion beam transit. Cubic as well as wurtzitic BN are, due to their outstanding hardness (Table 2.3), less susceptible to mechanical influences.

Graphite whose crystal structure is similar to that of hBN, nevertheless amorphized under ion bombardment, but only after exposure to fluences higher than 1×10^{13} ions per cm^2 [86] and in the regime of nuclear stopping using He ions, which are essentially lighter than the projectiles utilized in this work. Niwase [86] therefore proposed a model in order to describe the amorphization process in basal planes as a function of ion fluence, which results in emanated lattice defects:

Lattice defects Irradiation-induced defects are classified into three types of interstitial defects (single- and double-interstitials, interstitial loops) as well as three types of vacancy defects (single vacancies, collapsed lines and vacancy loops). The h-regions are areas of structures with hexagonal shape, whereas d-regions are characterized by disorder.

Amorphization process Due to a relatively high activation energy for vacancy hopping from one layer to its neighbouring one, such a defect is capable only

to move intralayer-wise, wheras interstitial atoms are forced to settle between the basal planes. However, has the energy loss of the impinging ion once caused the displacement of a B or N atom off its site, it is supposed to form a double-interstitial with an atom of the different species. The single-vacancy concentration, which is thus twice the number of the double-interstitial concentration [86], reaches a quasi-steady state at a certain fluence. In graphite, the hexagons begin to collapse when a significant amount of double-vacancies has emerged. The h-regions will then transform to d-regions, and the entire system eventually amorphizes. Although this process is described for graphite, it is likely to occur in hBN in a similar fashion (see Figure 5.2).

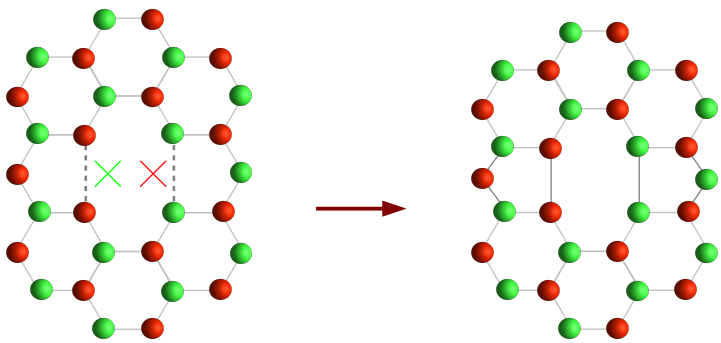

Figure 5.2: Proposed structure of the collapsed line induced by a double-vacancy in hBN. Due to repulsive interaction between energetic ions and nuclei of the basal planes

Our measurements clearly showed consistent results, which can be described by the above mentioned processes. On the one hand, XRD-patterns of irradiated BN powder samples do not give rise to significant amorphization in all three allotropes up to fluences of 1×10^{13} Ni ions per cm^2 (Figures 4.2, 4.3 and 4.4). The decreased Raman band intensities (Figure 4.1) can be interpreted as the accumulation of vacancies within the lattice under irradiation with up to 1.5×10^{13} Pb ions per cm^2, restraining the E_{2g} vibrations in hBN. The increased background is as well attributed to the generation of defects, which can become visible in colour centers (F-centers).

5.2 Ion-induced Colour Change

Ion irradiation apparently causes coloration of hBN (Figures 4.5 and 4.6) as well as cBN crystals (Figure 4.8).

For cubic BN, Nistor *et al.* [85] discovered several new, radiation-induced, isotropic paramagnetic centers via high-frequency electron spin resonance. UV irradiation of both p- and n-type cBN yields centers involving "very likely" protons. Irradiation of n-type cBN on the other hand with 1 MeV electrons results in the formation of vacancy associated paramagnetic defects and quasi-free electrons in colloidal particles. Protons of 2 MeV have been used by Manfredotti *et al.* [71] in order to investigate the irradiation hardness of luminescence peaks. In cBN it was found that ion beam-induced luminescence is dominated by three bands, one at approximately 2 eV, and the other two at higher energies. These three bands seem to be relatively radiation-hard and to be related to defects induced by doping. It is worth mentioning that we attempted to collect iono-luminescence signals using an ellipsoidal mirror and light amplifiers, focussing on a cBN single crystal when irradiated with carbon ions. Unfortunately, no signal could be detected. Shishonok and Steeds [107] irradiated cBN with electrons and discovered interstitial-related optical centres. It is thus very likely to induce color centers due to vacancies in the cBN lattice, caused by swift heavy ion irradiation, accompanied by decreased L_O and T_O Raman band intensities and simultaneously increasing luminescence backgroung (Figure 4.9).

Hexagonal BN however, is capable to develop color centers in nitrogen vacancies [58], where electrons of the boron shells can remain due to its partly ionic character. The fact that hBN irradiation yields a strong orientation dependent colouring effect (Figures 4.5 and 4.6) is suggested to result from the anisotropic electron density [16]. As known from (2.13), the energy of a traversing charged particle is transferred to the actual atomic lattice of the crystal via electron-phonon coupling according to the thermal spike model.

An ion, hitting the hexagonal layer parallel to c, suffers a larger electronic energy loss because of a higher "effective electron density" than an ion, which traverses the crystal perpendicula to c, i.e. parallel to the hexagonal layers, where the electron density is inhomogeneously distributed, ranging from its

maximum along the hexagonal planes and its minimum in between two layers.

The well known channeling effect [92, 100, 101, 118] can be used to describe the observed orientation dependent colouring effect. An ion, entering the hBN crystal perpendicular to c, is forced in between two neighbouring layers due to their repulsive charges (Figure 5.3). Hence, it is unlikely to transfer energy from the energetic ion to the lattice, preventing it from F-center generation. Otherwise, defects, leading to an increased Raman luminescence background, accompanied by a depressed E_{2g} band intensity (Figure 4.7) must have been produced. In summary it can be suggested, that irradiation along the hexagonal layers most likely induces only one-boron centers (Figure 5.9), which are not known to be colour centers. On the other hand, irradiation parallel to the hBN c-axis may generate both one-boron centers as well as three-boron centers. The latter is proved to be a colour-center [58] and therefore most likely the reason for the obvious color change.

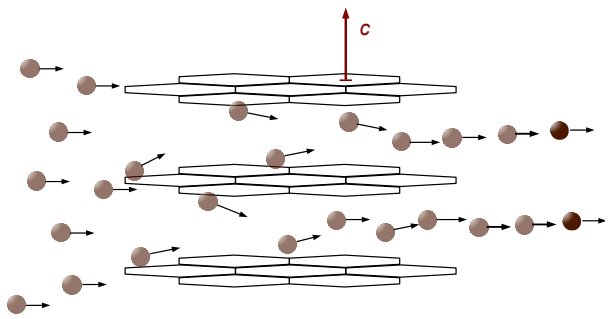

Figure 5.3: Principle of the channeling process in hBN. The impinging ions are constrained to move in between the hexagonal layers, reducing their ability to transfer kinetic energy to the lattice.

Vacancy creation is essential for the forming of colour centres, and therefore needs to imply good electron phonon coupling. Atomic displacement, directly transferred by nuclear collision is negligible due to the very little cross section for such a process and the fact, that the ion transit is in the electronic energy loss regime (Figure 2.4 (a)).

In general, the exposure of BN to ion irradiation introduces several changes within the volume of the material determined primarily by the penetration depth of the impinging ions. Such effects are local densification, compressive stress or

production of point defects. The production of such point defects in hBN and cBN has been studied theoretically, using for example the density functional theory [69, 89, 105]. Orellana and Chacham [89] found that the self-interstitials N_i and B_i in hBN have lower formation energies than those of the vacancies V_B and V_N.

5.3 Irradiations under Different Pressures and Orientations

Raman spectroscopic measurements, depicted in Figures 4.11 and 4.12, and summarized in Figure 4.13, clearly reveal orientation and pressure dependent processes, triggered by heavy ion irradiation. As under exposure to energetic Xe^+ ions at vacuum conditions, experiments at elevated pressures showed similar tendencies by means of equalization of the E_{2g} Raman band intensity and the luminescence background. Differences only emerge, when ions traverse the hBN crystal parallel to the c-axis. Here, the above mentioned equalization seems to be the more detained the higher the pressure.

The development of the luminescence background as well as the decreasing E_{2g} intensities for the three pressures are plotted seperately in Figure 5.4 up to the fluence of 1.2 $^{\text{ions}}/_{\text{cm}^2}$. As predicted, irradiation leads to tendentiously decreasing Raman band intensities, accompanied by increasing luminescence background. However, the crystals, exposed to the heavy ion beam perpendicular to their c-axes react more distinctly. E.g., after exposure to 1.2 $^{\text{Xe}^+}/_{\text{cm}^2}$, the area of the E_{2g} band has drop to 26 % of the value measured on the pristine sample, when irradiated $\perp$ c at 8.7 GPa. The same fluence and pressure, but irradiated $\parallel$ c, causes a Raman band intensity of 91 % of the value of the virgin crystal.

Obviously, ions interact with the basal planes in a strong orientation dependent manner, leading to the generation of F-centers only when moving along c. However, when pressure is applied to a solid state body, atoms are pushed together, which increases the charge density between them. The accompanying reduced electron-nucleus distance again increases the electron-electron repulsion and induces orbital overlap and hybridisation. Eventually pressure leads

to closing of band gaps, converting the material more and more into a metal. Pressurization therefore strengthens chemical bonds and cohesive properties of cBN [141,145], which possesses similar σ-bonds as hBN within its hexagons. On this note, pressurization should detain the hBN structure from being damaged by heavy ion irradiation. The behaviour of the hBN crystals, oriented to the incident beam parallel to c is thus consistent with this suggestion.

On the other hand, the uniform reaction of the hBN samples with the c-axis oriented perpendicular to the ion beam, regardless of the pressure, implies a different defect accumulation process. The strongly non-isotropic compressibility of hBN is well known [116, 117]. At a pressure of 4.3 GPa the unit cell dimension are $c/c_0 = 0.91$ and $a/a_0 = 0.995$. Furthermore, a pressure of 8.7 GPa means $c/c_0 = 0.87$ and $a/a_0 = 0.99$. Considering the above mentioned channeling effect, an appreciable contraction of the inter-layer distance in hBN must reduce the possibility of the impinging ion to traverse the crystal in between two layers without contacting them. Thus, pressure increases the cross-section for ion-target interactions when irradiated perpendicular to c. In contrast to the irradiation along the c-axis, at which the effective density remains nearly constant.

5.4 The hBN → wBN Phase Transformation

In-situ powder XRD measurements clearly show pure hBN up to (10.2±0.2) GPa in all samples, regardless if they were exposed to swift heavy ion irradiation or not. These findings are in good agreement with the pioneering work of Corrigan & Bundy [19]. Though Raman spectroscopy on single crystals, however, can not resolve the wurtzitic phase, the E_{2g} Raman band of hBN could be detected with almost constant intensities up to (10.87 ± 0.05) GPa. Again, regardless of the irradiation fluence. Nevertheless, the deviating E_{2g} intensity curve can be explained by the incipient transition into the wurtzitic phase in this pressure regime, which reduces the single crystal hBN sample to wBN powder. In accordance with our *in-situ* XRD data, the phase transition into wBN is a lingering process.

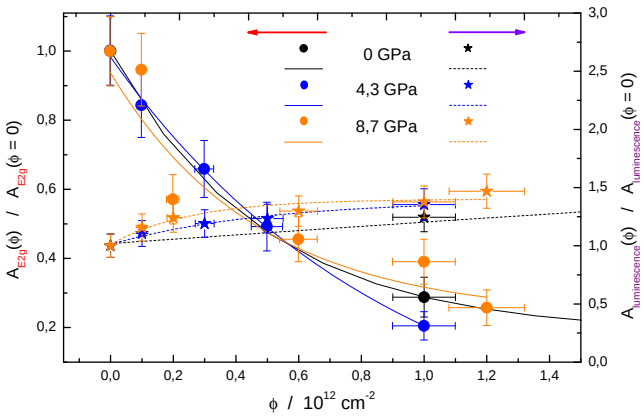

(a) irradiated perpendicular to the hBN c-axes

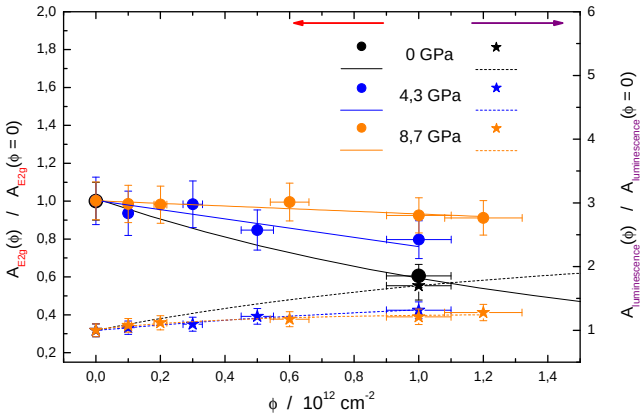

(b) irradiated parallel to the hBN c-axes

Figure 5.4: Developments of the normalized E_{2g} Raman band intensity (left axis of ordinate) and the luminescence backgroung (right axis of ordinate) of the orientation dependent hBN crystals, and as a function of ion fluences. These values are seperated from the ratio ζ of Figure 4.13.

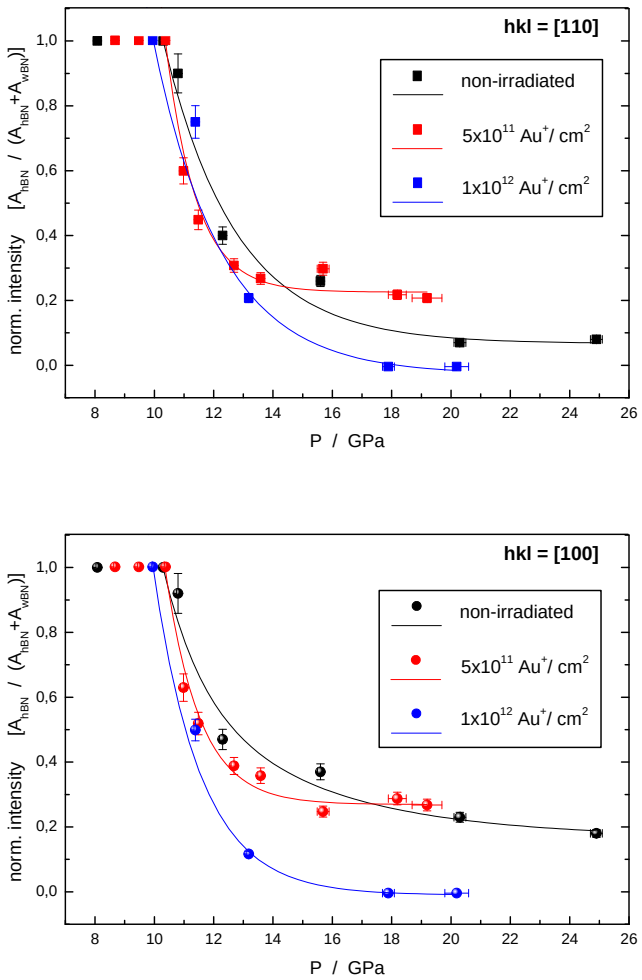

Figure 5.5: Proportions of the hBN phase in comparison to the wBN fraction as a function of pressure, and for powder samples, non-irradiated as well as exposed to two different fluences of Au^+ ions. Based on the normalized intensities of the hBN and wBN [110] reflections (upper graph), and [100] reflections (lower graph).

5.4.1 X-ray diffraction

Prior irradiation with energetic Au^+ ions (11.1 MeV/u) causes a more abrupt transformation as the development of the [100] and [110] reflections points out. Figure 5.5 compares intensities of the hexagonal [100] and [110] reflections with those of the wBN phase as a function of pressure. The diagram can be distinguished in three pressure regimes: The first regime is characterized by constant value of 1 of the ratio between the intensities of the hexagonal lattice reflections and those of the sum of both the hBN and wBN peaks together. This indicates no transformation to wBN and a pure hBN phase.

The second pressure regime begins around a pressure of (10.2 ± 0.2) GPa, indicated by the emergence of wBN reflections. The hexagonal lattice begins to alter its structure. The pressure at this point overcomes the repulsive force between the stacked B and N atoms of adjecent layers, and the weak interlayer π-bondings, which exhibit significant ionic charecteristics are on the verge of changing into covalent sp^3 hybridizations. The initiation of the hBN → wBN phase transformation is not affected by ion irradiation on the samples before pressurization. The declining slope between 10.2 GPa and 12.5 GPa in the $I_{hBN}/(I_{hBN}+I_{wBN})$ vs. pressure diagram is also irradiation independent and goes over in a lower, but still exponentially declining curve, which marks the third and highest pressure regime.

Nevertheless, at a pressure of (17.9 ± 0.1) GPa, the sample exposed to the highest fluence of 1×10^{12} ions per cm^2 has converted to wBN entirely, whereas both the powder suffering from bombardment with 5×10^{11} ions per cm^2 and the pristine sample still possess fractions of hBN, indicated by the remaining h(100) and h(110) reflections up to $P = (24.9 \pm 1.0)$ GPa.

Meng *et al.* [75] investigated the formation of sp^3 bonding during the hBN → wBN phase transition on powder samples, using inelastic X-ray scattering and near K-edge spectroscopy. The results are in good agreements with our findings. Furthermore, Meng *et al.* observed a strong orientation dependence of the emergence of the σ and π components, representing hBN and wBN, respectivelly. This behaviour is explained by the geometric properties of the hBN crystals, which are flat grains with the tendency to align preferentially with

their c-axis along the direction of the applied pressure (Figure 5.8). Therefore, these crystals transform into wBN at the lowest forces, applied to the diamond anvils.

Hence, the remaining [002] reflection (lower graph in Figure 4.20) of the pristine sample and the of the powder, which was exposed to 5×10^{11} ions/cm^2, up to a pressure of (24.9 ± 0.5) GPa is due to the non-isotropic pressure within the sample chamber, and the higher pressure along the anvil axis (see Figure 5.8). The hexagonal crystals therefore tend to allign their c-axis perpendicular to the anvil surface. Only the few crystals, which remain somehow with c parallel to the surface of the diamond anvils, are those crystals, which transform to wurtzitic BN at last, when overall pressure is rising.

In order to understand the possible role of irradiation on the hBN $\rightarrow$ wBN phase transition, it is worthwhile to recapitulate the transformation process considering the generation of defects, induced by decelerated charged particles in matter.

As described elsewhere [57, 89], nitrogen interstitials (N_i) are the most stable defects in hBN. Being arranged between adjacent layers, these interstitials can induce buckling (Figure 5.6) of the basal planes [79]. Though Mosuang & Lowther investigated the hBN to cBN phase transition[2], their findings are suitable for the understanding of the mechanism behind the transition into wBN. As described in the theory chapter of this work, the transformation of hBN into wBN implies the approach of B and N atoms of adjacent layers, which requires buckling of the hexagons in the plane [75,130]. Hence, irradiation is suggested to ease the conversion of the interlayer π bonds, which is partial ionic into stronger and predominantly covalent σ bonds, necessary for the forming of sp^3 orbitals in wBN.

5.4.2 Raman spectroscopy

Raman spectroscopic measurements do not differ considerably from XRD results. Unlike the XRD measurements, where powder samples were investigated,

[2] Mosuang & Lowther also proposed ion bombardment to serve as a catalyst in the hBN $\rightarrow$ cBN phase transition [79].

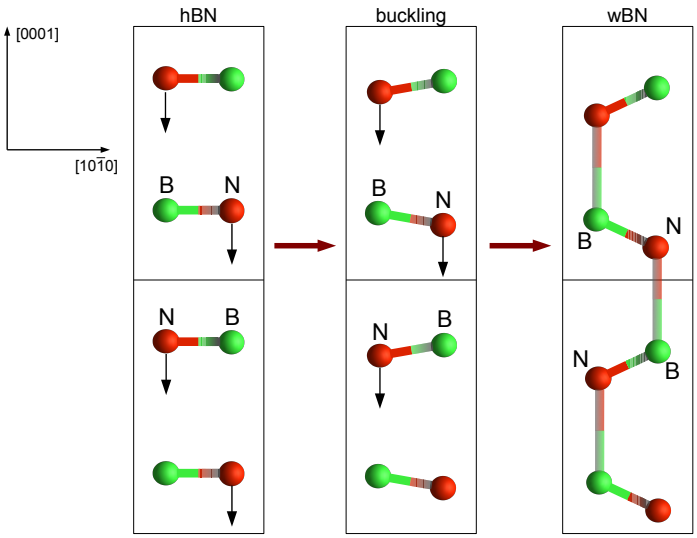

Figure 5.6: Top view along [11$\bar{2}$0] in the crystal structures of hBN (left) and wBN (right). Buckling (middle) can be induced by interstititials [75,130], and therefore ion irradiation prior pressurization can make the pressure driven hBN → wBN phase transition more abrupt.

Raman spectroscopic probing was applied on single crystals (Figure 4.16), which were all oriented with its c-axis parallel to the diamond axis along the direction of the highest pressure gradient. Thus, all crystals were exposed to the same conditions. Nevertheless, as seen in Figure 5.7, a trend towards lower pressure in terms of the accomplishment of the phase transition into wBN is observable.

The Raman spectra, where the integral E_{2g} band intensity, normalized to the first measurement at (6.71 ± 0.05) GPa, is plotted as a function of pressure, can be divided in two regimes. The first one comprehends data points, recorded at $P \leq 10.2$ GPa, and the second one at $P \geq 10.78$ GPa. Data points of the first regime do not reveal significant differences by means of irradiation fluences, but the well-defined transition from the lower-pressure to the higher-pressure regime is again the more abrupt the higher the fluence of Xe^+ ions, which was applied to the crystals prior pressurization. In the second pressure regime, the unirradiated sample showed a tendency to the highest, normalized intensities; followed by the crystal, irradiated with 5×10^{11} Xe^+ ions per cm^2, and the crystal, irradiated with 1×10^{12} Xe^+ ions per cm^2. The single crystal, irradiated with 1×10^{13} Xe^+ ions per cm^2, does not reveal traces of the hexagonal phase beyond a pressure

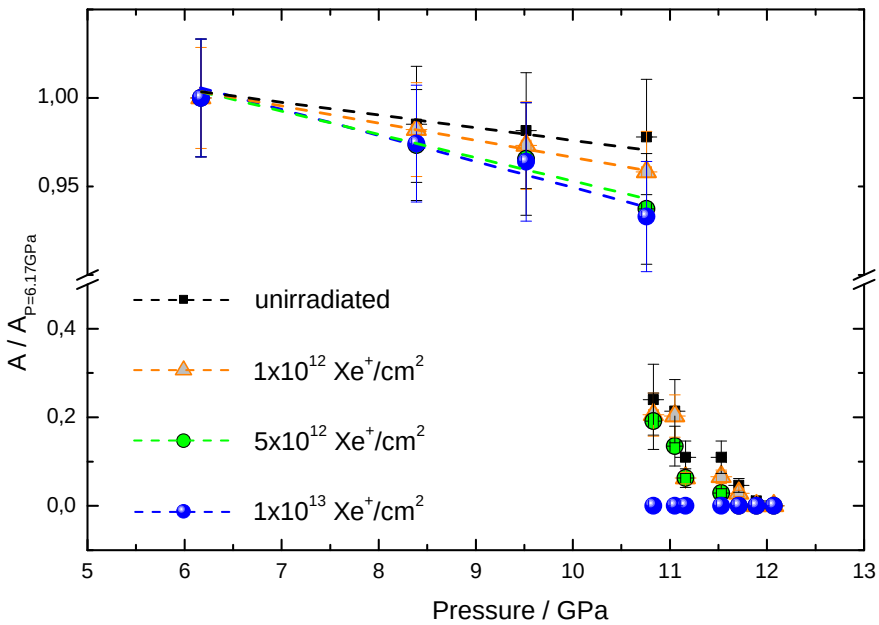

Figure 5.7: E_{2g} Raman band intensities of the four irradiated hBN crystals (Figure 4.16). Each intensity of Figure 4.17 is normalized to the Raman band area of the value, obtained at $P = 6.17$ GPa and displayed vs. pressure.

of (10.78 ± 0.05) GPa.

The sharp edge in the curvature of the Raman spectra can be explained by a powderization of the hBN crystal, when transforming into wBN. However, the remaining fraction of the hexagonal phase is not fluence indipendent. It is suggested, therefore, that irradiation-induced defects [79] can weaken the hexagonal lattice. Apparently, this does not result in a significantly depressed phase boundary by means of pressure. On the other hand, ion bombardment and the induced lattice damage can form smaller grains, as known from ion-beam milling [35, 110], which eventually reduces the Raman scattered intensity. However, this would not explain the analogies to the XRD-data. It is more likely, that interstitial atoms, kicked off their original sites by traversing ions, act on the process of phase transition catalytically, as proposed by Mosuang & Lowther [79].

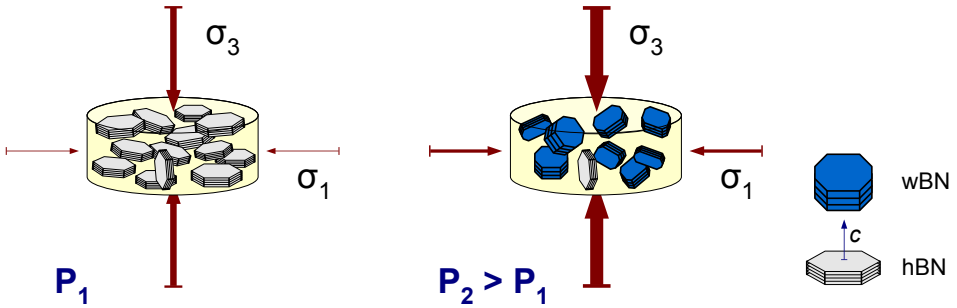

Figure 5.8: Inhomogeneity of the pressure distribution within the sample chamber in the gasket, causing the hBN *c*-vector to be aligned along the diamond axis (left). Those hBN crystals, oriented with the *c*-axis perpendicular to the diamond anvil axis (σ_3) can resist transformation to wBN due to minor effective pressure applied in *c* direction of the crystal (right).

5.5 Nature of the Defects

Geist and Römelt [34] identified and studied two types of paramagnetic centers in hexagonal BN (Figure 5.9). In one type, an unpaired electron was shown to interact with a single ^{11}B nucleus, giving rise to a four-line electron-paramagnetic (EPR) spectrum, and the defect was called a "one-boron center". A ten-line EPR spectrum occurs, if three ^{11}B nuclei share one unpaired electron, which is referred to as a "three-boron center" . Boron possesses two stable isotropes: ^{11}B and ^{10}B, with natural abundances of 81.17 % and 18.83 %, respectively [83]. With their different nuclear spins and magnetic moments, the two types of centers can be clearly identified using EPR. Khushidman *et al.* [58] suggested that the three-boron centers are actually F-centers. Furthermore, Moore and Singer [78] assumed on one hand the thermal production of the three-boron centers to be due to diffusion of carbon into hBN, and on the other hand by the effect of ionizing radiation. Here, the paramagnetic centers produced by irradiation appeared to be identical to those produced thermally. Their hypothesis was based on simplified π-electron quantum-chemical calculations which suggested that a nitrogen atom carries a negative charge in the hexagonal structure. Electrons can therefore be trapped in nitrogen vacancies – thus forming F-centers.

The energy difference between the defect state and the conduction band is evaluated as 1.0 eV for three-boron centers, and 0.7 eV for a one-boron cen-

ter [57]. However, pure white hBN was not affected by prolonged ionizing irradiation. Carbon impurities are thus considered as responsible for the stabilization of such F-centers. Jiménez *et al.* [53] proposed different types of nitrogen vacancies and showed that such vacancies are common defects in ion bombarded hBN, and part of the nitrogen atoms displaced from their crystalline sites moved to interstitial positions along with a fraction of the impinging ions that can remain embedded in the material. However, this group used low-energy N ions and therefore enriched the hBN matrix with nitrogen.

Displacement of a nitrogen atom from its site within the crystal requires 6.4 eV [1], necessary to surmount the strong σ-bonds. This cohesive energy is similar to that of cBN, but considerably higher than the cohesive energy between the adjacent hexagonal layers, which is reflected in the short distance to the neighbouring boron atom of 1.45 Å, and a wide interlayer spacing of 3.33 Å [99], produced by weak π-bonds. Therefore, the electron density in hBN is concentrated within instead of in between the layers [16]. Hence, a charged particle, traversing the system hBN, is being decelerated in a strongly anisotropic manner.

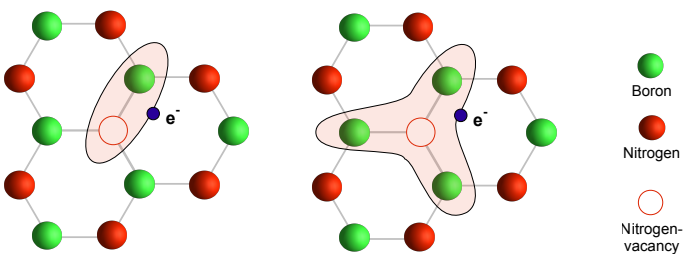

(a) one-boron center (b) three-boron center

Figure 5.9: Different types of boron centers in BN. Only the three-boron center is known to be a F-center [58].

6 Outlook

Though these experiments on boron nitride shed light on irradiation-induced processes as colourization, channeling, and a pressure related phase transition, the influences are not fully understood. Therefore, further investigations on irradiation damages and alterations in boron nitride are a matter of particular interest. Also, due to applications like the usage of cBN as anvil material in Paris-Edinburgh-presses, that are exposed to swift heavy ion irradiation and simultaneously applied high pressure, results of future research on this field may be beneficial.

As demonstrated, no traces of amorphization could be revealed in all three BN allotropes. Since such effects, however, were shown in graphite [86], but after treatment with higher fluences as applied in this work, it is interesting to learn, if irradiation doses of two orders of magnitude are capable for hBN amorphization. The newly installed XRD and SEM working sites at the GSI's novel facility M-branch offer possibility for *on-line* investigations even on single crystal specimens. However, in order to obtain a more detailed impression of radiation damage, several other methods have to be introduced.

SAXS

Small-angle X-ray scattering (SAXS) benefits from X-rays, scattered on density discontinuities and is therefore the ideal ion track detection method [60–62]. Recent SAXS measurements at the Australian Synchrotron facility revealed obvious differences in the patterns of the hBN crystals, displayed in Figure 4.6 (a)–(c). The samples, which were irradiated with 1×10^{12} and 5×10^{12} Au^{+} ions per cm^2 show evidence for the existence of ion track related damage formation indicated by the high anisotropy of the scattering.

First and preliminary analysis (Figure 6.1) revealed track radii of $\approx (21)$ Å, as suggested by Kluth & Rodriguez. Interestingly, no difference were measured between samples of diffent orientations during ion bombardment (perpendicular and parallel to the hBN c-axis).

Differences, however, occured in the scattering spectra for different fluences, and it could be said that at the highest fluence (5×10^{12} Au^{+}/cm^{2}) two populations of particles are present with an important scattering contribution.

In any case, further SAXS measurements of BN as function of ion fluence (lower fluences in order to avoid track overlap) on thinned samples, and/or additional TEM measurements can yield further information.

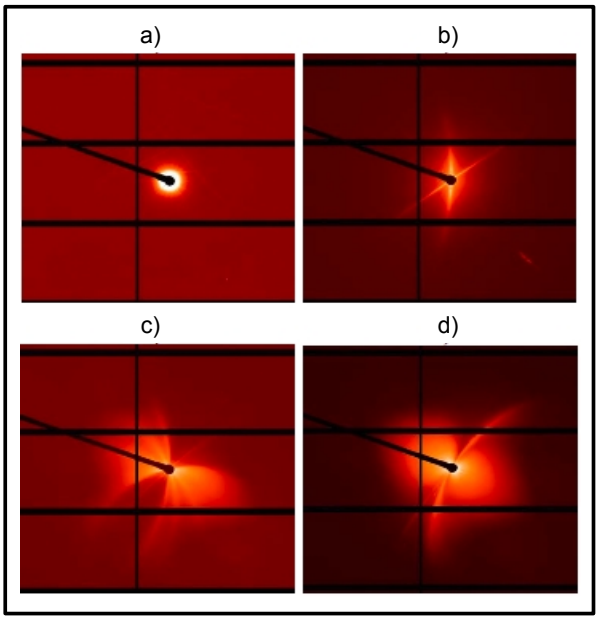

Figure 6.1: SAXS images of hBN single crystals: a) unirradiated sample, b) sample irradiated to a fluence of 5×10^{12} Au^{+}/cm^{2}, c) and d) sample irradiated to a fluence of 1×10^{12} Au^{+}/cm^{2}. The halo in a) around the center comes from the unscattered X-ray beam. Figures b), c) and d) show streaks, intersecting the center, which is a clear proof of density discontinuities, most probably derived from ion tracks. All randomly distributed lines around the center are negligible Kossel-lines.

TEM

Transmission electron microscopy is a capable method for the investigation in atomic dimensions, and therefore useful for promising investigations on ion tracks in boron nitride. Though we could not verify any phase transition in BN, which was irradiated without subsequent or simultaneous pressurization, it might be possible to amorphize hBN in the wake of the traversed ion, as the detected density inhomogeneities suggest.

In graphite, which resembles hBN, irradiation with high fluences of Ar^+ ions triggered the growth of nanocrystalline diamond [133]. Therefore, further TEM investigations on irradiated hBN may eventually reveal the production of the cubic phase, which is the diamond counterpart of boron nitride.

TEM also confirmed quenching of a $Gd_2Zr_2O_7$ high pressure phase after simultaneous pressurization and ion irradiation [66], which additionally encourages continuative research.

Channeling

The surprisingly arisen effect of the clearly orientation dependent irradiation behaviour in hBN certainly deserves further regards, because hereby one can access molecular information of the partly ionic and partly covalent character of the sp^2-bonds of hBN. Due to suggested channeling effect, ions, traversing the crystals, are supposed to be decelerated in a different manner, depending whether impinging parallel or perpendicular to the c-axis of hBN. On this note it would be interesting to repeat the stopping experiment for heavy ions in diamond [65], with hBN crystals, exposed to the ion beam with different orientations. However, due to the small size of the crystals, such an experiment will turn out ambitious.

Bibliography

[1] K. Albe.
Theoretical study of boron nitride modifications at hydrostatic pressures.
Physical Review B, 55:6203–6210, 1997.

[2] B. Baer, M. Chang, and W. Evans.
Raman shift of stressed diamond anvils: Pressure calibration and culet geometry dependence.
J. of Applied Physics, 104:034504, 2008.

[3] Y. Bai-Ru et al.
Structural and Thermodynamic Properties of Wurtzitic Boron Nitride from First-Principle Calculations.
Commun. Theor. Phys., 48:925–929, 2007.

[4] W. Balmain.
Bemerkungen über die Bildung von Verbindungen des Bors und Siliciums mit Stickstoff und gewissen Metallen.
J. Prakt. Chem., 27:422–430, 1842.

[5] A. Bassett.
Diamond anvil cell, 50th birthday.
High Pressure Research, 29(2):163–186, 2009.

[6] A. Benyagoub.
Mechanism of the monoclinic-to-tetragonal phase transition induced in zirconia and hafnia by swift heavy ions.
Physical Review B, 72:094114, 2005.

[7] A. Benyagoub.
Phase transformations in oxides induced by swift heavy ions.
Nuclear Instruments and Methods in Physics Research B, 245:225–230, 2006.

[8] A. Benyagoub, F. Couvreur, S. Bouffard, et al.
Phase transformation induced in pure zirconia by high energy heavy ion irradiation.
Nucl. Instr. and Meth. B, 175:417, 2001.

[9] A. Benyagoub, F. Levesque, F. Couvreur, C. Gibert-Mougel, C. Dufour, and E. Paumier.
Evidence of a phase transition induced in zirconia by high energy heavy ions.
Applied Physics Letters, 77:20, 2000.

[10] H. Bethe.
Zur Theorie des Durchgangs schneller Korpuskularstrahlen durch Materie.
Annalen der Physik, 397:325–400, 1930.

[11] S. Bhagavantam and D. N. Rao.
Dielectric Constant of Diamond.
Nature, 161:729, 1948.

[12] F. Bloch.
Zur Bremsung rasch bewegter Teilchen beim Durchgang durch Materie.
Annalen der Physik, 408:285–320, 1933.

[13] W. Bragg.
The Diffraction of Short Electromagnetic Waves by a Crystal.
In *Proceedings of the Cambridge Philosophical Society*, volume 17, pages 43–57, 1913.

[14] S. Brorson, A. Kazeroonian, J. Moodera, D. Face, T. Cheng, E. Ippen, M. Dresselhaus, and G. Dresselhaus.
Femtosecond Room Temperature Measurement of the Electron-Phonon Coupling Constant λ in Metallic Superconductors.
Physical Review Letters, 64:2172, 1990.

[15] F. Bundy and R. Wentorf.
Direct transformation of hexagonal boron nitride to denser forms.
J. Chem Phys, 38:1144–1149, 1963.

[16] A. Catellani, M. Posternak, A. Baldereschi, and A. Freeman.
Bulk and surface electronic structure of hexagonal boron nitride.
Physical Review B, 36:6105–6111, 1987.

[17] J. Che et al.
Thermal conductivity of diamond and related materials from molecular dynamics simulations.
J. Chem. Phys., 113:6888–6900, 2000.

[18] N. G. Chopra et al.
Boron Nitride Nanotubes.
Science, 269:966–967, 1995.

[19] F. Corrigan and F. Bundy.
Direct transitions among the allotropic forms of boron nitride at high pressures and temperatures.
J. Chem. Phys., 63:3812, 1975.

[20] J. Cowley.
Diffraction Physics, page 126.
North-Holland Publishing Company, second, revised edition, 1981.

[21] H. Dammak, A. Barbu, A. Dunlop, D. Lesueur, and N. Lorenzelli.
$\alpha \rightarrow \omega$ phase transformation induced in titanium during ion irradiations in the electronic slowing-down regime.
Philosophical Magazine Letters, 67:253–259, 1993.

[22] F. Dessauer.
Über einige Wirkungen von Strahlen I.
Zeitschrift für Physik, 12:38–47, 1923.

[23] G. Doll.
Properties of Group III Nitrides.
Inspec, London, 1994.

[24] N. Dubrovinskaia, L. Dubrovinsky, W. Crichton, F. Langenhorst, and A. Richter.
Aggregated diamond nanorods, the densest and least compressible form of carbon.
Applied Physics Letters, 87:083106, 2005.

[25] N. Dubrovinskaia, V. Solozhenko, N. Miyajima, V. Dmitriev, O. Kurakevych, and L. Dubrovinsky.
Superhard nanocomposite of dense polymorphs of boron nitride: Noncarbon material has reached diamond hardness.

Applied Physics Letters, 90:101912, 2007.

[26] C. Dufour et al.
A high-resistivity phase induced by swift heavy-ion irradiation of Bi: a probe for thermal spike damage?
Zeitschrift für Physik, 12:38–47, 1923.

[27] M. Eremets.
Megabar high-pressure cells for Raman measurements.
J. of Raman Spectroscopy, 34:515–518, 2003.

[28] M. Eremets et al.
Disordered state in first-order phase transitions: Hexagonal-to-cubic and cubic-to-hexagonal transitions in boron nitride.
Physical Review B, 57:5655–5660, 1998.

[29] M. Ferhat, A. Zaoui, M. Certier, and H. Aourag.
Electronic structure of BN, BP and BAs - The Art of Scientifique Computing.
Physica B, 252:229–236, 1998.

[30] R. Fleischer, P. Price, and R. Walker.
Ion Explosion Spike Mechanism for Formation of Charged-Particle Tracks in Solids.
Journal of applied Physics, 36:3645–3652, 1965.

[31] J. Furthmüller, J. Hafner, and G. Kresse.
Physical Review B, 50:606, 1994.

[32] K. Gavrichev, V. Solozhenko, V. Gorbunov, L. Golushina, G. Totrova, and V. Lazarev.
Low-temperature heat capacity and thermodynamic properties of four boron nitride modifications.

[33] R. Geick, C. Perry, and G. Rupprecht.
Normal Modes in Hexagonal Boron Nitride.

[34] D. Geist and G. Römelt.
Paramagnetische Elektronenresonanz in Bornitrid.

[35] L. Giannuzzi and F. Stevie.
A review of focused ion beam milling techniques for TEM specimen preparation.

Micron, 30:197–204, 1999.

[36] P. Gielisse et al.
Lattice Infrared Spectra of Boron Nitride and Boron Monophosphide.

[37] D. Golberg, Y. Bando, O. Stéphan, and K. Kurashima.
Octahedral boron nitride fullerenes formed by electron beam irradiation.
Applied Physics Letters, 73:2441–2443, 1998.

[38] H. Hauptmann and J. Karle.
Solution of the Phase Problem.
American Crystallographic Society, 1953.

[39] R. Hemley.
Effects of High Pressure on Molecules.
Annu. Rev. Phys. Chem., 51:763–800, 2000.

[40] R. Hemley and N. Ashcroft.
The Revealing Role of Pressure in the Condensed Matter Sciences.
Physics Today, 51(8):26–32, 1998.

[41] C. Henager et al.
Thermal Conductivities of thin, sputtered optical films.
Applied Optics, 32:91–101, 1993.

[42] J. Heremans, C. Olk, and D. Morelli.
Magnetic susceptibility of carbon structures.
Physical Review B, 49:15122–15125, 1994.

[43] W. Holzapfel.
Refinement of the ruby luminescence pressure scale.
J. of Applied Physics, 93(3):1813–1818, 2003.

[44] HORIBA Jobin Yvon.
HR 800 User Manual.

[45] HORIBA Jobin Yvon.
LabSpec5 User's Manual.

[46] S. Horiuchi, J. Huang, L. He, J. Mao, and T. Taniguchi.
Facilitated synthesis of cubic boron nitride by a mechanochemical effect.
Philosophical Magazine A, 78:1065–1072, 1998.

[47] http://www inj.gsi.de/index.php?section=3&subsection=1.

[48] http://www.gsi.de/beschleuniger/sis18/sis.html.

[49] J. Huang, H. Yasuda, H. Mori, and T. Mitchell.
HRTEM and EELS Studies on the Amorphization of Hexagonal Boron Nitride Induced by Ball Milling.
Journal of the American Ceramic Society, 83:403–409, 2004.

[50] J. Huang and Y. Zhu.
Defect and Diffusion Forum, 186:1–32, 2000.

[51] ICRUM.
Stopping Powers and Ranges for Protons and Alpha Particles.
Technical report, Report 49 of the International Commission on Radiation Units and Measurements, Bethesda, MD, USA, 1993.

[52] T. Ishii and T. Sato.
J. of Crystal Growth, 61:689, 1983.

[53] I. Jiménez, A. Jankowski, L. Terminello, D. Sutherland, J. Carlisle, G. Doll, W. Tong, D. Shuh, and F. Himpsel.
Core-level photoabsorption study of defects and metastable bonding configurations in boron nitride.
Physical Review B, 55:12025, 1997.

[54] J. J.R. Riter.
Discussion of shock-induced graphite → wurtzite phase transformation in BN and implications for stacking in graphitic BN.
J. Chem. Phys., 59:1538, 1973.

[55] E. Jäger and J. C. Hunziker.
Lectures in Isotope Geology.
Springer, Germany, 1979.

[56] K. Karch and F. Bechstedt.
Ab initio lattice dynamics of BN and AlN: Covalent versus ionic forces.
Physical Review B, 56:7404, 1997.

[57] A. Katzir, J. Suss, A. Zunger, and A. Halperin.
Point defects in hexagonal boron nitride. I. EPR, thermoluminescence, and thermally-stimulated-current measurements.
Physical Review B, 11:2370, 1975.

[58] M. Khusidman and V. Neshpor.
An Investigation of hexagonal Boron Nitride by means of Electron Para-

magnetic Resonance.
Theoretical and Experimental Chemistry, 3:152–153, 1967.

[59] S. Klotz, J.-C. Chervin, P. Munsch, and G. L. Marchand.
Hydrostatic limits of 11 pressure transmitting media.
Journal of Physics D: Applied Physics, 42:075413, 2009.

[60] P. Kluth, B. Johannessen, G. Foran, D. Cookson, S. Kluth, and M. Ridgway.
Disorder and cluster formation during ion irradiation of Au nanoparticles in SiO_2.
Physical Review B, 74:014202, 2006.

[61] P. Kluth, C. Schnohr, O. Pakarinen, F. Djurabekova, D. Sprouster, R. Giulian, M. Ridgway, A. Byrne, C. Trautmann, D. Cookson, K. Nordlund, and M. Toulemonde.
Fine Structure in Swift Heavy Ion Tracks in Amorphous SiO_2.
Physical Review Letters, 101:175503, 2008.

[62] P. Kluth, C. Schnohr, D. Sprouster, A. Byrne, D. Cookson, and M. Ridgway.
Measurement of latent tracks in amorphous SiO_2 using small angle X-ray scattering.
Nuclear Instruments and Methods in Physics Research B, 266:2994–2997, 2008.

[63] E. Knittle and R. Jeanloz.
High-Pressure metallization of FeO and implications for the earth's core.
Geophysical Research Letters, 13(13):1541–1544, 1986.

[64] A. Kurdyumov, V. Solozhenko, and W. Zelyavski.
Lattice parameters of boron nitride polymorphous modifications as a function of their crystal-structure perfection.
J. Appl. Cryst., 28:540–545, 1995.

[65] M. Lang, U. Glasmacher, R. Neumann, D. Schardt, C. Trautmann, and G. Wagner.
Energy loss of 50-GeV uranium ions in natural diamond.
Appl. Phys. A, 80:691–694, 2005.

[66] M. Lang, F. Zhang, J. Zhang, J. Wang, B. Schuster, C. Trautmann,

R. Neumann, U. Becker, and R. Ewing.
Nanoscale manipulation of the properties of solids at high pressure with relativistic heavy ions.
Nature Materials, 8:793–797, 2009.

[67] G. Lian, X. Zhang, L. Zhu, D. Cui, Q. Wang, and X. Tao.
Phase transformation of boron nitride under hypothermal conditions.
Journal of Solid State Chemistry, 182:1326–1330, 2009.

[68] J. Lian, X. Zu, K. Kutty, J. Chen, L. Wang, and R. Ewing.
Ion-irradiation-induced amorphization of $La_2Zr_2O_7$ pyrochlore.
Physical Review B, 66:054108, 2002.

[69] L. Liu, Y. Feng, and Z. Shen.
Structural and electronic properties of hbn.
Physical Review B, 68:104102, 2003.

[70] C. Louis, K. Iyakutti, and P. Malarvizhi.
Pressure dependence of metallization and superconducting transition of AgCl and AgBr.
J. Phys.: Condens. Matter, 16(9):1577–1592, 2004.

[71] C. Manfredotti, E. Vittone, A. L. Giudice, C. Paolini, F. Fizzotti, C. Dinca, V. Ralchenko, and S. Nistor.
Ionosuminescence in CVD diamond and in cubic boron nitride.
Diamond and Related Materials, 10:568–573, 2001.

[72] H. Mao, P. Bell, J. Shaner, and D. Steinberg.
Specific volume meassurements of Cu, Mo, Pd and Ag and calibration of the ruby R_1 fluorescence pressure gauge from 0.006 to 1 Mbar.
J. of Applied Physics, 49:3276–3283, 1978.

[73] H. Mao, J. Xu, and P. Bell.
Calibration of the Ruby Pressure Gauge to 800 kbar Under Quasi-Hydrostatic conditions.
J. of Geophysical Research, 91:4673–4676, 1986.

[74] A. Meldrum, S. Zinkle, L. Boatner, and R. Ewing.
Heavy-ion irradiation effects in the ABO_4 orthosilicates: Decomposition, amorphization, and recrystallization.
Physical Review B, 59:3981–3992, 1999.

[75] Y. Meng et al.
The formation of sp^3 bonding in compressed BN.
Nature Materials, 3:111–114, 2004.

[76] H. Mieskes, W. Assmann, F. Grüner, H. Kucal, Z. Wang, and M. Toulemonde.
Electronic and nuclear thermal spike effects in sputtering of metals with energetic heavy ions.
Physical Review B, 67:155414, 2003.

[77] R. Miletich, editor.
Mineral Behaviour at Extreme Conditions, volume 7 of *European Mineralogical Union - Notes in Mineralogy*, chapter 4, pages 95–116.
Eötvös Unitversity Press, Budapest, Hungary, 2005.

[78] A. Moore and L. Singer.
Electron Spin Resonance in Carbon-Doped Boron Nitride.
J. Phys. Chem. Solids, 33:343–355, 1972.

[79] T. Mosuang and J. Lowther.
Influence of defects on the *h*-BN to *c*-BN transformation.
Physical Review B, 66:014112, 2002.

[80] Y. Muramatsu, T. Kaneyoshi, E. Gullikson, and R. Perera.
Angle-resolved soft X-ray emission and absorption spectroscopy of hexagonal boron nitride.
Spectrochimica Acta A, 59:1951–1957, 2003.

[81] H. Naguib and R. Kelly.
Criteria for bombardment-induced structural changes in non-metallic solids.
Radiation Effects and Defects in Solids, 25:1–12, 1975.

[82] R. Nemanich, S. Solin, and R. Martin.
Light scattering study of boron nitride microcrystals.
Physical Review B, 23:6348, 1981.

[83] NIST.
National Institute of Standards and Technology: Atomic Weights and Isotopic Compositions for all Elements, 9 2008.

[84] NISTIR 4999.

Stopping Power and Range Tables,
www.physics.nist.gov/PhysRefData/Star/Text/programs.html.

[85] S. Nistor, D. Ghica, M. Stefan, L. Nistor, E. Goovaerts, and T. Taniguchi.
Irradiation defects in superhard cubic boron nitride single crystals.
Nuclear Instruments and Methods in Physics Research B, 266:2784–2787, 2008.

[86] K. Niwase.
Irradiation-induced amorphization of graphite.
Physical Review B, 52:15785, 1995.

[87] N. Ohba, K. Miwa, N. Nagasako, and A. Fukumoto.
First-principles study on structural, dielectric, and dynamical properties for three BN polytypes.
Physical Review B, 63:115207, 2001.

[88] N. Ooi, A. Rairkar, L. Lindsley, and J. Adams.
Electronic structure and bonding in hexagonal boron nitride.
Journal of Physics: Condensed Matter, 18:97–115, 2006.

[89] W. Orellana and H. Chacham.
Stability of native defects in hexagonal and cubic boron nitride.
Physical Review B, 63:125205, 2001.

[90] A. Patterson.
A Fourier Series Method for the Determination of the Components of Interatomic Distances in Crystals.
Physical Review, 46:372–376, 1934.

[91] A. Patterson.
A direct method for the determination of the components of interatomic distances in crystals.
Zeitschrift für Kristallographie, 90:517–542, 1935.

[92] G. Piercy, F. Brown, J. Davies, and M. McCargo.
Experimental Evidence for the Increase of Heavy Ion Ranges by Channeling in Crystalline Structure.
Physical Review Letters, 10:399–400, 1963.

[93] H. Pierson.
Handbook of carbon, graphite, diamond, and fullerenes: Properties, Pro-

cessing and Applications.
Noyes Publications, 1993.

[94] A. Pilyankevich, A. Kurdyumov, and N. Ostrovskaya.
On the crystallographic irreversibility of some phase transformations in boron nitride.
Phys. Stat. Sol. A, 116:k1–k5, 1989.

[95] M. Polanyi.
Über die Natur des Zerreißvorganges.
Zeitschrift für Physik A, 7:323–327, 1921.

[96] V. Polyakov and N. Kharlashina.
The use of heat capacity data to calculate carbon isotope fractionation between graphite, diamond, and carbon dioxide: A new approach.
Geochimica et Cosmochimica Acta, 59:2561–2572, 1995.

[97] C. Raman and K. Krishnan.
A new type of secondary radiation.
Nature, 121:501, 1928.

[98] S. Reich et al.
Resonant Raman scattering in cubic and hexagonal boron nitride.
Physical Review B, 71:205201, 2005.

[99] J. Robertson.
Electronic structure and core exciton of hexagonal boron nitride.
Physical Review B, 29:2131, 1984.

[100] M. Robinson.
Computer Studies of the Slowing Down of Energetic Atoms in Crystals.
Physical Review, 132:2385–2398, 1963.

[101] M. Robinson and O. Oen.
The Channeling of Energetic Atoms in Crystal Lattices.
Applied Physics Letters, 2:30–32, 1963.

[102] S. Rumyantsev et al.
Properties of Advanced Semiconductor Materials GaN, AlN, InN, BN, SiC, and SiGe.
John Wiley & Sons, Inc., New York, 2001.

[103] H. Rydberg et al.

Van der Waals Density Functional for Layered Structures.
Physical Review Letters, 91:1264021, 2003.

[104] H. Sachdev.
Influence of impurities on the morphology and Raman spectra of cubic boron nitride.
Diamond and Related Materials, 12:1275–1286, 2003.

[105] T. Schmidt, R. Baierle, P. Piquini, and A. Fazzio.
Theoretical study of native defects in bn nanotubes.
Physical Review B, 67:113407, 2003.

[106] B. Schuster, M. Lang, R. Klein, C. Trautmann, R. Neumann, and A. Benyagoub.
Structural phase transition in ZrO_2 induced by swift heavy ion irradiation at high-pressure.
Nucl. Instr. and Meth. B, 267:964–968, 2009.

[107] E. Shishonok and J. Steeds.
Near-threshold creation of optical centres in electron irradiated cubic boron nitride.
Diamond and Related Materials, 11:1774–1780, 2002.

[108] Y. Shu-Jie, C. Lian-Chen, and J. Chang-Qing.
Hydrostaticity of Pressure Media in Diamond Anvil Cells.
Chinese Physics Letters, 26:096202, 2009.

[109] P. Sigmund.
Stopping of Heavy Ions.
Springer, Germany, 2004.

[110] W. Sinclair and H. Simmons.
Microstructure and thermal shock behaviour of BN composites.
Journal of Materials Science Letters, 6:627, 1987.

[111] A. Smekal.
Zur Quantentheorie der Dispersion.
Naturwissenschaften, 11:873, 1923.

[112] E. Smith and G. Dent.
Modern Raman Spectroscopy - A Practical Approach.
John Wiley & Sons Ltd., The Atrium, Southern Gate, Chichester, West

Sussex PO19 8SQ, England, 2005.

[113] V. Solozhenko.
Thermodynamics of dense boron nitride modifications and a new phase P,T diagram for BN.
Thermochimica Acta, 218:221–227, 1993.

[114] V. Solozhenko.
Diamond and Related Materials, 4:1, 1994.

[115] V. Solozhenko, D. Häusermann, M. Mezouar, and M. Kunz.
Equation of state of wurtzitic boron nitride to 66 GPa.
Applied Physics Letters, 72:1691–1693, 1998.

[116] V. Solozhenko and T. Peun.
Compression and Thermal Expansion of Hexagonal Graphite-Like Boron Nitride up to 7 GPa and 1800 K.
J. Phys. Chem. Solids, 58:1321–1323, 1997.

[117] V. Solozhenko, G. Will, and F. Elf.
Isothermal compression of hexagonal graphite-like boron nitride up to 12 GPa.
Solid State Commun., 96:1–3, 1995.

[118] J. Stark.
Zerstreuung und Absorption von β-Strahlen und Röntgenstrahlen.
Physikalische Zeitschrift, 13:973, 1912.

[119] O. Stéphan, Y. Bando, A. Loiseau, F. Willaime, N. Shramchenko, T. Tamiya, and T. Sato.
Formation of small single-layer and nested BN cages under electron irradiation of nanotubes and bulk material.
Applied Physics A, 67:107–111, 1998.

[120] K. Takemura.
Evaluation of the hydrostaticity of a helium-pressure medium with powder x-ray diffraction techniques.
J. of Applied Physics, 89:662, 2001.

[121] T. Taniguchi and K. Watanabe.
Synthesis of high-purity boron nitride single crystals under high pressure by using ba-bn solvent.

Journal of Crystal Growth, 303:525–529, 2007.

[122] T. Taniguchi, K. Watanabe, and S. Koizumi.
Defect characterization of cBN single crystals grown under HP/HT.
Phys. Stat. Sol. A, 201:2573–2577, 2004.

[123] T. Taniguchi and S. Yamaoka.
Spontaneous nucleation of cubic boron nitride single crystal by temperature gradient method under high pressure.
Journal of Crystal Growth, 222:549–557, 2001.

[124] C. Taylor, editor.
Proceedings of the NATO Advanced Research Workshop on Diamond Based Composites and Related Materials, volume 72.

[125] M. Ueno et al.
Room-temperature transition of rhombohedral-type boron nitride under high static pressure.
Physical Review B, 45:10226–10232, 1992.

[126] B. Vainstein, V. Fridkin, and V. Indenborn.
Structure of Crystals, Modern Crystallography, volume 2.

[127] P. van Camp and V. van Doren.
Total energy calculations in the dft on binary compounds.
Int. J. Quantum Chemistry, 55:339–345, 1995.

[128] M. Wakatsuki, K. Takano, and G. Fujita.
Topotoxial and some other characters of the transformation from hexagonal to wurtzitic BN.
Physica B, 139:256–258, 1986.

[129] M. Waligorski, R. Hamm, and R. Katz.
The Radial Distribution of Dose around the Path of a Heavy Ion in Liquid Water.
Nuclear Tracks and Radiation Measurement, 11:309–319, 1986.

[130] H. Wang, Q. Li, T. Cui, Y. Ma, and G. Zou.
Phase-transition mechanism of hBN → wBN from first principles.
Solid State Communications, 149:843–846, 2009.

[131] S. Wang, L. Wang, R. Ewing, G. Was, and G. Lumpkin.
Ion irradiation-induced phase transformation of pyrochlore and zircono-

lite.

Nuclear Instruments and Methods in Physics Research B, 148:704–709, 1999.

[132] Z. Wang, C. Dufour, E. Paumier, and M. Toulemonde.
The S_e sensitivity of metals under swift-heavy-ion irradiation: a transient thermal process.
Journal of Physics: Condensed Matter, 6:6733–6750, 1994.

[133] Z. Wang, G. Yu, L. Yu, F. Zhu, D. Zhu, H. Xu, and M. Ruan.
Nanocrystalline diamond formation during argon ion irradiation of graphite.
Journal of Applied Physics, 91:3480–3482, 2002.

[134] S. Weissmantel, B. Reisse, B. Keiper, and S. Schulze.
Microstructure and mechanical properties of pulsed laser deposited boron nitride films.
Diamond and Related Materials, 8:377, 1999.

[135] R. Wentorf.
Cubic Form of Boron Nitride.
J. Chem Phys, 26:956, 1957.

[136] E. Wigner and H. Huntington.
On the Possibility of a Metallic Modification of Hydrogen.
Journal of Chemical Physics, 3(12):764, 1935.

[137] R. Winter and J. Jonas.
High Pressure Molecular Science, page 291.
Dordrecht, Netherlands: Kluwer, 1999.

[138] J. Xu, H. Mao, and P. Bell.
High-Pressure Ruby and Diamond Fluorescence: Observations at 0.21 to 0.55 Terapascal.
Science, 232(4756), June 1986.

[139] Y.-N. Xu and W. Ching.
Calculation of ground-state and optical properties of hBN, cBN and wBN.
Physical Review B, 44:7787–7798, 1991.

[140] S. Yixi et al.
Vacuum-ultraviolet reflectance spectra and optical properties of nanoscale

wurtzite boron nitride.
Physical Review B, 50:576–578, 1994.

[141] K. Yuge.
Pressure effects on the phase stability of cubic BNC ternary alloys.
Journal of Physics: Condensed Matter, 21:055403, 2009.

[142] R. Zedlitz, M. Heintze, and M. Schubert.
Properties of amorphous boron nitride thin films.
Journal of Non-Crystalline Solids, 198:403–406, 1996.

[143] C. Zha, H. Mao, and R. Hemley.
Elasticity of MgO and a primary pressure scale to 55 GPa.
97(25):13494–13499, December 5 2000.

[144] J. Ziegler.
SRIM-2003.
Nucl. Instr. Meth. B, 219:1027–1036, 2004.

[145] A. Zunger and A. Freeman.
Ab initio self-consistent study of the electronic structure and properties of cubic boron nitride.
Physical Review B, 17(4):2030–2042, 1978.

[146] J. Zupan, M. Komac, and D. Kolar.
Magnetic Susceptibility of Boron Nitride.
Journal of Applied Physics, 41:5337, 1970.